Doctoral Dissertation
Doctoral Program in Energy Engineering (31th Cycle)

Development of the Multi-physiCs tool for the integrated simulation of the Cavity and its application for the design of gyrotron cavities for thermonuclear applications

By

Andrea Bertinetti

******

Supervisor:
Prof. L. Savoldi, Politecnico di Torino

Doctoral Examination Committee:

Prof. E. Chiavazzo, Politecnico di Torino
Dr. W. Bin, Istituto per la Scienza e Tecnologia dei Plasmi
Dr. A. Moro, Istituto per la Scienza e Tecnologia dei Plasmi
Dr. F. Albajar, Fusion for Energy
Dr. A. Leggieri, Thales

Politecnico di Torino
2019

Declaration

I hereby declare that, the contents and organization of this dissertation constitute my own original work and does not compromise in any way the rights of third parties, including those relating to the security of personal data.

Andrea Bertinetti

2019

This work has been partly carried out within the framework of the EUROfusion Consortium and has received funding from the Euratom research and training programme 2014-2018 under grant agreement No 633053. The views and opinions expressed herein do not necessarily reflect those of the European Commission.

* This dissertation is presented in partial fulfilment of the requirements for **Ph.D. degree** in the Graduate School of Politecnico di Torino (ScuDo).

Acknowledgement

First of all, I wish to thank my mother, my father and my brother for supporting me all along my educational path. I would also thank my grandparents, my cousins, my uncles and aunts.

I would also like to thank my supervisor, prof. L. Savoldi, who guided me through my PhD experience, prof. A. Carpignano, prof. S. Dulla, prof. N. Pedroni, prof. P. Ravetto, prof. F. Subba, and prof. R. Zanino.

Many thanks to the people met during this part of my career, Kostas, Sebastian, Parth, Alberto, Francesca, Fabio, Ferran, Francois, Stefano, and Jean-Philippe.

I also wish to thank all the PhD students that have shared this experience with me: Nicolò A., Andrea Bers., Roberto, Alberto, Mattia, Stefano, Dominic, Nicolò F., Antonio, Giuseppe Francesco, Raffaella, Anna Chiara and Andrea Z.: your presence made these years a lot less hard.

Abstract

High-power gyrotrons, used in tokamaks and stellarators for electron cyclotron resonance heating and current drive, deliver microwave power of the order of MW per unit, at frequencies above 100 GHz, to sustain the plasma conditions during the fusion reactors operations for the production of electrical power. The ohmic load, produced by the interaction between electrons beam that moves inside the central hollow region of the resonator and the magnetic field, is deposited on the inner wall of the resonant cavity and it constitutes one of the major technological factors which limits the gyrotron operations conditions. A forced flow of pressurized water is used to cool down the cavity structures to reduce the temperature and, consequently, to minimize the deformation of the resonating surfaces.

In the frame of the EUROfusion activities the MUlti-physiCs tool for the integrated simulation of the CAvity (MUCCA) has been developed in the collaboration between Politecnico di Torino (PoliTo), Karlsruhe Institute of Technology (KIT), Fusion for Energy (F4E) and Thales Electron Devices (TED), since 2016. The MUCCA tool includes thermal-hydraulic, thermo-mechanical and electro-dynamic simulations in an iterative self-consistent procedure applied to compute the gyrotron cavity behaviour, aiming at evaluating the modification of the operating conditions of the component. The MUCCA tool is applied in this work to different cavity layouts in order to present the characteristics of the simulation tool and to show the wide range of its application for the development the cooling aspects of the gyrotron cavities.

The tool is successfully validated comparing the computed results with those from the experimental test campaigns performed on the cavity designed for the 170 GHz, 1 MW gyrotron developed for ITER electron cyclotron system. In this cavity layout, the Raschig Rings (RRs) cooling structure is used as a heat transfer promoter to reduce the temperature inside the resonator. On the same cavity structure, an alternative cooling configuration, involving a set of parallel semi-circular Mini-Channels (MCs), is proposed and optimized to improve the thermal behaviour of the cavity aiming at reducing the temperature peak computed in the most critical region of the resonating region of the cavity.

In DEMO perspective, the MUCCA tool is used to evaluate the evolution of the coaxial cavity design, currently under development with an annular cooling strategy for the 170 GHz, 2 MW gyrotrons. In order to improve the performances of the gyrotrons to be used in the DEMO electron cyclotron system, the layout of the cavity is designed at KIT including the coaxial insert, which is also modelled in the simulations. The computed results highlight the necessity to optimize the preliminary annular cooling configuration proposed, since the temperature peak obtained with the present annular cooling configuration overcomes in ~150 ms the limits defined for the safe gyrotron operation conditions. As performed in the analysis of the cavity for the 1 MW gyrotrons, an explorative simulation is performed applying a set of parallel circular MCs as cooling promoter strategy, which improve considerably the cooling behaviour of the cavity with respect to the annular cooling design.

Contents

List of Figures

List of Tables

Nomenclature

Abbreviations

3D	Three Dimensional
B-U	Bottom-Up
CAD	Computer Aided Drafting
CFD	Computational Fluid Dynamics
DEM	Discrete Element Method
DEMO	DEMOnstration
EC	Electron Cyclotron
ECCD	Electron Cyclotron Current Drive
ECRH	Electron Cyclotron Resonance Heating
ED	Electro-Dynamic
RF	Radio Frequency
HTC	Heat Transfer Coefficient
IAPWS	International Association for the Properties of Water and Steam
ICHR	Ion Cyclotron Resonance Heating
ITER	International Thermonuclear Experimental Reactor
JET	Joint European Torus
KIT	Karlsruher Institut für Technologie
K-STAR	Korea Superconducting Tokamak Advanced Research
MIG	Magnetron Injection Gun
MCs	Mini-Channels
MUCCA	Multi-physiCs tool for the integrated simulation of the CAvity
PoliTo	Politecnico di Torino
RRs	Raschig Rings
SA	Super Advanced
T-D	Top-Down
TC	ThermoCouple
TH	Thermal-Hydraulic
TM	Thermo-Mechanical

Symbols

A	Area
b	Cross section
B_o	Magnetic field
c	Light speed in vacuum

c_p	Specific heat
C_{qw}	Solid-liquid interface coefficient
D	Diamater
D_h	Hydraulic diameter
E	Energy, Young modulus
f	Friction factor coefficient, frequency
g	Gravity acceleration
G	Specific mass flow rate
k_B	Boltzmann constant
L, l	Length
m	Mass, mass flow
n	Plasma density
n_p	Prandtl number exponent
T	Temperature
p	Pressure
P	Power
Pr	Prandtl number
Q	Gain parameter
R	Radius
Re	Reynolds number
R_c	Thermal contact resistance
q	Heat
sat	Saturation
v	Velocity
z	Axial coordinate

Greek

α	Thermal expansion coefficient
γ	Relativistic factor
δ	Skin depth
ε	Relative error
λ	Wavelength
μ	Dynamic viscosity, permittivity
ρ	Density, heat load
σ	Surface tension, electrical conductivity
τ_E	Confinement time
ω_c	Cyclotron frequency

Subscripts

α	Alpha particles
B	Bremsstrahlung

bulk	Bulk
bw	Boiling at wall
Cu	Copper
e	Electron
el	Electrical
in	Inlet
ins	Insert
l	Liquid
lat	Latent of vaporization
loss	Losses
max	Maximum
k	Thermal conduction
out	Outlet
res	Resonator
s	Surface
tan	Tangential
th	Thermic
tot	Total
v	Vapour
wall	Wall
0	Initial

Chapter 1

Introduction

The increase of World population and of the life standards in developing countries is strictly related with the growing energy demand, expected to double in the next 30 years [1]. The need for more energy has a strong effect on the environment. For instance, the use of fossil fuels, satisfying approximatively 80% of the primary energy demand [2], brings a significant negative impact on the environment and on the climate. The main cause of these effects is the emission of greenhouse gases, which must be reduced for a sustainable future development. Possible solutions to reduce the environmental impact of the present primary energy sources can be:

- to improve the efficiency of the current energy technologies;
- to sustain the development of more efficient carbon capture and sequestration technologies;
- to diversify the energy sources by means of consistent investments on renewable technologies and nuclear energy.

The future exploitation of the nuclear fusion energy is one of the possible alternatives for the massive production of energy, although its complete industrial development still needs a long time to be achieved. The challenges faced by the realization of the fusion energy are related to the technological complexity for sustaining the extreme conditions needed by the reaction.

Research in fusion technology has been carried out worldwide since the beginning of the 20th century. In the last decades, Europe has been one of the most important player in the development of industrial fusion power plants for the production of nuclear energy. The reference documents to guide the development of the fusion technology, *"Fusion Electricity: A roadmap to the realisation of fusion energy"* [1] and *"European Research Roadmap to the Realisation of Fusion Energy"* [3], have been signed in 2012 and 2018, respectively. The two documents define the most important challenges to be overcome and the steps needed to reach this ambitious goal in the near future.

1.1 The nuclear fusion reaction

The nuclear fusion reaction involves the interaction of two light nuclei which are maintained in the physic state of plasma. During the reaction, they fuse together producing a heavier nucleus and releasing energy. The energy produced (ΔE) is obtained by the defect of mass (Δm) between the products and the reactants of the process, according to the well-known Einstein's equation:

$$\Delta E = \Delta m \cdot c^2 \tag{1}$$

in which the speed of light in vacuum is expressed by c.

Various fusion reactions are possible for the energy production involving nuclei of deuterium (D), tritium (T) and helium-3 (He^3).

The most interesting fusion reaction involves two deuterium nuclei, since the fuel is very abundant and cheap. The D-D pair may combine in two different set of products:

$$D + D \rightarrow He^3 + n + 3.27\ MeV \tag{2}$$

$$D + D \rightarrow T + p + 4.03\ MeV \tag{3}$$

The first alternative is the D-He^3 reaction for which one of the most important positive aspect is the production of only charged particles, a fact that is more suitable for the energy extraction. In addition, this feature allows to reduce the issue of the reactor structures activation.

$$D + He^3 \rightarrow \alpha + p + 18.3\ MeV \tag{4}$$

One of the most relevant drawbacks of this reaction is the very small availability of the He^3 on earth.

The third reaction considered involves deuterium and tritium nuclei (D-T).

$$D + T \rightarrow \alpha + n + 17.6\ MeV \tag{5}$$

The most relevant drawback of this reaction involves the fuel supply, which is solved developing a complex tritium production and extraction system based on lithium isotopes (Li^6 and Li^7) embedded in the structure of the reactor. The tritium used in the reaction is produced by the following processes:

$$Li^6 + n(slow) \rightarrow \alpha + T + 4.8\ MeV \tag{6}$$

$$Li^7 + n(fast) \rightarrow \alpha + T + n - 2.5\ MeV \tag{7}$$

The minus sign in (7) indicates that this reaction needs energy to be sustained.

The definition of the best solution for the energy production been performed considering the positive and the negative aspects of each reactions and the condition needed to sustain the fusion process inside the reactors. For this purpose, the nuclear fusion cross section is a quantity expressed in barn (1 b = 10^{-28} m^2) defined to characterize the probability that a particular reaction will occur[i]. The definition of the cross section takes into account lots of mechanisms and the detailed description of the theory behind this physical quantity is not developed here.

More relevant for the engineering point of view, the velocity average cross section $\langle \sigma v \rangle$ is defined considering also the velocity distribution of the reactants for the estimation of the reaction probability. This quantity is reported in Figure 1.1 for the three above mentioned fusion reactions as a function of the plasma temperature in the relevant operating conditions for nuclear power plant applications. The probability to obtain the D-T fusion reaction is several orders of magnitude higher if compared to the others reactions, in particular, in the region of the lower energy (~10 keV), indeed easier to reach in a fusion reactor.

[i] The concept of cross section is widely used in fission nuclear field [53] and not only for nuclear fusion applications.

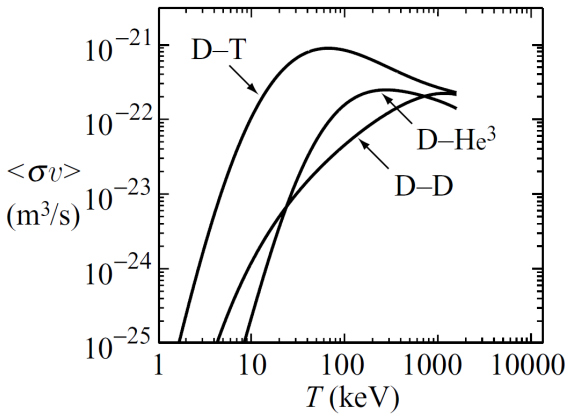

Figure 1.1: Velocity averaged cross section for the D-T, D-He^3, and D-D fusion reactions, as a function of the plasma temperature [4].

1.2 The nuclear fusion reactors

The technological strategy under development by Europe for the realization of a nuclear fusion power plant involves the magnetic confinement[ii] of the plasma inside the plasma chamber of the fusion reactor, which is designed in a tokamak configuration [5].

The ITER reactor, currently under construction in Cadarache (France), see Figure 1.2, represents largest nuclear fusion reactor designed for experimental purposes. ITER aims at demonstrating the scientific and technological feasibility of fusion energy production. In fact, the limits of the present magnetic confinement fusion machines (i.e. JET, K-STAR, JT-60, …) are still far from the characteristics needed in an industrial fusion power plant. The first ITER plasma is scheduled in 2025 [6], and the fully operative conditions will be reached in 2035 [7].

[ii] The alternative option for fusion technology is the inertial confinement. In this case suitable conditions for fusion are reached by heating and compressing the reactants typically in the form of pellets.

Figure 1.2: Aerial view of the ITER site in November 2018 [7].

Before the beginning of the construction of the commercial nuclear fusion power plants for the massive production of energy, the DEMO reactor will be the next step after ITER [8]. DEMO will be used to show the possibility to produce a relevant quantity of electrical power (300 – 500 MW) and to guarantee the safety and the environmental sustainability of the fusion energy production. The construction of the reactor is scheduled in the early 2040s and its operations are expected to start in the 2050s.

The main structures of the present fusion reactor are sketched in Figure 1.3. The plasma is confined in a void region located at the centre of the reactor, which is called plasma chamber, by means of suitable magnetic fields generated by a complex system of magnets that surrounds the reactor. The plasma is physically separated by the external environment using the blanket (also used for the production of the tritium) and by the vacuum vessel (used to maintain the suitable vacuum condition in the plasma chamber). Externally, the complex system of magnets is placed inside a proper cryostat that surrounds the overall structure. To complete the power plant, outside the cryostat, the balance of plant is used to deliver the coolant to all the components of the reactor and to produce electrical power.

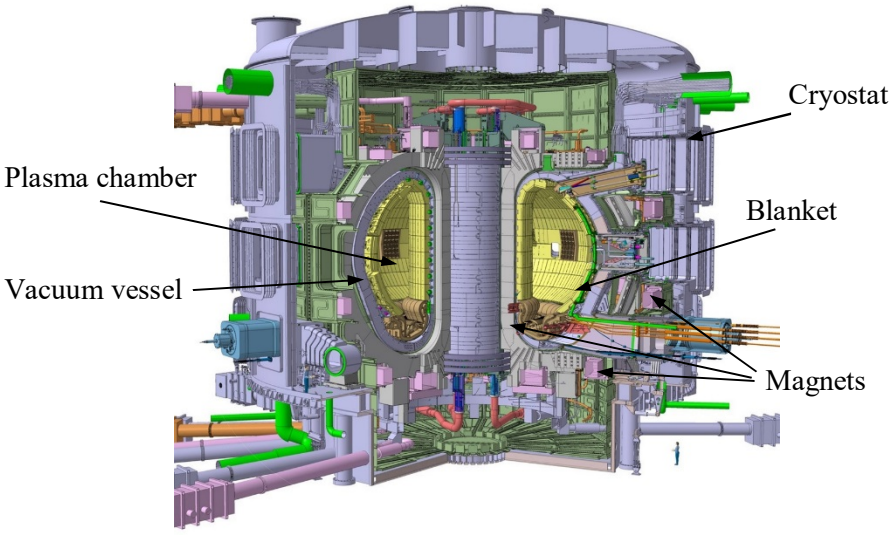

Figure 1.3: Sketch of the main components of the ITER fusion reactor [9].

For the production of a relevant amount of energy, the power balance of the nuclear reactor is very important in the development of industrial power plant and to figure out the complexity of the systems need to sustain the fusion process. Two power balances are defined:

- the power balance of the plasma, which consider only the reactions present inside the plasma;
- the power balance of the reactor, which includes also the energy transformation processes.

Focusing on the energy balance in the plasma, the ignition condition[iii] is achieved if the power developed inside the plasma by the high energy alpha particles (S_α), produced in the reaction, is sufficient to balance the power losses by the Bremsstrahlung effects (S_B)[iv] and by the thermal conduction phenomena which occurs inside the plasma (S_k):

$$S_\alpha = S_B + S_k \tag{8}$$

Developing the power balance described in (8), the definition of the ignition condition sets the physical requirements need to obtain a self-sustaining plasma.

[iii] It is called ignition the condition for which the self-sustained and no external energy sources are needs to maintain the fusion reactions.

[iv] The Bremsstrahlung effect is the loss of energy in the form of electromagnetic radiation produced by the deceleration of a charged particle when deflected by another charged particle.

The ignition condition is expressed by the product between the density of the plasma (n), its temperature (T) and the confinement time[v] (τ_E), called "triple product". The comparison of the values of the triple product as a function of the plasma temperature is shown in Figure 1.4, for the three above mentioned fusion reactions. The triple product for the D-T reaction in the range of the lower temperature (~10 keV) is a couple of orders of magnitude lower with respect to the other two reactions. This behaviour confirms that easier conditions are required to obtain the ignition with the D-T plasma with respect to the other two. The Lawson criterion is defined as the minimum value of the triple product, which in the D-T is obtained in correspondence with the plasma temperature of ~15 keV (~10^8 K) [4]. The temperature expressed in K is related to the temperature expressed in eV, which indicates the energy of the electrons in the plasma, by the Boltzmann constant k_B.

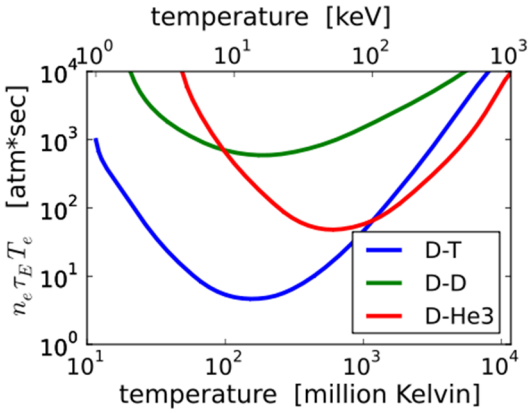

Figure 1.4: Variation of the triple product as a function of plasma temperature for D-T, D-D, and D-He^3 fusion reactions [10].

Considering now the power balance of the entire reactor, it takes into account also the processes used to extract the thermal energy from the plasma for the electricity production and the systems needs to sustain the fusion reactions. Two gain parameters are defined for this purpose, called physic gain factor (Q) and engineering gain factor (Q_E), which are expressed by (9) and (10), respectively.

$$Q = \frac{P_{th,out} - P_{th,in}}{P_{th,in}} \tag{9}$$

[v] For a general system, the confinement time measures the rate at which a system loses energy to the environment.

$$Q_E = \frac{P_{el,out} - P_{el,in}}{P_{el,in}} \tag{10}$$

in which $P_{th,out}$ is the total thermal power extracted from the plasma, $P_{th,in}$ is the heat power injected inside the plasma. The electric power produced by the reactor is given by $P_{el,out}$, while $P_{el,in}$ is the electric power required to drive the external sources used to inject energy into the plasma. In the ignition condition the two gain factors are both infinite because the plasma does not need external energy to be sustained.

Since the ignition is the ideal final state of the plasma for the production of energy, the presence of the heating systems plays an important role on the achievement of the working conditions of the fusion power plant.

The plasma heating systems

As described in the previous section, the ignition state of the plasma is reached if a suitable value of the triple product between density, temperature and confinement time is reached. More in detail, this condition is expressed by:

$$n\,\tau_E T = \frac{12\,k_B}{E_\alpha}\frac{T^2}{\langle\sigma v\rangle} \tag{11}$$

in which k_B is the Boltzmann constant, and E_α is the energy of the alpha particles produced in the fusion reactions. T is the plasma temperature and $\langle\sigma v\rangle$ is the velocity averaged cross section of the reaction.

The temperature required to obtain plasma ignition (~15 keV), is reached with the use of three main plasma heating processes, see Figure 1.5, relying on:

- ohmic heating;
- radio frequency;
- neutral beam injection.

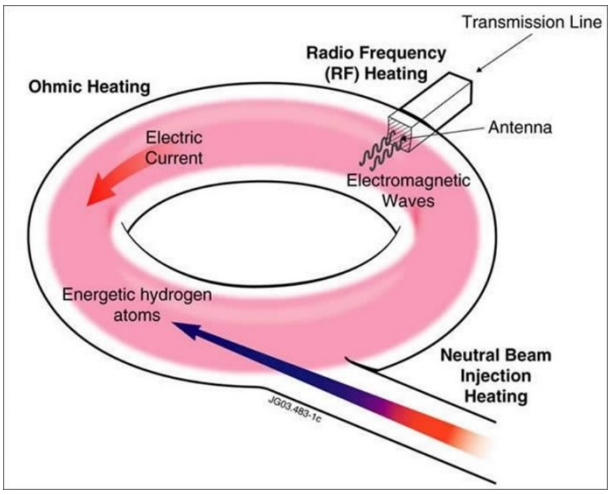

Figure 1.5: Plasma heating strategies adopted in a fusion reactor [7].

Due to the physical processes involved and the feedback of the plasma to the external actions, the first part of the heating process is performed by a combination of ohmic heating, radio frequency heating and neutral beam injection. The aim of these systems is to rise the plasma temperature up to about 5 – 7 keV. Above this threshold, the power provided by alpha particles[vi] is dominant, heating the plasma up to the temperature required for ignition [4].

1.3 Application of radiofrequency in fusion technology

The radio frequency heating system is relevant for the study performed in this work, dealing with the use of Radio Frequency (RF) waves to deliver energy into plasma. Additionally, the RF waves are used to drive a steady state non-inductive current inside the plasma to control plasma instabilities and to support the start-up phase of the reactor. The RF system works according to wave-particle resonance conditions occurring between injected waves and plasma particles. The energy exchange, between the RF and the plasma, occurs if the frequency of the waves matches the gyro-frequency of the plasma particles, or one of its harmonics.

Figure 1.6 shows the sketch of the system used to produce the RF waves. The RF source, which characteristics depend on the waves frequency needed into the plasma, is driven by a high-voltage power supply connected to the electric grid. The waves are injected into the plasma by means of the launcher (a sort of big antenna facing to the plasma), which is connected to the source by the transmission line.

[vi] The alpha particles that are produced by the D-T fusion reaction are characterized by a kinetic energy of ~3.5 MeV.

The choice of the technologies adopted for the launcher and for the transmission line depend again on the characteristics of the RF source needed in the reactor.

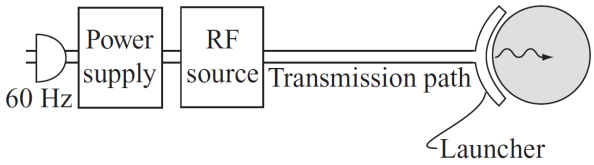

Figure 1.6: Sketch of the diagram of an RF system [4].

The general classification of the RF sources is performed based on the frequency (f) that they can produce:

- high-power vacuum tubes: f < 100 MHz
- klystrons: f ~1 – 10 MHz
- gyrotrons: f ~10 – 300 GHz

For example, for a magnetic field of 5 T with D plasma, the gyro-frequency[vii] of the electrons is 140 GHz and for the ions is 38 MHz. The plasma characteristics require that to obtain suitable waves to perform the resonance interactions with the ions, high-power vacuum tubes are needed, while to obtain the interactions with the electrons, the gyrotrons are used. In present fusion machines, long pulse and Continuous Waves (CW) gyrotrons, characterized by output power of 100 – 960 kW and frequencies of 28 – 170 GHz, are successfully used. The gyrotrons are mainly used for the Electron Cyclotron Resonance Heating (ECRH) and the Electron Cyclotron Current Drive (ECCD) for the control of plasma instabilities in systems with power up to 4 MW [11].

Figure 1.7 shows the Electron Cyclotron (EC) system developed for ITER [12]. The system includes a power supply of ~50 MW that feeds 24 gyrotrons for an overall output power of ~24 MW in the form of RF waves. The transmission lines used to connect the gyrotron to the reactor are ~160 m long and end with 5 launchers, used to deliver ~20 MW of power inside the plasma.

[vii] The gyro-frequency is defined by $f_c = \frac{\omega_c}{2\pi}$, in which ω_c is the rotational speed.

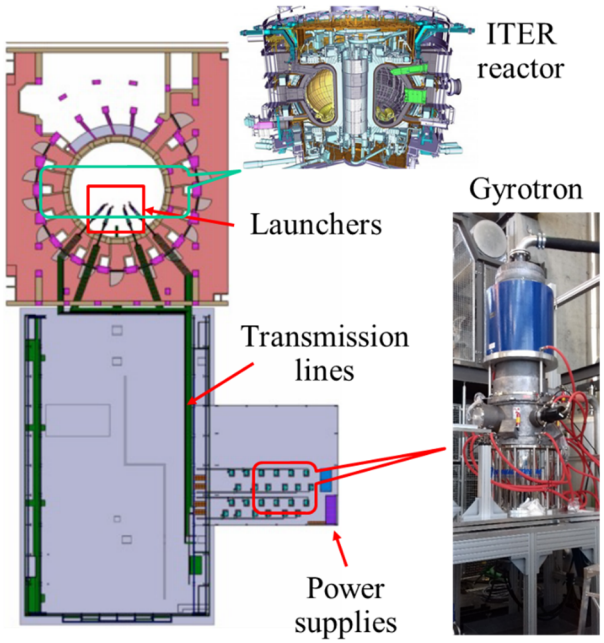

Figure 1.7: Scheme of the Electron Cyclotron (EC) system in ITER (adapted from [12]).

1.4 The working principle of the gyrotron

The layout of a gyrotron is sketched in Figure 1.8: in the bottom region of the gyrotron, the Magnetron Injection Gun (MIG), or simply electron gun, emits an annular electrons beam with proper velocity and direction. The MIG (see Figure 1.9a) consists of a cathode where a perfectly circular emitter ring made of tungsten is heated up to ~1000 °C in order to extract the electrons. To complete this part of the gyrotron, one (diode gun) or two (triode gun) anodes are present based on the features of the MIG. The electrons beam produced by the MIG is accelerated thanks to the electrical field produced in the bottom region of the gyrotron, and then the beam moves upward inside the beam tunnel (see Figure 1.9b). In this hollow truncated cone component, the parasitic oscillation of the beam is suppressed by the corrugation on the inner surface of the beam tunnel.

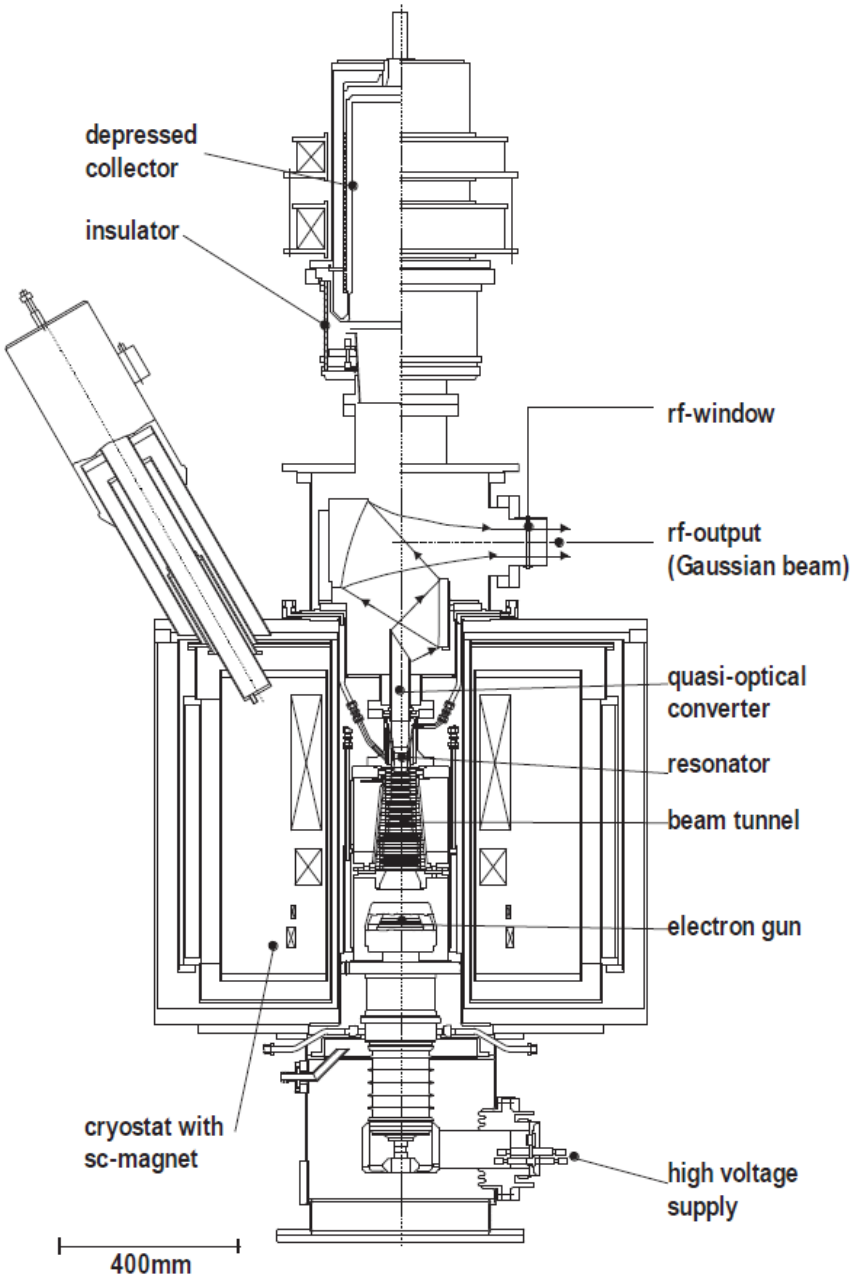

Figure 1.8: Schematic layout of a gyrotron [13].

After the beam tunnel, the electrons moves through the cavity of the gyrotron, which is the relevant part of the gyrotron for this work. In the cavity region, the electrons beam interacts with the resonating surface of the component producing the RF waves with the desired energy. In the case of radial output gyrotron (as shown in Figure 1.8) used in the ITER EC system, the launcher (see Figure 1.9c) is installed after the cavity to obtain the desired characteristics of the RF waves, which

are then radially transmitted outside the gyrotron by means of the vacuum window. The vacuum window is coupled with the transmission lines which finally deliver the RF inside the plasma by means of suitable antennas. After the resonating interaction inside the cavity, the spent electrons beam moves unperturbed crossing the launcher region and reaches the upper part of the gyrotron. On the top of the gyrotron structure the collector is used to collect the electrons and to dissipate the residual energy of the beam, which is >50% of the initial one.

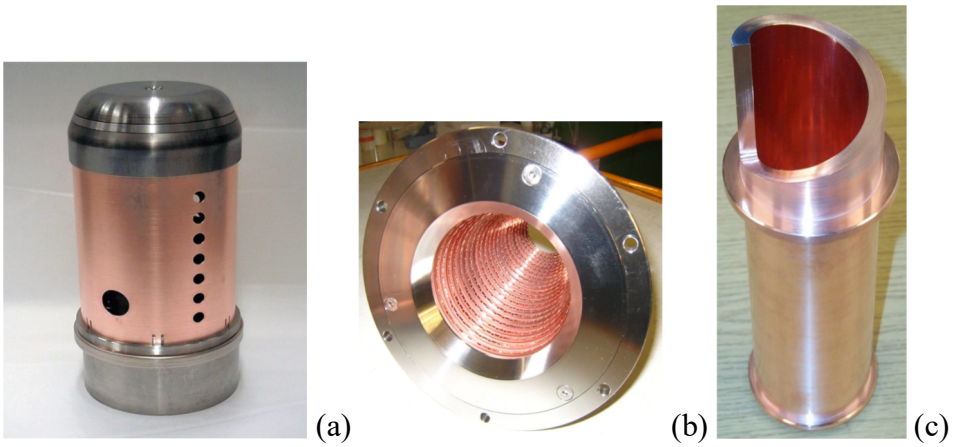

Figure 1.9: Pictures of (a) the electron gun, (b) the beam tunnel and (c) part of the quasi-optical converter [14].

In the different components of the gyrotron, the motion of the electrons is guided by proper electromagnetic field lines produced by a complex system of magnets. In particular, the magnetic field generated inside the cavity region is carefully chosen in order to obtain suitable resonating interactions with the internal surface of the resonator, aimed to produce the RF waves with the desired characteristics in terms of frequency and energy. Inside the cavity region, the electrons of the annular beam follow a helical path around the line of force of the external field, initially with a random phase (see Figure 1.10a). The kinetic energy transfer from the electrons motion to the electromagnetic waves occurs if their phase becomes synchronous in a condition called “phase bouncing” (see Figure 1.10b). This situation can occur since the electron cyclotron frequency (ω_c) depends on the electron energy, as shown by (12):

$$\omega_c = \frac{e\,B_0}{m_e\,\gamma} = \frac{\Omega_0}{\gamma} \tag{12}$$

in which -e and m_e are the charge and the rest mass of the electron, respectively, B_0 is the magnetic field in the resonator region, and $\Omega_0 = {}^{e\,B_o}/_{m_e}$. The relativistic factor is defined by $\gamma = {}^{E}/_{m_e\,c^2} = {}^{1}/_{\sqrt{1-(v/c)^2}}$, in which E is the total energy of the electron.

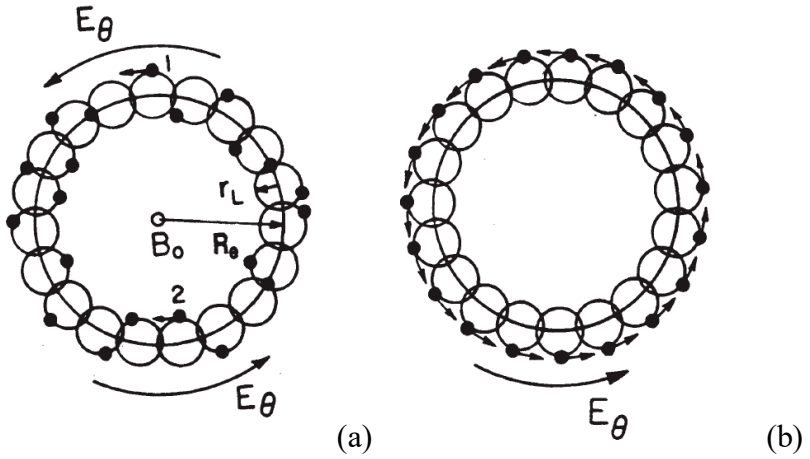

Figure 1.10: Annular electron beam trajectories before (a) and after (b) the interaction inside the cavity [15].

In the first stage of the cavity region, the presence of a transverse electric field accelerates or decelerates the electrons according to their position in the beam, gaining or losing energy with random phasing, thus, no net energy exchange with the RF can occur. The phase bouncing is achieved if the wave frequency is slightly larger than the initial value of the cyclotron frequency, developing an instability on the beam which allows to synchronize the orbits of the electrons, as shown in Figure 1.10b. In this condition, a net energy exchange with the RF field in the region of the cavity is obtained.

The explanation of the phase bunching process is out of the scope of this thesis and its description is far from a complete discussion of this phenomena. Other energy transfer mechanisms are also present inside the gyrotron, as discussed in [16]. More complete and detailed descriptions of the working principles of the gyrotron are present in [11] - [17].

1.5 The cavity of the gyrotron

As discussed in the Section 1.4, inside the cavity the interaction between the electrons beam and the magnetic field takes place to produce suitable RF waves that are

finally used on the plasma. In this paragraph, a general overview of the geometrical characteristics of the gyrotron cavities studied in this works are discussed. The differences on the cavity layout depend on the power of the gyrotron on which they are installed and the cooling configuration of the component.

The section of the CAD model of the cavity and of the launcher[viii] designed for the 170 GHz, 1 MW gyrotron for the ITER EC system, studied in the first part of this work, is shown in Figure 1.11. The general description of the resonating structure is also valid for the cavity of the 170 GHz, 2 MW gyrotron equipped with the coaxial insert designed for DEMO, studied in the last part of this work. The resonator of the cavity and the launcher are surrounded by an external stainless steel region, which is used for structural purpose. The coolant is sub-cooled water in forced flow at 6 – 10 bar and ~40 °C, which flows in the gap region obtained between the external surface of the resonator and the internal surface of the stainless steel structure.

One of the issues of the 1 MW cavity designed for ITER deals with the position of the outlet pipe of the cooling circuit of the cavity, which is located after the end of the resonator (this is not valid for the CAD model used for the 2 MW cavity designed for DEMO). In order to simulate accurately the thermal behaviour of the ITER gyrotron cavity, the CAD model used in the simulations includes also the initial part of the launcher. This strategy is used to modify as less as possible the coolant behaviour in the outlet region of the cavity, due to the variation of the cooling circuit. Moreover, the position of the inlet and of the outlet pipes is not in reciprocal symmetric position, then a full 3D simulation is needed due to the impossibility to perform any sort of domain reduction thanks to the symmetric domain[ix].

[viii] The launcher is presented with the cavity because the two components are strictly connected and the definition of the cooling circuit of the cavity will be performed based on the complete assembly.

[ix] In the simulation of the 1 MW cavity equipped with RRs (see Chapter 3) the domain is reduced at the level of the resonator in order to take advantages of the symmetry condition to reduce the computational cost.

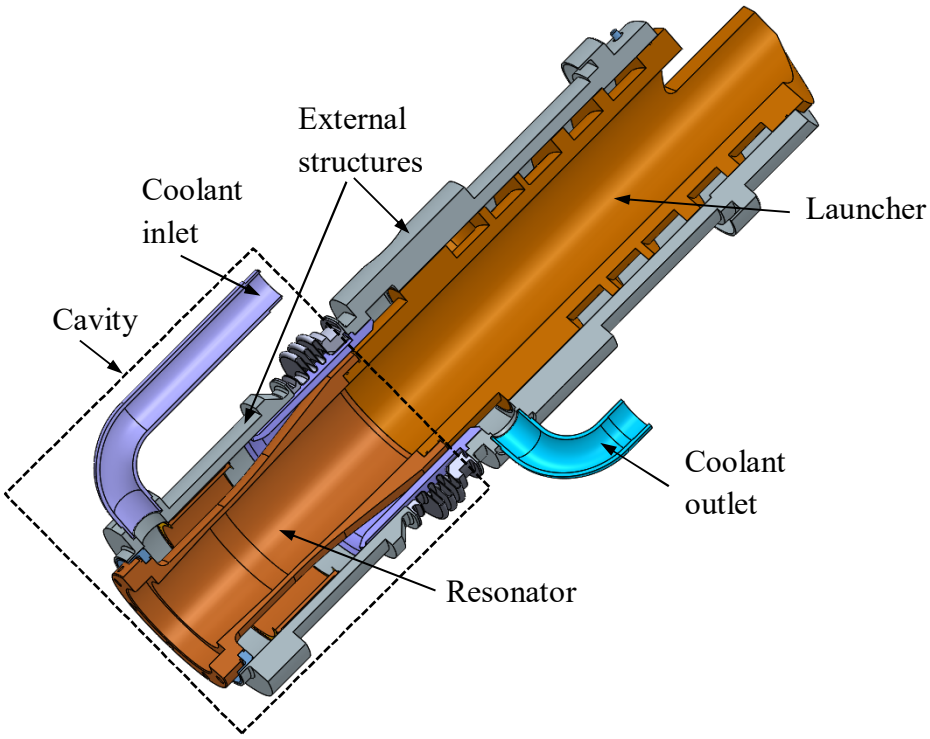

Figure 1.11: Cross section of the CAD model of the cavity and launcher assembly for the 170 GHz, 1 MW gyrotron for ITER.

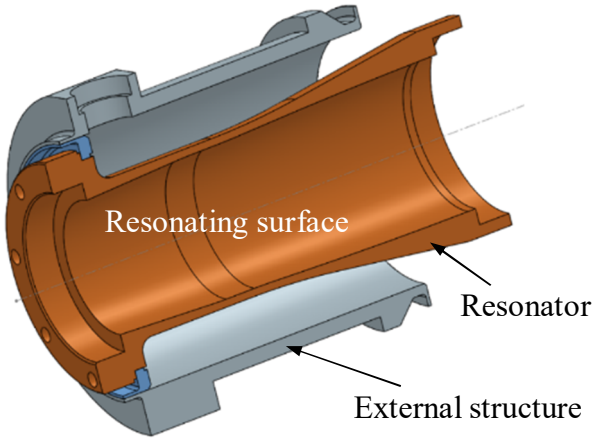

Figure 1.12: Cross section of the gyrotron cavity.

In order to highlight the resonating region, the cross section of the cavity of the 170 GHz, 1 MW gyrotron is shown in Figure 1.12, in which only the resonator and the stainless steel structure are shown. The launcher, the inlet and the outlet pipes are removed for clarity. The cavity resonator is a hollow cylindrical region made of Glidcop®. This material is a copper-aluminum alloy widely used in this kind of

applications thanks to the higher stress resistance at high temperature if compared with the pure copper [18]. The resonator is in contact with the external stainless steel structure in the bottom part of the cavity closer to the inlet pipe and it is in contact with the launcher on the opposite side. The axial length of the resonator is ~10 cm and the internal radius of the heated surface of the resonator is ~2 cm[x] (these values are still valid to have an indication on the dimensions of the cavity for the 2 MW gyrotron).

DEMO needs a set of gyrotrons with higher power characteristics due to the higher energy requested in this type of reactor. In order to increase the gyrotron performances, more complex resonating structures are used to increase the power stored in the RF waves. In this direction, the 170 GHz, 2 MW gyrotron involves the presence of the coaxial insert in the lower part of the gyrotron. The coaxial insert starts in the bottom part of the gyrotron crossing the entire length of the cavity and the first part of the launcher, as shown in Figure 1.13. The most important advantage gained by the presence of the coaxial insert is related to the reduction of the modes competition inside the cavity region, with a consequent more stable operation with larger cavity diameter [11]. The disadvantage is the higher technical complexity of the lower part of the gyrotron structure involving the electron gun, the beam tunnel and the cavity region.

The cavity of the coaxial gyrotron for DEMO is currently under development at KIT and its study is shown in Chapter 5.

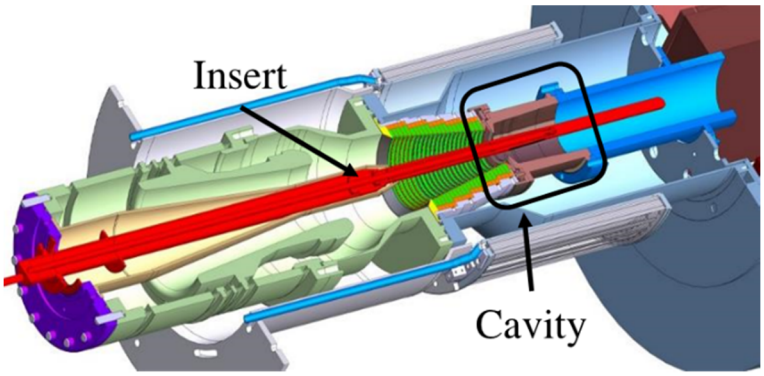

Figure 1.13: CAD model of the lower part of the 2 MW coaxial gyrotron under development for DEMO.

The most important difference with respect to the cavity developed for ITER is related to the position of the outlet pipe of the cooling circuit: it is placed before the

[x] Technical specifications provided in a confidential form.

end of the resonator for the DEMO gyrotron, while for ITER it is located in the first part of the launcher region. This allows to remove completely the launcher region in the definition of the simulations model (see Figure 1.14).

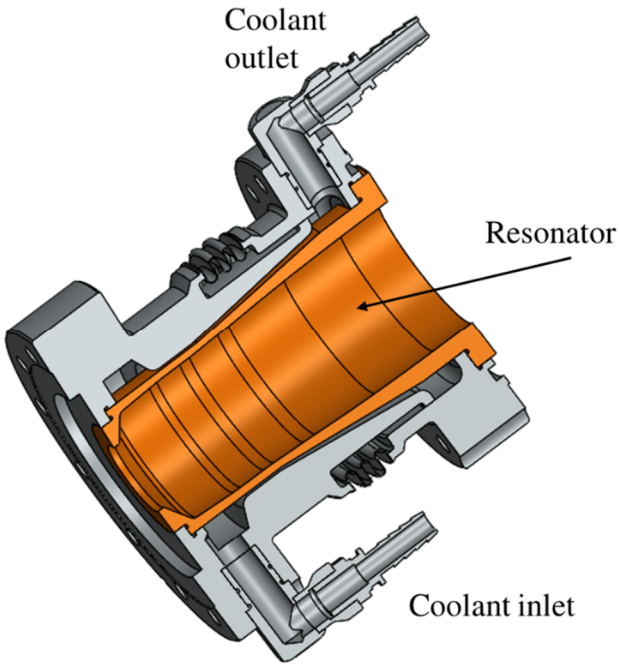

Figure 1.14: Cavity region of the 170 GHz, 2 MW gyrotron for DEMO.

The detailed descriptions of the cooling strategy adopted in the cavity for ITER are discussed in the Chapter 3 and Chapter 4 while, as far as the coaxial cavity for DEMO is concerned, details are reported in Chapter 5.

1.6 Aim of the thesis

Recalling the central role of the cavity region of the gyrotron in the production of RF waves with the desired characteristics to obtain suitable interactions with the plasma in the fusion reactors, this work presents a multi-physics computational tool developed to perform thermal-hydraulic, thermo-mechanical and electro-dynamic analysis of the resonating structure of the cavity during the operation of the gyrotron, to capture and to predict its operating point.

The different aspects of the tool are presented in this work showing the simulations' results performed on different strategies adopted for the optimization of the cooling aspect of the cavity components. For each cooling design, the positive and

negative features are highlighted to determine the best strategy to be applied for the study of the present gyrotrons and for their development [19].

Chapter 2

The MUlti-physiCs tool for the integrated simulation of the CAvity

The MUlti-physics tool for the integrated simulation of the Cavity (MUCCA) started being developed since 2016 within the framework of the PhD activity object of this thesis, thanks to the collaboration between Politecnico di Torino (PoliTo) and the Karlsruhe Institute of Technology (KIT). Fusion for Energy and Thales Electron Devices, under the coordination of the EUROfusion consortium, were also involved in the project. The MUCCA tool aims at obtaining an iterative self-consistent procedure for the evaluation of the working condition of the cavity to be used in the gyrotrons development for nuclear fusion applications.

The iterative process implemented in the MUCCA tool is represented in Figure 2.1: the transient or steady state simulation of the Thermal-Hydraulic (TH) behavior (see Appendix B), followed by the stationary Thermo-Mechanical (TM) analyses are performed by PoliTo, using the commercial software STAR-CCM+® [20], on the relevant parts of the gyrotron cavity. The thermal deformations computed on the resonating surface of the cavity are used to evaluate the modification of its radial profile, which is used as input in the Electro-Dynamic (ED) code EURIDICE® [21] managed by KIT. EURIDICE® is used to estimate the interaction between the electrons and the magnetic field inside the cavity and to compute the heat load on the resonating surface considering the deformations previously ob-

tained in the TM module. The updated heat load becomes the driver of the TH analysis for the next iteration of the MUCCA tool. The iterative procedure continues up to the steady state operation of the cavity [22].

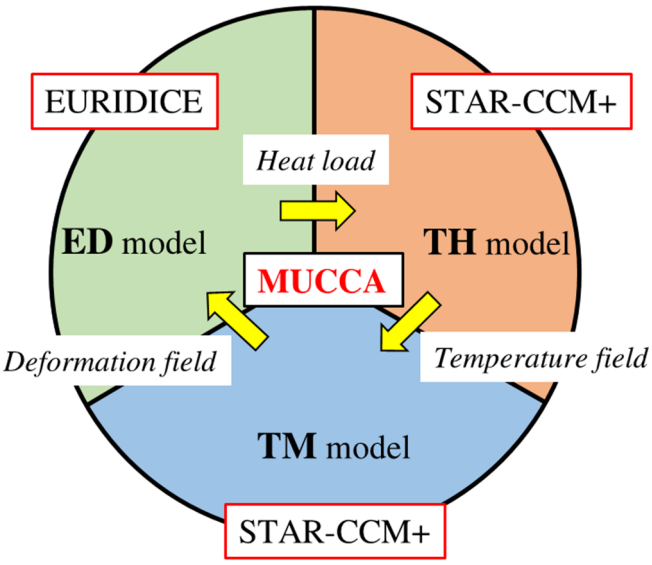

Figure 2.1: Iterative processes and models interactions in the MUCCA tool.

Either transient or steady state simulations are conceivable for the evaluation of the final thermal response of the cavity. In the first method, the TH simulations are performed with transient approach in order to take into account the thermal capacity of the solid structure of the cavity, which is not taken into account in the steady state approach for the evaluation of the temperature field. With both timing strategies, the heat load applied on the resonator is fixed for a specific iterative step of the MUCCA tool. In order to verify the goodness of both approaches, a set of preliminary simulations is performed on the 170 GHz, 1 MW gyrotron for ITER applying the two time approaches. The results of the MUCCA tool show that the same final working condition of the cavity is reached starting from the same initial condition (see Appendix B for details). This behavior shows that the two time strategies are mutually consistent for the evaluation of the steady state operation of the cavity. The choice of the timing approach to be applied in the TH simulations of the MUCCA tool is performed in this work based on the information required for the description of the cavity and the computational cost of each procedure. The drawback of the steady state simulation approach is the loss of the transient description of the components, since it requires a small amount of iterations of the MUCCA tool (less than five) in order to obtain the final results of the cavity. Vice versa, the transient approach is used to monitor the time evolution of the components using

much more (order of 20) iterations of the MUCCA tool to reach the steady state cavity working condition.

2.1 The Thermal-Hydraulic model

In the MUCCA tool, the TH model reproduces the 3D geometry of the resonator, of the coaxial insert and of the cooling circuit of the cavity[i].

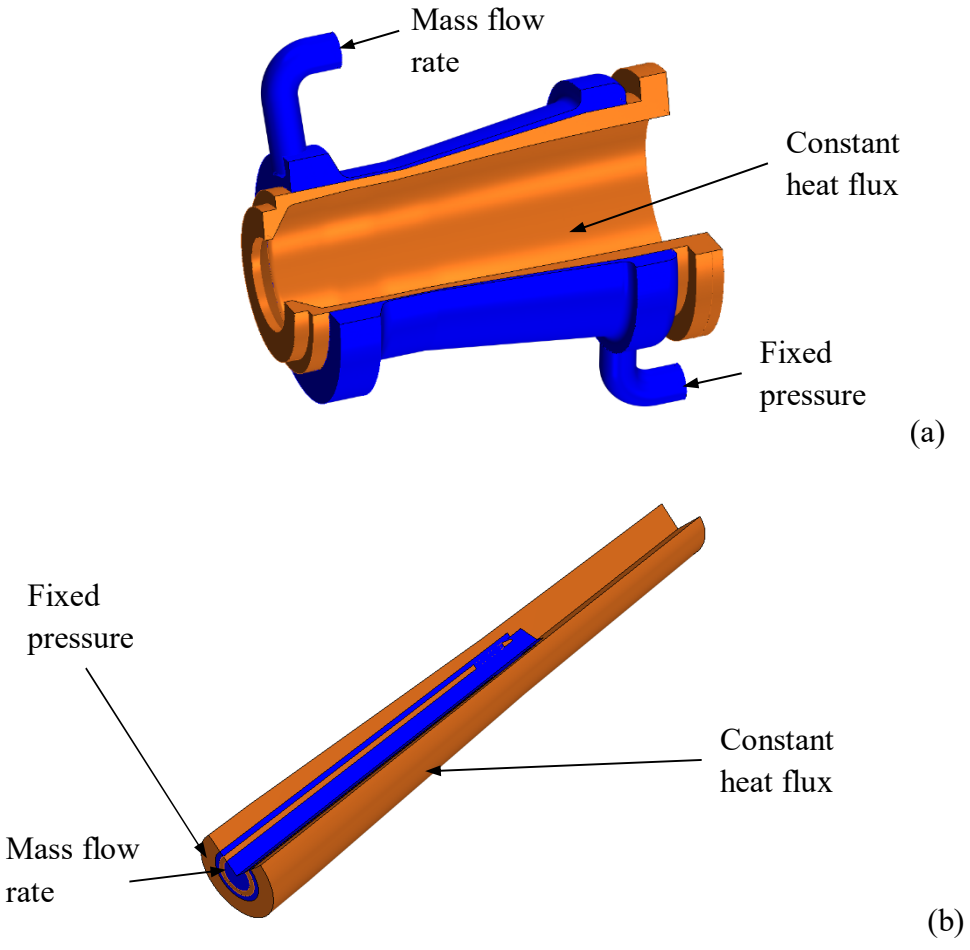

Figure 2.2: Cross section of the (a) resonator and of the (b) coaxial insert domains in which the TH boundary conditions are reported.

[i] Geometrical simplifications are performed on the CAD model of the cavity using the software SolidWorks®. In addition, the computational domain is also reduced as much as possible, keeping unchanged the relevant features of the structures modelled.

The boundaries (see Figure 2.2) and the initial conditions used in the TH simulations are the following:

- a constant coolant mass flow rate at a fixed temperature is applied on the inlet section of the cooling circuit of the cavity. These values depend on the specific cavity studied;
- a fixed pressure is set on the outlet section of the cooling circuit of the cavity and of the insert. Its value is defined in order to compute an absolute pressure on the inlet section of the model which is in agreement with the specification of each gyrotron cooling circuit;
- the external surfaces of the solid structure of the cavity and of the coolant are adiabatic with respect to the environment;
- a fixed heat flux is applied on the internal surface of the resonator and of the launcher. In the simulations of the coaxial insert, the heat load is applied on its external surface;
- the initial temperature of the solid structures and of the fluid region are set equal to the inlet temperature of the coolant. This condition assumes that the thermal equilibrium between fluid and solids regions is achieved at the beginning of the simulation procedure.

Turbulent flow conditions are observed in the simulations performed in this work. The turbulence behavior of the fluid flow is modelled with the k-ω SST (Menter) model [23] applying the all-y+ wall treatment [20]. The computational grid is defined according the specification required by the turbulence model used and the grid independence analysis have been performed on the resulting temperature distribution of the heated surfaces of the cavity and on the pressure drop computed between the inlet and the outlet section of the coolant.

In order to evaluate the effects of the boiling phenomena, the single-phase Rohsenow boiling model [24] is used. This model evaluates the heat extracted by the coolant due to boiling from the Rohsenow correlation described by the Equation (13) [25].

$$q_{bw} = \mu_l h_{lat} \sqrt{\frac{g(\rho_l - \rho_v)}{\sigma}} \left(\frac{c_{pl}(T_w - T_{sat})}{C_{qw} h_{lat} Pr^{n_p}} \right)^{3.03} \tag{13}$$

in which μ_l is the dynamic viscosity of the coolant, h_{lat} is the latent heat of vaporization of the coolant which is evaluated at a relevant value of the pressure for

the cavity (e.g. the pressure computed in the position in which the boiling phenomena is expected), g is the gravitational acceleration, ρ_l and ρ_v are the liquid and vapour density, respectively. σ is the surface tension, c_{pl} is the liquid specific heat, $T_w - T_{sat} = \Delta T_{sat}$ is the local difference between the wall temperature and the saturation temperature of the coolant, C_{qw} is an empirical coefficient depending on the liquid-solid interface conditions [26] (materials, surface conditions, …), and $Pr = \mu \frac{c_p}{k}$ is the Prandtl number with its exponent n_p. The exponent of the Prandtl number is set equal to one [27].

The use of this simulation strategy is justified by the low impact on the flow dynamics of the vapor bubbles generated at the solid-coolant interfaces due to the high velocity of the coolant observed. In addition, this model is very easy to manage due to the fact that the coolant is simulated as single phase fluid, reducing considerably the computational cost of the simulations.

The coolant properties are defined as a functions of the pressure and the temperature, according to IAPWS-IF97 standard library [28]. The thermal properties of the copper [29] and of the Glidcop® [30] are defined as a function of the temperature (see Appendix A).

2.1.1 The Raschig Rings cooling strategy: model and calibration

The cooling strategy adopted in the cavity of the 170 GHz, 1 MW gyrotron for ITER is characterized by a porous medium made by Raschig Rings (RRs), which cross section is shown in Figure 2.3. The porous medium is applied to reduce the temperature of the resonator of the cavity increasing the heat transfer at the solid-water interface in the region in which the heat load is higher. The RRs are small hollow cylinders made of copper and characterized by diameter and length dimensions in the order of the millimeters[ii]. The cylinders are randomly injected inside the cavity during the assembling process of this component is performed by Thales Electron Devices. At the end of the manufacturing procedure, the RRs are brazed together to produce a compact porous like block. A preliminary simulation procedure implemented in STAR-CCM+® is used to create the RRs region (details are described in Appendix E) which is applied on the external part of the cavity resonating region.

[ii] Technical specifications provided in a confidential form.

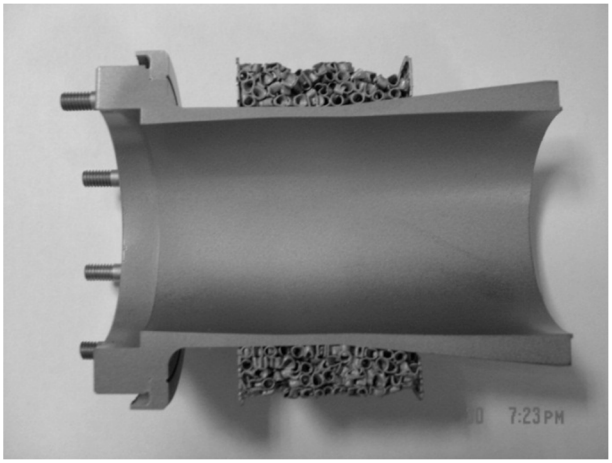

Figure 2.3: Picture of the cut section of the cavity equipped with RRs [31].

Due to the complexity of the cooling strategy adopted in the ITER cavity, a proper calibration of the TH simulation is needed. For this purpose, a test campaign on a planar cavity mock-up equipped with RRs has been performed by Areva in the FE200 test facility of Le Creusot (France) in 2015 [31]. The details of the test facility and of the measurement system employed during the campaign are described in Appendix C. The calibration process aims at determining the best setting of the thermal parameters to be used in the simulation of the full size cavity for the ITER gyrotron. The thermal conductivity of the RRs region (k_{RR}) is chosen as the calibration parameter, which is set to reproduce the temperature outcomes of the experiments. Due to the lack of information on the coefficient C_{qw} for the water-Glidcop® interface for the RRs cooling configuration, the value 0.013 is assumed in the boiling model [32]. The temperature measured by a pyrometer on the target region of the mock-up (see Appendix C) is used as reference parameter for the calibration process.

A more detailed calibration study of the RRs thermal conductivity is performed after the development of the model, comparing the outcomes of the MUCCA tool applied on the full size cavity equipped with RRs with the results obtained during the experimental campaign on the 170 GHz, 1 MW gyrotron, performed by KIT in 2016 (see Paragraph 3.3).

Taking advantage of the tests performed on the mock-up equipped with RRs, the pressure drop computed are used for the validation of the pure hydraulic models adopted in the simulations.

The mock-up of the cavity equipped with Raschig Rings

The geometry used in the simulation of the mock-up equipped with RRs is shown in Figure 2.4 [32]. The target region of the mock-up, made of Glidcop®, is located in the lower part of the assembly and it is directly in contact with the RRs region. The definition of the RRs region is performed simulating the random injection of the hollow cylinders in a hexahedral block with dimension ~28 mm × ~33 mm × ~13 mm. The RRs block is finally placed above the circular target region of the mock-up as shown in the figure below.

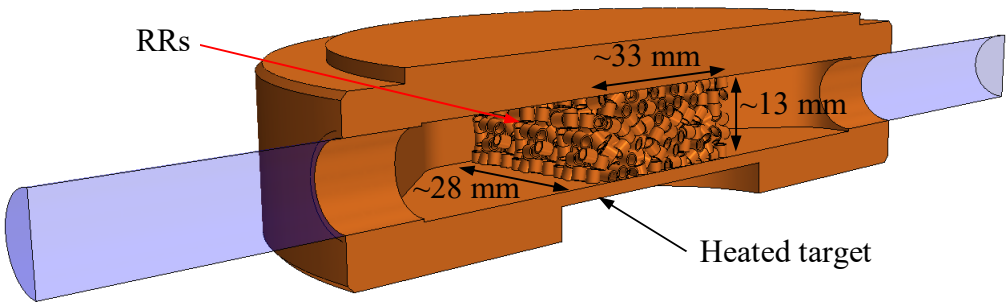

Figure 2.4: CAD drawing of the mock-up equipped with RRs used in the simulations for the validation and preliminary calibration of the TH models.

The pure hydraulic results of the test campaign are shown in Figure 2.5 in terms of pressure drop computed between the inlet and the outlet section of the mock-up equipped with RRs. The evaluation of the pressure drop has been performed by Areva, when the target is not subject to any thermal loads [31]. This is done to prevent the change of the water properties with the temperature and, eventually, the effects of boiling. The fit curve obtained (see red line in Figure 2.5) well reproduces the experimental results with a R^2 coefficient of 0.999.

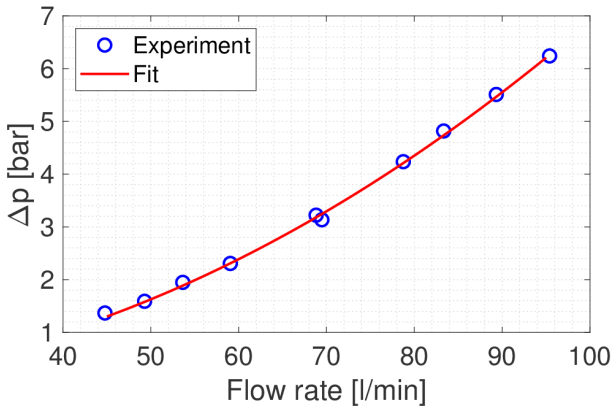

Figure 2.5: Experimental results of the pressure drop in the cavity mock-up equipped with RRs (blue circles) and fit curve (red line).

The temperatures measured by the pyrometer on the target surface of the mock-up are shown in Figure 2.6. The results show a difference of ~10 °C – 15 °C between the measurements at 80 l/min and the other series at lower mass flow rates. The consistent discrepancy observed is not justified by the higher mass flow rate with respect to the other experimental conditions. This behaviour can be related to the range of operation of the pyrometer during experiment that is out of the calibration region of the instrument. Figure 2.7 shows the curve obtained during the calibration process performed independently by Areva before the experimental campaign on the mock-up. As shown, the measurement of the pyrometer are reliable only for target temperature above 350 °C.

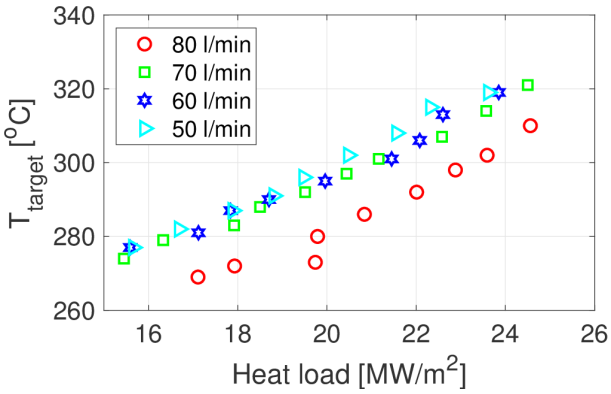

Figure 2.6: Temperature measured during experiment by the pyrometer at different values of the incident heat flux, for different values of the mass flow rate.

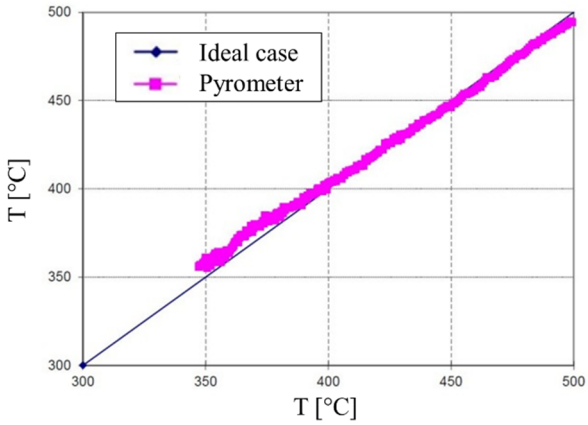

Figure 2.7: Characteristic curve of the pyrometer available during the calibration performed with the sample cool-down procedure (from [31]).

Preliminary pure hydraulic simulations are performed on the mock-up equipped with RRs for the validation of the models adopted in the MUCCA tool. The validation of the turbulence model is performed comparing the computed pressure drop curves and the measurements collected on the mock-up (see Figure 2.8) during the hydraulic tests carried out at the FE200 facility in 2015. In order to be consistent with the experimental pressure drop evaluations, the CFD simulations have been performed when the target is not subject to any thermal loads. The computed results are in very good agreement (maximum relative error < 3.5%) with the experimental mass flow rates used during the tests (i.e. 60 – 90 l/min).

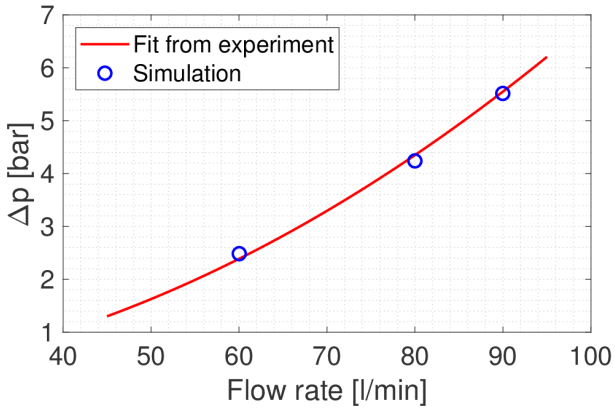

Figure 2.8: Pressure drop curve obtained from the polynomial fit of the experimental campaign (red line) and CFD simulation results (blue circles), for the mock-up equipped with RRs.

The calibration of the thermal simulations is related to the working condition of the pyrometer which is used to monitor the temperature on the target surface of

the mock-up (see Figure 2.7). In order to be consistent with the information available from the test, the calibration process is performed considering this threshold temperature as the reference value to be obtained in the test of the worst case scenario, since the temperature read on the target by the pyrometer is always below this limit. In this condition the simulation is performed adopting the maximum heat load and the minimum mass flow rate used during the campaign. The heat load applied on the mock-up is produced by an electron gun and it is characterized by a square footprint of 33 mm of side, located in the center of the circular target surface of the mock-up.

The temperature of the target region obtained during the calibration process of the TH simulations is shown in Figure 2.9 and compared with the outcomes of the 2015 test campaign. The calibration of the thermal conductivity is performed on the case characterized by an inlet mass flow rate of 50 l/min, in which the heat load of 24 MW/m^2 is applied on the target (see Figure 2.9a). The results of the calibrating process show that the value of 2000 W/m K (instead of the nominal value of ~400 W/m K) gives the required target temperature of 350 °C. This value is used as lower bound for the definition of the RRs thermal conductivity, to be used in the calibration process performed on the 1 MW gyrotron discussed in Chapter 3. The setup obtained at the end of the calibration is maintained unchanged in the other simulations of the mock-up.

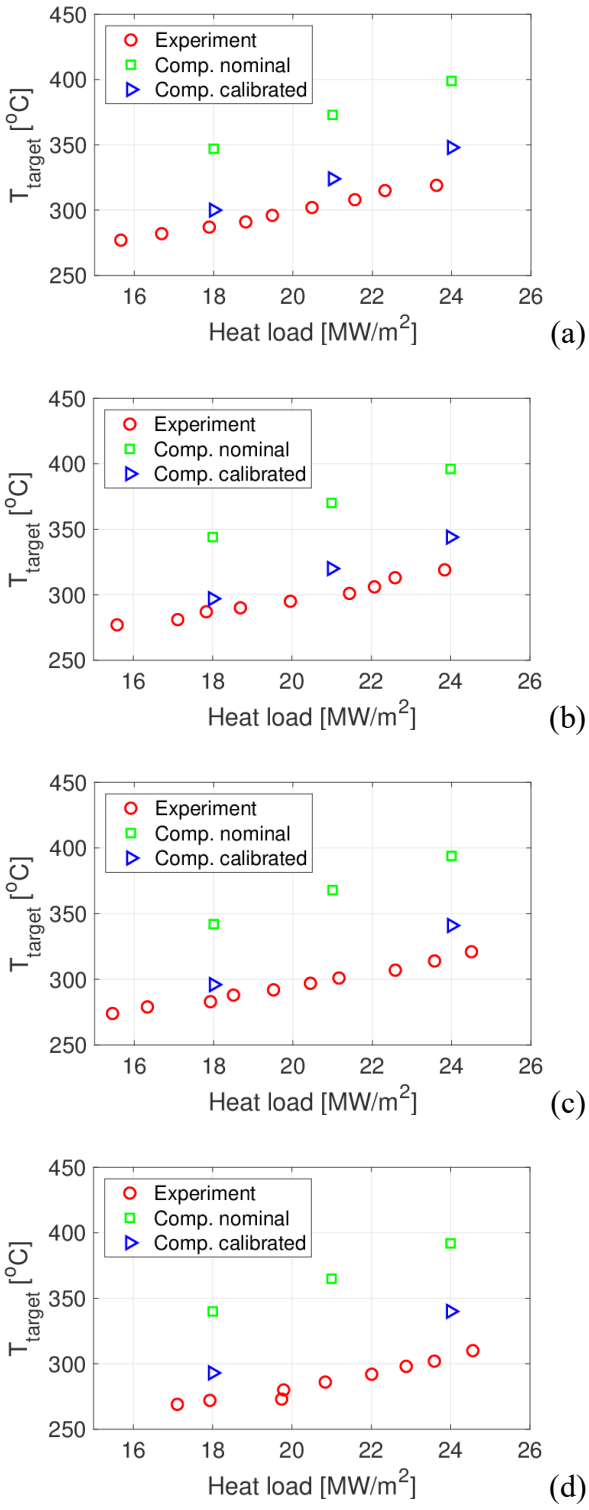

Figure 2.9: Comparison between experimental and calibrated results for the model of the mock-up equipped with RRs with inlet mass flow rates of (a) 50 l/min, (b) 60 l/min, (c) 70 l/min, and (d) 80 l/min.

2.1.2 The Mini-Channels cooling strategy: model and calibration

The design of the gyrotron cavity equipped with Mini-Channels (MCs) is performed in order to suggest an alternative cooling layout to the RRs strategy. The characteristics of the MCs cooling strategy has been explored in [19] comparing its thermal behavior with various possible alternatives as the hypervapotron and the meander flow layouts.

The calibration of the TH models is performed comparing the simulated results with the experiment performed on the planar mock-up[iii] of the cavity equipped with MCs. Due to the lack of information on the coefficient C_{qw} for the water-Glidcop® interface to be used in the boiling model, the value 0.0147 (characteristic of the coupling water and lapped copper [26]) is assumed in the simulations. As the case of the mock-up equipped with RRs, the manufacturing of the mock-up with MCs is performed by Thales Electron Devices and the test campaign is performed by Areva in the FE200 test facility (see Appendix C) in 2016 [31]. The calibration of the model is performed on the thermal contact resistance between the different parts of the mock-up [33].

The mock-up of the cavity equipped with Mini-Channels

The cross section along the longitudinal symmetry plane of the mock-up equipped with MCs is shown in Figure 2.10. The upper region of the structure is transparent in order to see more clearly the internal configuration. Inside the mock-up, the coolant is divided between the MCs and the square-shaped by-pass channels. The first are located in the lower region of the structure in proximity of the heated region and the last are located in the upper region of the structure. The aim of the by-pass channels is to reduce the pressure drop suffered by the coolant between the inlet and the outlet section of the mock-up, which is limited by the working conditions of the test facility.

[iii] The external structure of the mock-up equipped with MCs tested in 2016 is the same as the mock-up equipped with RRs tested in 2015 in the same facility.

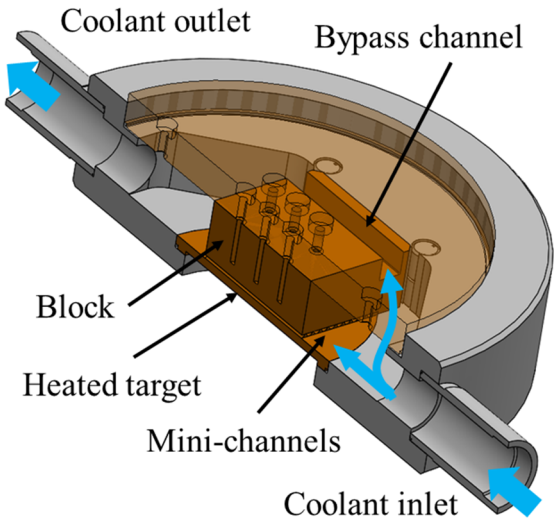

Figure 2.10: Cross section on the symmetry plane of the mock-up equipped with MCs tested in the test facility FE200.

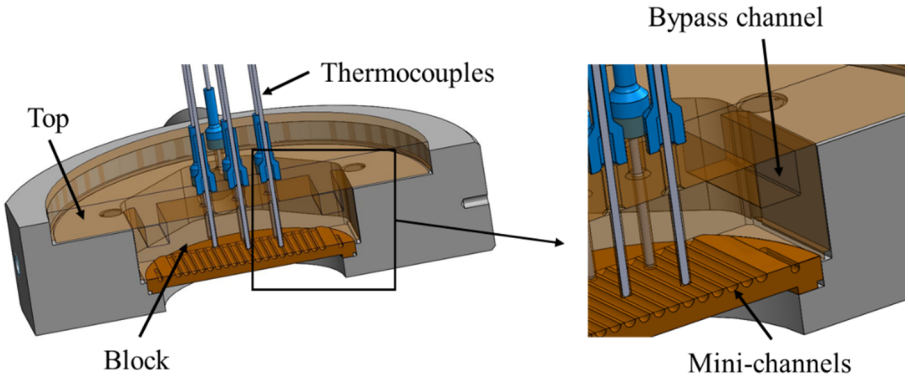

Figure 2.11: Cross section on a plane orthogonal to the MCs of the mock-up equipped with MCs.

Figure 2.11 shows the cross section of the mock-up along a plane orthogonal to the MCs length to highlight the position of the semi-circular channels and the by-pass. The MCs drilled directly on the target region of the mock-up and they are characterized by the curved edge closer to the heated surface. The by-pass channel is obtained on the upper part of the copper hexahedral block that is located above the target region. In total, 19 equally spaced semi-circular channels with diameter of 1.5 mm and length ~33 mm are present in the mock-up, positioned ~2 mm apart from the heated surface of the target. The minimum distance between two consecutive MCs is 0.5 mm. The two by-pass channels are located in symmetric position

with respect to the longitudinal symmetry plane and are in contact with the upper region of the mock-up. The heated surface of the mock-up is a circular disk of ~45 mm of diameter, located in the bottom part of the structure.

The target region of the mock-up is made of Glidcop® whereas the block and the top part region of the structure (colored in transparent brown in Figure 2.11) are both made of copper. The three structures are brazed together along the contact surfaces to prevent coolant leakage.

The simulations performed on the mock-up equipped with MCs take into account the symmetry of the geometry, reducing the computational model to ½ and imposing symmetry conditions on the symmetry plane. The thermocouples shown in Figure 2.11 are removed in the simulations.

Comparison of the experimental and simulation results with the calibration of the thermal-hydraulic model

The pure hydraulic results of the test campaign performed on the mock-up equipped with MCs are shown in Figure 2.12. Following the same procedure adopted for the mock-up equipped with RRs, the hydraulic characterization of the component is obtained when the target is not subject to any thermal loads. The fit curve (see red line in Figure 2.12) well reproduces the experimental results with a R^2 value of 0.999.

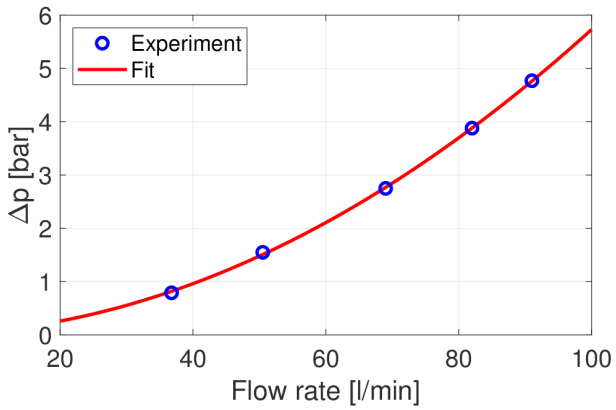

Figure 2.12: Experimental results of the pressure drop in the cavity mock-up equipped with MCs (blue circles) and fit curve (red line).

The temperature of the mock-up target region (see Figure 2.13) are measured during the test campaign using a pyrometer previously calibrated by Areva in the temperature range 300 °C – 450 °C [31].

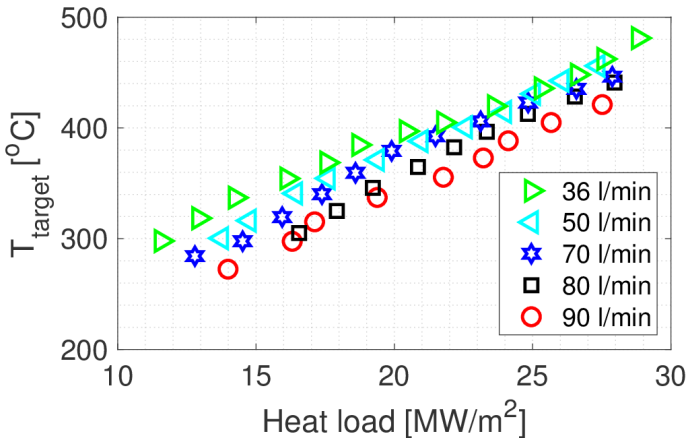

Figure 2.13: Measured temperature on the target surface of the mock-up equipped with MCs at different values of the incident heat flux, for different values of the mass flow rate.

As expected, the trend of the signals shows an increasing temperature with the heat load for a given mass flow rate, and an increasing temperature for the same heat load when the mass flow rate decreases. In the low mass flow rate conditions (i.e. 36 l/min, 50 l/min and 70 l/min), the temperature behavior suffer of a non negligible reduction in the region of the high heat flux, if compared to the behavior observed at lower heat load. This can be explained by the presence of boiling phenomena in the region of the MCs, which increase the heat exchanged with coolant. The same behavior is not clearly visible in the 90 l/min and in the 80 l/min due to the higher mass flow rate inside the channels that may reduce or prevent the presence of boiling.

The experimental results measured by the thermocouples (see Appendix C), that properly work during the test campaign, are shown in Figure 2.15. The sketch of the position of the thermocouples on the mock-up is shown in Figure 2.14 (see Appendix C for more details). The temperatures values show the expected trend: the measured temperature increases with the heat fluxes, and higher inlet mass flow rates are associated with lower measured temperatures for all the thermocouples.

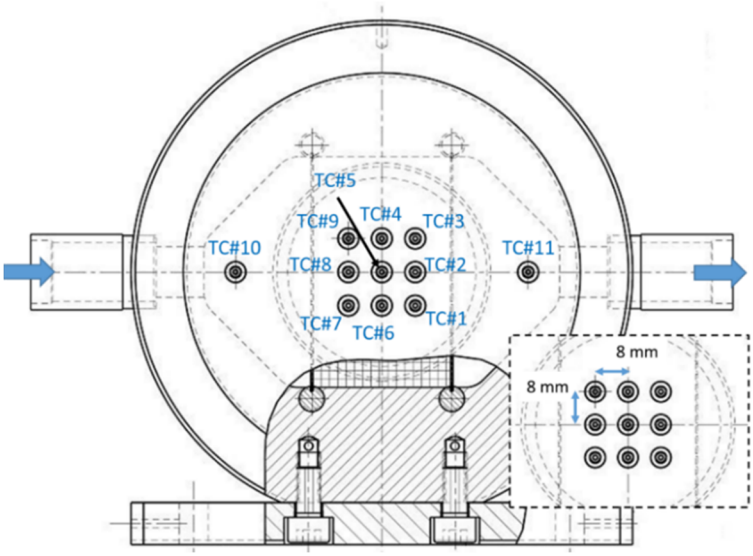

Figure 2.14: Position of the thermocouples in the mock-up (the thermocouples are numbered from #1 to #11). The inset shows the zoom of the region where the 9 thermocouples are positioned, together with their relative distance. The main flow direction in the mock-up is also shown with the light blue arrows.

The simulation process on the mock-up equipped with MCs is performed applying the lower and the higher mass flow rates tested (i.e. 36 l/min and 90 l/min, respectively) in order to validate the two extremes working conditions tested and the mass flow rate of 70 l/min that is relevant for the gyrotron cavity in nominal working conditions (see Appendix D).

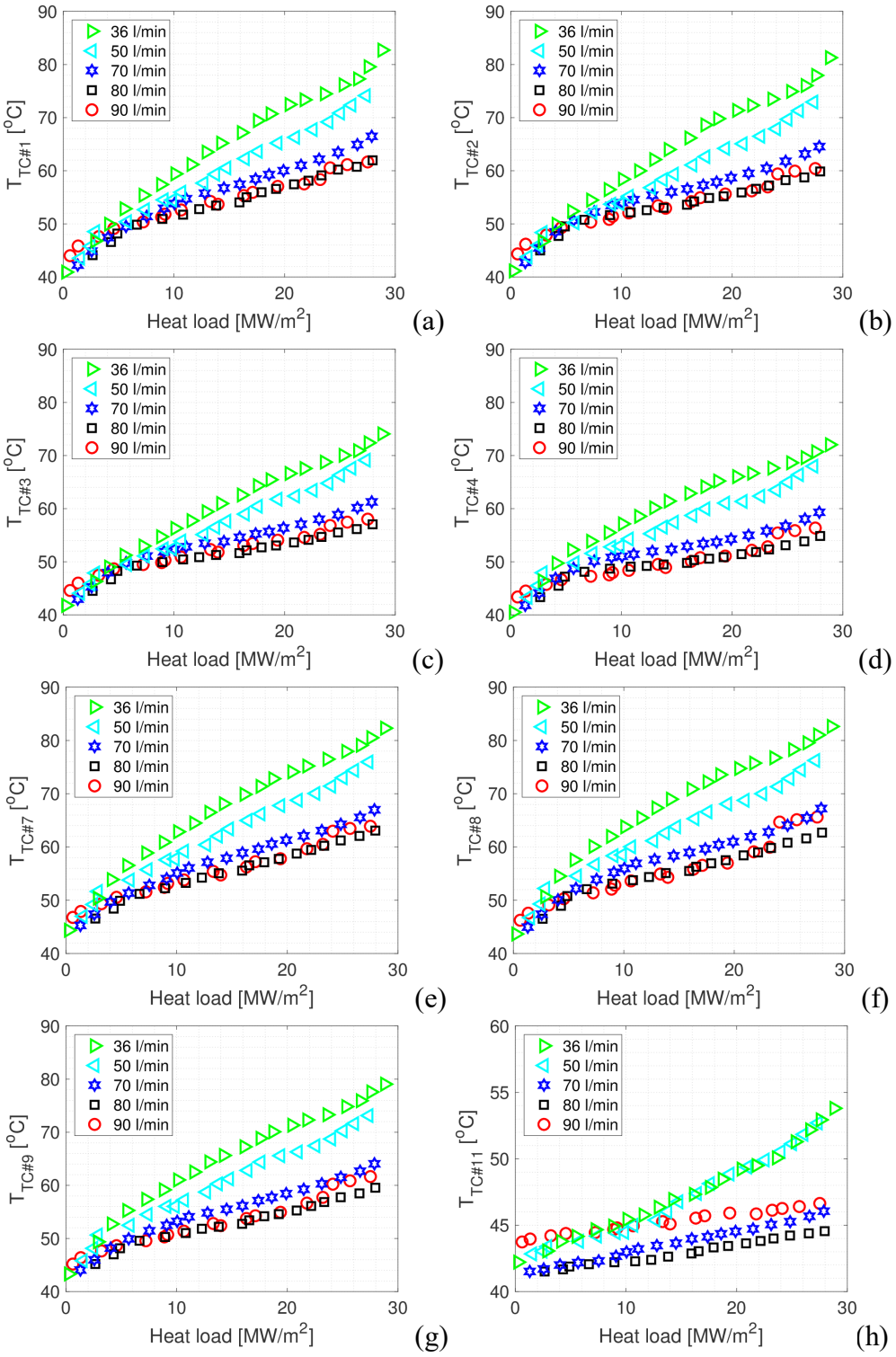

Figure 2.15: Experimental measurements of the working thermocouples in the mock-up equipped with MCs.

The results of the pressure drop curves computed with the analytical model and with the CFD simulations are compared with the results of the test campaign in Figure 2.16. The comparison between the three sets of results shows a very good agreement with a maximum error below 10%. A set of hydraulic simulation using the Realizable k-ε turbulence model [34], gives very similar results if compared with the k-ω model used in the CFD simulations (maximum relative error below 6%), see Figure 2.17.

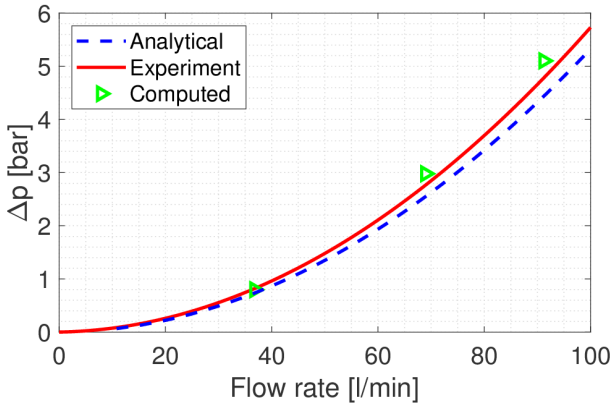

Figure 2.16: Pressure drop across the mock-up, for the different mass flow rates as resulting from the experiments and the simulations (green triangles). The quadratic fit of the experimental data (red solid line), as well as the hydraulic characteristic computed by the analytical simplified model (blue dashed line) are reported.

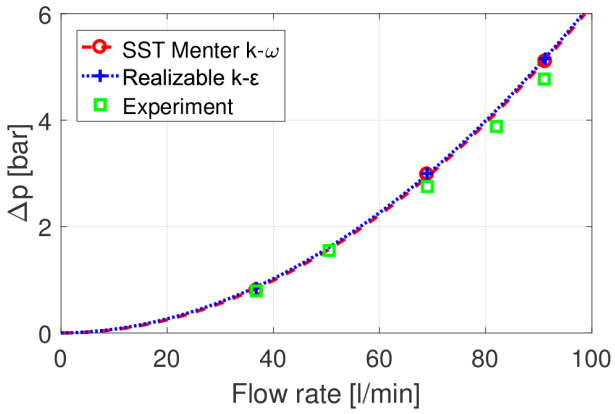

Figure 2.17: Computed pressure drop curves using SST Menter k-ω turbulence model (dashed red line with circles) and Realizable k-ε turbulence model (dotted blue line with crosses).

The relevant results from the pure hydraulic simulations are shown in Table 2.1, which describes the average mass flow rate and the average Reynolds number computed inside the MCs. The Reynolds number is evaluated considering an equal mass flow rate distribution in the channels. As described by the analytical model, the CFD simulations confirm that the representativeness of the gyrotron cavity with nominal mass flow rate (Reynolds number = 1.8×10^4 [35]) is obtained in the mock-up with an inlet mass flow rate of 70 l/min. In addition, the CFD results confirm also the mass flow repartition between the MCs and the by-pass channels (see Appendix D).

Table 2.1: Total mock-up inlet mass flow rate, computed mass flow rate in MCs and average Re in the MCs.

Inlet mass flow rate	Mass flow rate in the MCs	Re inside the MCs
0.63 kg/s (36 l/min)	0.11 kg/s (17.5 %)	0.9×10^4
1.14 kg/s (70 l/min)	0.21 kg/s (18.4 %)	1.7×10^4
1.50 kg/s (90 l/min)	0.28 kg/s (18.6 %)	2.3×10^4

The turbulence models and the simulation setup used for the evaluation of the hydraulic behavior of the coolant in the MCs geometry show very good results when compared to the experimental measurements. This gives a high confidence about the pressure drop evaluation for the simulation of the full-size cavity.

The comparison with the TH simulations of the temperature computed on the heated surface of the mock-up is shown in Figure 2.18 for the three mass flow rates simulated (i.e. 36 l/min, 70 l/min, and 90 l/min), when a heat load between 12 MW/m^2 and 27 MW/m^2 is applied. During the 2016 test campaign, the heat load has a square footprint of 28 mm of side, and it is deposited in the center of the circular target surface of the mock-up.

Two sets of results are shown in Figure 2.18 before and after the calibration process of the contact resistance (R_c) between the target region and the block positioned above the channels. The pyrometer temperature measurements are systematically underestimated by the un-calibrated model (R_c = 0 m^2 K/W) up to a temperature difference of ~50 K (error ~20%). The agreement between simulations and

experiments improves sensibly when a finite value of the contact resistance is accounted for. After the calibration, the best results are obtained with $R_c = 10^{-5}$ m^2 K/W, which lies inside the range of validity for the copper-copper thermal coupling [26], leading to an error < 15% [33].

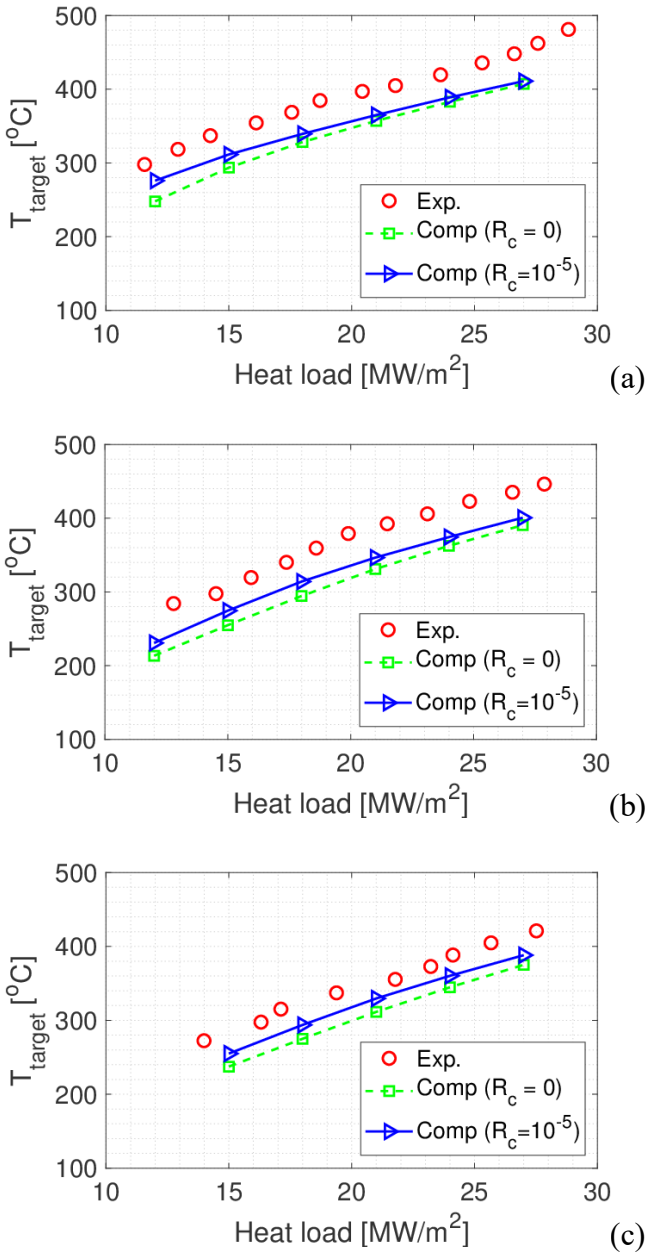

Figure 2.18: Comparison between the experimental (circles) and computed temperature on the heated surface with two values of R_c (dashed with squares and solid with circles), for a mass flow rate of: (a) 36 l/min, (b) 70 l/min and (c) 90 l/min.

In the region of the high heat fluxes, the positive effect of the water boiling is evident in the reduction of the target temperature curves slope due to the improvement on the heat transfer coefficient. This effect is more evident for lower mass flow rates.

A set of nine thermocouples (TC) is installed in contact with the block region of the mock-up. Figure 2.19 shows the temperature values measured by the TC #1 (see Appendix C) and computed in the TH simulations before (Figure 2.19a) and after (Figure 2.19b) the calibration of R_c. The value of the thermal resistance R_c is calibrated in the case with mass flow rate of 36 l/min and heat load of 24 MW/m^2. Then the value of R_c is frozen for the simulations of the other two cases. While the temperatures computed with $R_c = 0$ m^2 K/W largely disagree with the measured values, the effect of the calibration is quite remarkable, reducing the error with respect to the experimental results in the complete set of simulations.

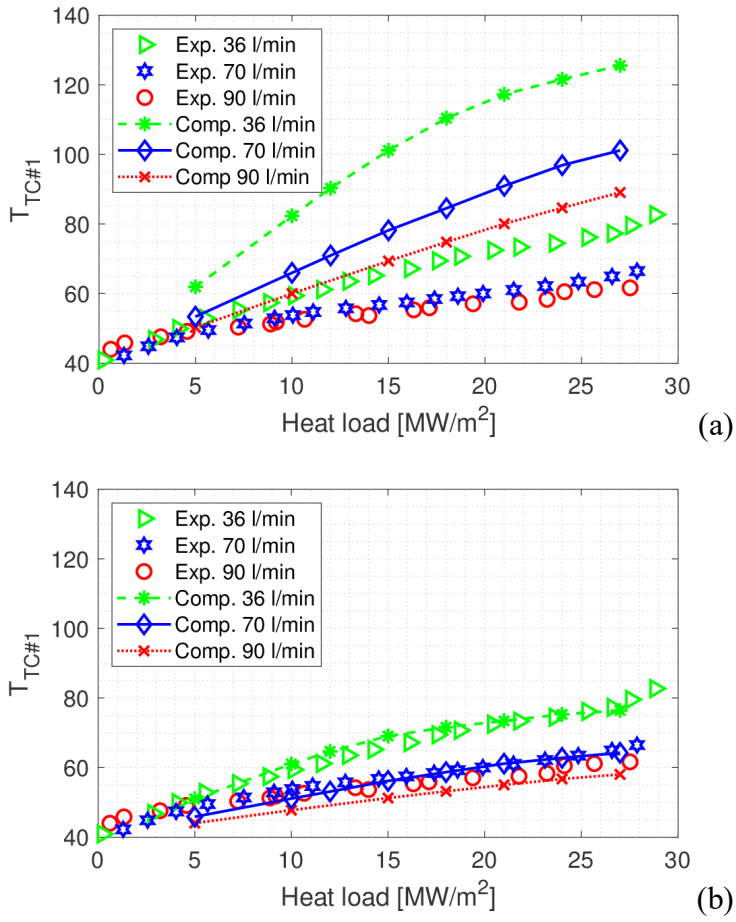

Figure 2.19: Comparison between experimental and computed temperatures at the position of the TC #1 with (a) $R_c = 0$ m^2 W/K and (b) $R_c = 10^{-5}$ m^{2}W/K.

The discrepancy between the simulation and the experiment in the different thermocouples is shown in Figure 2.20. The comparison with the simulation results is presented in terms of temperature difference (Figure 2.20a) and of relative error with respect to the initial temperature considered (i.e. 40 °C), for the thermocouples working properly during the campaign (Figure 2.20b). Taking into account the uncertainties related to the experimental campaign [31], the comparison between the experimental and the computed results after calibration can be considered satisfactory: the maximum temperature difference is <5 °C and the maximum relative error is lower than 22 %.

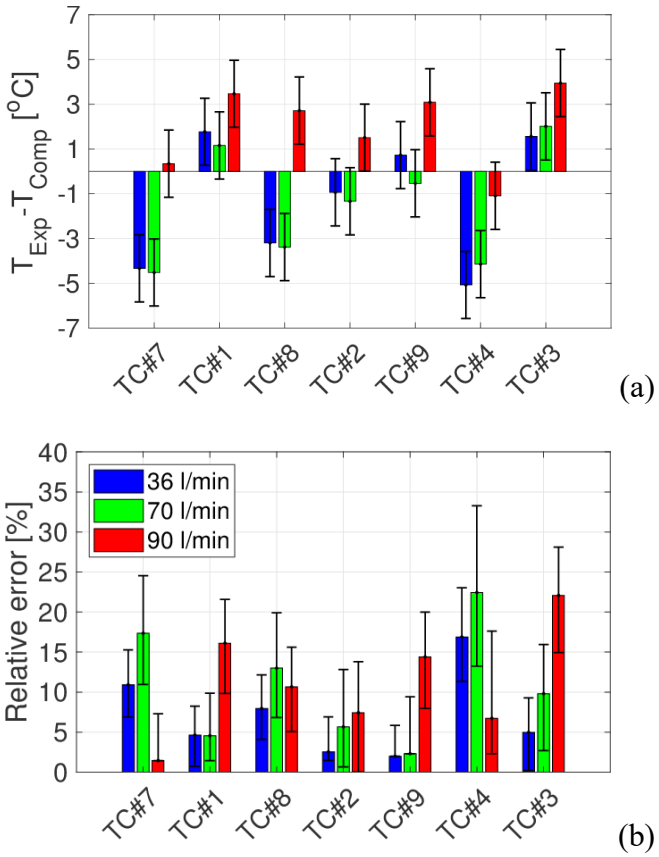

Figure 2.20: Comparison between experimental and computed results in terms of (a) absolute and (b) relative error for working thermocouples, at the various tested mass flow rates and heat load of 27 MW/m^2. Error bars are computed considering thermocouples accuracy of ± 1.5 °C.

The calibration performed on the mock-up equipped with MCs shows that the effect of the contact resistance on the simulation results is extremely important in this type of cooling structure. To characterize at best the contact resistance, precise

information, about the constitutive materials of the components adopted and the manufacturing process used to assembly the cavity, are needed.

2.2 The Thermo-Mechanical model

The simulation of the TM behaviour of the gyrotron cavity is done by PoliTo using the commercial software STAR-CCM+®. In order to reduce the computational cost, these simulations are performed only on the resonator structure of the cavity (see Figure 2.21) and on the coaxial insert, if present. In the case of the MCs simulation, the region above the channels is also simulated since its impact on the thermal deformation of the heated surface is not negligible.

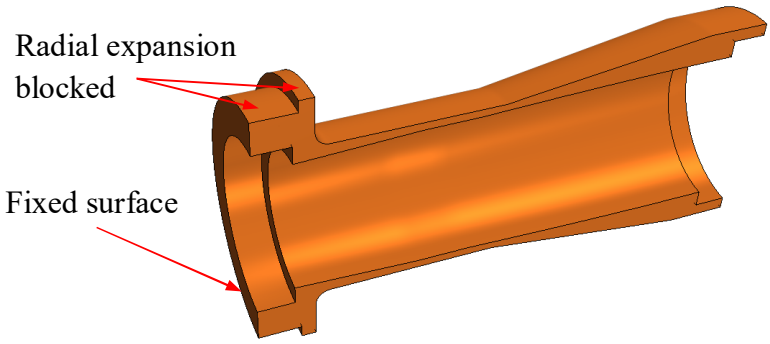

Figure 2.21: Computational domain used for the TM simulations of the cavity equipped with RRs and mechanical boundary conditions.

The mechanical boundary conditions defined in the TM simulation are set to reproduce the constraints present in the gyrotron structure. In particular, for the 1 MW gyrotron for ITER, the bottom surface of the resonator is fixed to the external structure of the gyrotron [35], while for the coaxial cavity for the 2 MW gyrotron for DEMO, the upper surface of the resonator is fixed (see Figure 2.22) on the launcher structure [36].

For both configuration of the gyrotron cavity, the application of the *"normal constraint"* condition defined in STAR-CCM+® impedes the expansion of the lateral surface of the resonator. This is done to simulate the effects of the contact with the external structure of the cavity, which is indeed removed in the simulation (see Figure 2.22). The other surfaces of the resonator are free to move.

In the coaxial cavity, a fixed mechanical constraint on the bottom surface of the coaxial insert structure is applied [36]. The mechanical coupling between the insert

and the resonator is performed applying an axial displacement on the lower surface of the insert of the same magnitude of the axial shift on the lower surface of the resonator (see blue arrows in Figure 2.22). This assumption is justified since the longitudinal expansion of the resonator induces the movement of the coaxial insert, due to the mechanical connection between the two components in the region not considered in the simulation (see Figure 1.13).

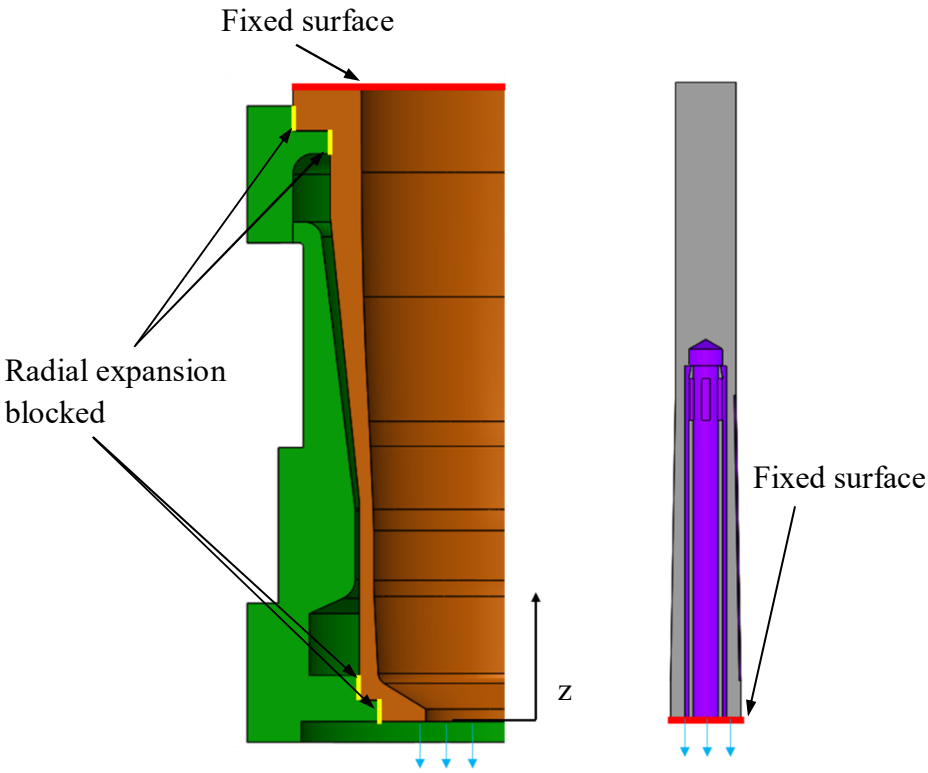

Figure 2.22: Mechanical constraints defined for the gyrotron coaxial cavity for DEMO.

A temperature of 27 °C is used as reference for the definition of the thermal unstressed condition of the solid structures of the resonator and of the insert, based on the ambient conditions which characterize the construction phase of the components [36]. The deformations induced by the thermal equilibrium between the solid structure and the coolant (40 °C) is also taken into account to evaluate the initial condition of the cavity. For the same reason, the axial shift of the coaxial insert is evaluated by (14) considering also the thermal deformation of the lower part of the insert, which is not simulated here.

$$\Delta L_{insert} = \alpha_{Cu} L_0 \Delta T_{t=0} \tag{14}$$

in which ΔL_{insert} is the axial shift of the lower base of the computed part of the insert due to the deformation of the region below characterized by an initial length of L_0, α_{Cu} is the copper linear expansion coefficient and $\Delta T_{t=0}$ is the temperature difference with respect to the unstressed condition at the beginning of the transient.

The mechanical properties of the copper [29] and of the Glidcop® [30] are functions of the temperature of the solid structure (see Appendix A).

2.3 The Electro-Dynamic model

The resonating interaction of the electrons beam with the internal surface of the resonator is simulated by KIT with the code EURIDICE® [21]. The deformed profiles of the inner surface of the resonator and of the outer surface of the insert (if present), computed in the TM simulation, are used in the code EURIDICE®. The outcome of the ED simulation is the new profile of the heat loads which has to be applied on the resonating surfaces of the cavity in the next step of the MUCCA, i.e. the TH simulation. The temperature profiles from the previous TH simulation are also taken into account in the ED simulation to evaluate the electrical properties of the surface involved.

Since EURIDICE® approximates the resonating surfaces of the cavity with their 2D profiles, the temperature and the deformed profiles evaluated on the heated surface of the cavity need to be averaged along the azimuthal coordinate before being processed in the ED simulations.

The evaluation of the wall losses due to the interaction of the electron with the resonating surface of the cavity is given by (15) [11].

$$\frac{dP_{loss}}{dA} = \left(\frac{1}{2\sigma\delta}\right) |H_{tan}|^2 \tag{15}$$

in which $\frac{dP_{loss}}{dA}$ is the power deposited on the resonating surface per unit area, δ is the skin depth defined by (16), σ is the electrical conductivity of the resonating structure, H_{tan} is the tangential component of the magnetic field on the resonating surface.

$$\delta = \left(\frac{\lambda}{\pi \mu_0 c \sigma}\right)^{\frac{1}{2}} \tag{16}$$

in which λ is the RF wavelength and μ_0 is the permittivity of the medium.

The heat load computed by the code EURIDICE® is shown in Figure 2.23a and Figure 2.23b, in the case of the resonator and of the coaxial insert, respectively. The presence of the proper electromagnetic field in the mid-section region of the resonator produce the resonating interaction of the electrons that leads to a very high heat flux peaked in this region.

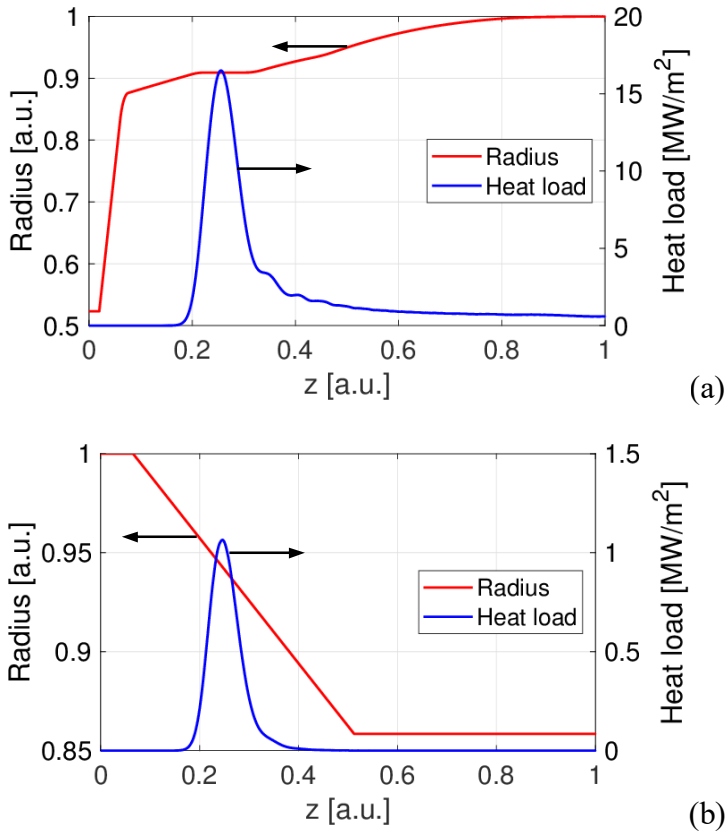

Figure 2.23: Heat loads (blue lines) computed with the EURIDICE® code for (a) the resonator and (b) the coaxial insert of the cavity.

Chapter 3

Analysis of the 1 MW ITER gyrotron cavity equipped with Raschig Rings[i]

In this chapter, the MUCCA tool is applied on the study of the 170 GHz, 1MW gyrotron cavity[ii] designed for the ITER EC system. The resonator of the cavity adopts the RRs cooling strategy already used in the mock-up. The approach for the simulations and the models used in the analysis of this kind of cavity reflect the strategy adopted for the simulations of the mock-up, on which a first rough calibration of the thermal conductivity of the porous region has been performed based on the results of the experimental campaign performed in 2015 (see paragraph 2.1.1).

3.1 The cavity of the gyrotron equipped with Raschig Rings

The model used in the MUCCA tool of the 170 GHz, 1 MW gyrotron cavity applied in the ITER EC system is shown in Figure 3.1. The heat transfer promoter is a porous region made by RRs (in grey) located in the annular region between the resonator and the external stainless steel structure (not shown in Figure 3.1). The porous

[i] The material presented in this chapter is mainly based on [53].

[ii] The dimensions of the cavity described in this chapter are under confidentiality restriction and they are reported scaled with respect to the total length or the maximum radius of the component.

region is installed in the region of the cavity with the peak heat load applied on the resonator [36]. As performed in the simulations of the planar mock-up, the RRs region is modelled separately in a proper simulation performed in STAR-CCM+® (see Appendix E).

To limit the computational domain taking advantage on the geometry symmetry, the model used in the simulation is reduced longitudinally up to the end of the resonator (see Figure 3.1). The region of the outlet pipe of the cavity and the launcher structure are removed and an annular coolant outlet is defined.

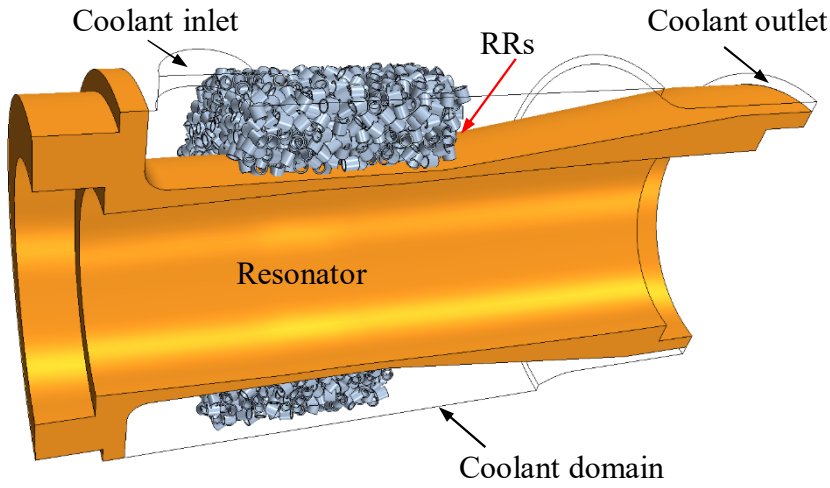

Figure 3.1: Model of the cavity equipped with RRs used in the simulations of the 170 GHZ, 1MW gyrotron for ITER. The surface of the coolant domain, which is conceivable by the lines that define its perimeter, is removed in order to figure out the position of the RRs region.

The radial profile of the heated surface of the cavity resonator and the heat loads used in the initial stage of the iterative process of the MUCCA tool are shown in Figure 3.2. On the same figure, the axial location of the RRs region is showed with the magenta band. Four working conditions of the cavity at different gyrotron output powers, are used for the validation of the MUCCA tool, identified by 300, 500, 700, and 800 which are related to the RF power produced in the gyrotron during operation, expressed in kW. The heat loads are azimuthally symmetric and they are applied on the internal surface of the cavity resonator. The flat region of the resonator, where the heat load reaches its maximum value, is called “mid-section” ($0.3 < z < 0.4$ in Figure 3.2): this is the most critical part of the resonator where RF waves are produced by the interaction between the electrons and the magnetic field. The part of the resonator following the mid-section ($z > 0.4$) is called “up-taper”

and it plays an important role on the evaluation of the power deposited inside the cavity due to the relevant axial dimension in comparison with the mid-section.

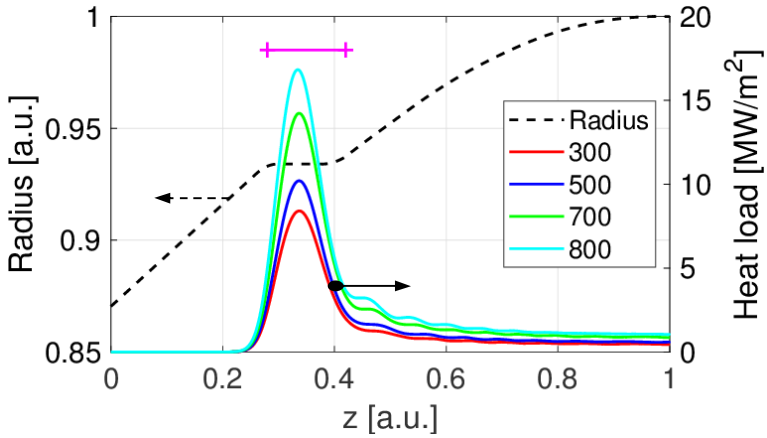

Figure 3.2: Radial profile (black dashed line) of the heated surface of the cavity equipped with RRs and the profile of the initial heat loads (solid lines) used in the MUCCA tool. The magenta band indicates the extension of the RRs region along the profile of the cavity.

The simulations are performed applying the nominal working condition of the cavity cooling circuit, characterized by a constant inlet mass flow rate of 45 l/min, at the constant temperature of 27 °C and pressure of 6 bar [36]. The mechanical simulations are performed fixing the outlet region of the resonator (z = 1) and keeping free to move the lower base of the cavity [36].

3.2 Validation of the MUCCA tool against experimental results

The validation of the MUCCA tool is done on the full-size cavity equipped with RRs using the setup obtained after the calibration performed on the mock-up (k_{RR} = 2000 W/m K). The results computed on the cavity at the end of the iterative process of the MUCCA tool are compared with the outcomes of the experimental campaign performed independently by KIT in 2016 on the ITER gyrotron equipped with RRs. The validation is performed considering different working conditions of the gyrotron and monitoring the variation of the frequency in the cavity, which is directly related to the thermal deformation of the resonating surface.

The heat load profiles computed at the end of the simulation (solid lines) is compared in Figure 3.3 with the initial heat load (dotted lines) obtained in EURIDICE® considering the initial undeformed cavity condition. The heat loads peak computed during the final step of the MUCCA tool are lower if compared to

the initial ones and the axial location of the peak is shifted toward the outlet region of the cavity due to the deformed shape of the mid-section region (see below).

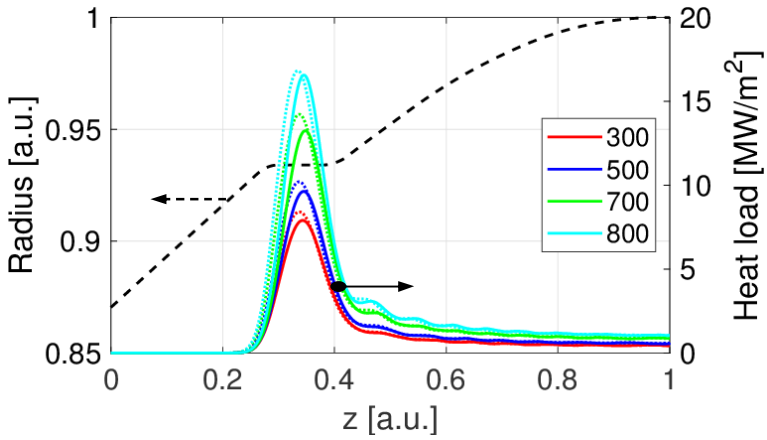

Figure 3.3: Comparison of the computed heat loads at the end of the iterative process of the MUCCA tool (solid lines) and its initial value (dotted lines).

The temperature profiles of the resonator computed at the end of the iterations of the MUCCA tool are shown in Figure 3.4. In this set of simulations, the steady state TH approach is used, since the relevant information of the cavity are associated to the steady state working condition of the component.

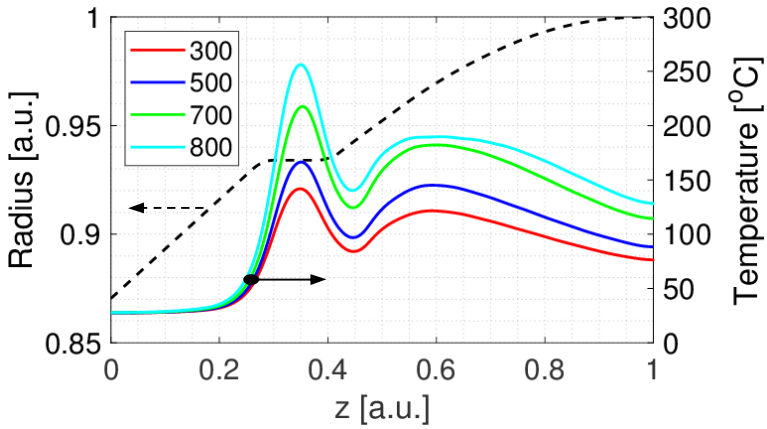

Figure 3.4: Computed temperature profiles on the heated surface of the resonator at the end of the iterative process of the MUCCA tool.

As expected from the applied heat load profile, the most critical region, where the temperature profile is peaked, is located in the mid-section of the resonator. At the beginning of the up-taper region, approximatively at $z = 0.6$, the temperature profiles is characterized by non-negligible a local peak which affects considerably

the thermal and mechanical behavior of the structure. The main cause of this anomalous behavior is due to the cooling inefficiency in this region. In fact, the very low coolant velocity observed here (see Figure 3.5) is caused by the large frontal area of the cooling circuit in this region and by the absence of the RRs porous medium. In the case of the 800 working condition, a temperature plateau is observed around z = 0.6 caused by the presence of boiling, which improves locally the heat transfer coefficient. Boiling is also present in the 700 working condition even though the effects on the temperature profile is not clearly visible since the minor intensity of the phenomena. Vice versa, in the 500 and 300 conditions, boiling is not observed because the heat load in this part of the cavity is slightly lower with respect to the other two situations (see Figure 3.2). Moving toward the outlet region of the resonator, the cooling circuit is characterized by a consistent reduction of the flow cross section, which contributes to improve sensibly the coolant speed and, consequently, to enhance the heat transfer coefficient in this region of the cavity.

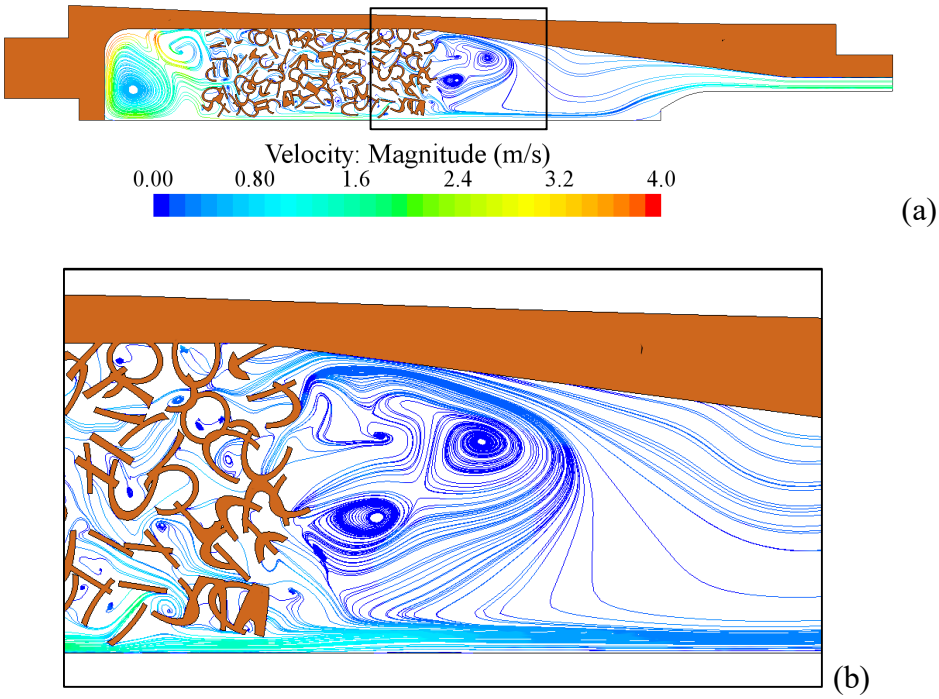

Figure 3.5: (a) Computed streamlines in a longitudinal cross section of the cavity equipped with RRs and (b) zoom of the streamlines in the outlet region of the RRs region.

The complexity of the fluid path inside the RRs region can be observed in the streamlines computed in a longitudinal cross section of the fluid, which are shown

in Figure 3.5. The pressure drop between the inlet and the outlet section of the simulated domain is ~ 0.17 bar, thanks to the low hydraulic resistance of the RRs region and the absence of abrupt reduction of flow area in the cooling circuit of the cavity.

The temperature map computed on the solid structure of the cavity is shown in Figure 3.6, focused on the heated surface of the resonator and on the symmetry plane. The temperature field on the RRs region shows that the part exchanging heat with the coolant in an efficient way is localized nearby the resonator. In the external region, the RRs temperature is almost unperturbed with respect to the initial temperature of the structure (27 °C) without a relevant impact on the cavity cooling.

Focusing on the temperature map in the mid-section region of the heated surface, some local peaks are present due to the effects of the arrangement of the RRs in contact with the resonator. The position of the RRs, which are randomly injected during the construction of the model, may produce a flow stagnation point with a consequent local increment of the solid structure temperature, clearly visible also on the heated surface.

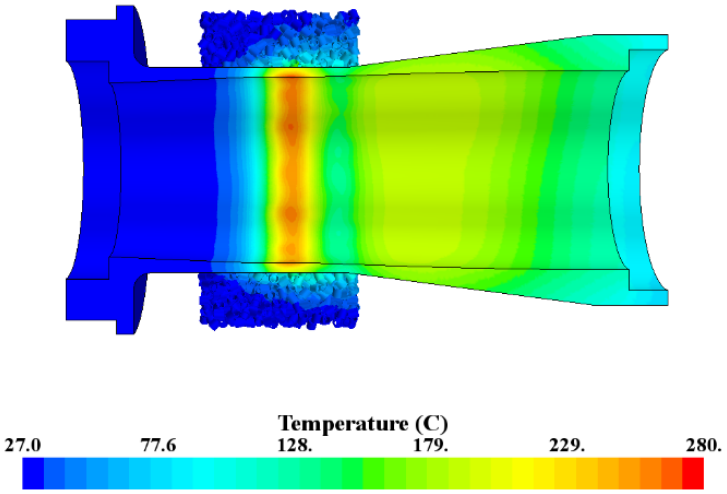

Figure 3.6: Computed temperature map on the solid structure (resonator and RRs region) of the cavity equipped with RRs at the final iteration of the MUCCA tool applied on the 800 kW working condition.

The deformed profiles of the resonating surface of the cavity equipped with RRs are shown in Figure 3.7. The deformed radius in the mid-section region (see the inset of Figure 3.7) appears in a bell-shaped profile with radial increment toward the up-taper region, due to the temperature field obtained in the resonator and the

mechanical constraints applied on the cavity causing the heat load shifting toward the outlet section of the cavity computed at the end of the iteration of the MUCCA tool (see Figure 3.3). The RRs region in the TM simulation is not included in the computational domain due to the impossibility to obtain a simulation with this porous medium. The effect of the RRs region can be assumed negligible in the modification of the thermal expansion behavior of the inner surface of the resonating region of the cavity thanks to the experimental tests performed in [37].

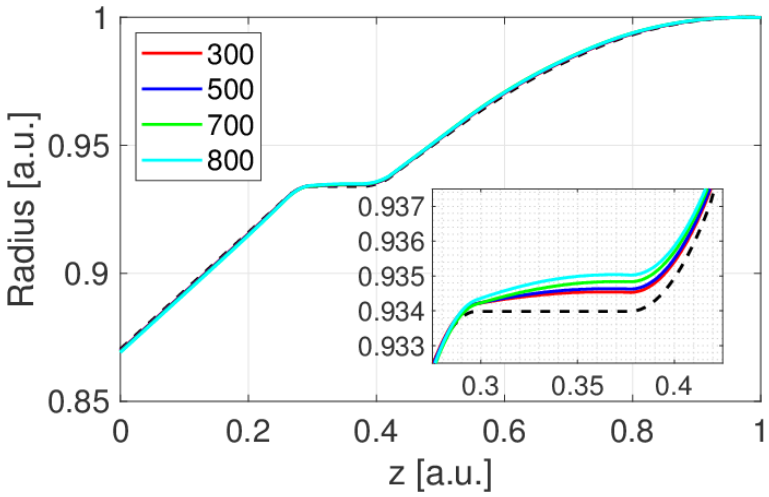

Figure 3.7: Computed deformed radial profiles of the heated surface of the resonator at the end of the iterative process of the MUCCA tool.

In order to improve the overall thermal performances of the RRs cooling strategy, the reduction of the external radial thickness of the cavity cooling region is suggested, so that the coolant flow area is reduced [38]. Some positive cooling effects are observed thanks to the increase of the water flow speed in the coolant domain, where the RRs are located, and on the up-taper regions of the cavity with a non-negligible peak temperature reduction.

The comparison between the frequency shift evaluated at the final iteration of the MUCCA tool by EURIDICE® and the experimental results of the test campaign performed by KIT is shown in Figure 3.9 as a function of the power losses in the cavity. The ohmic loss at the cavity is defined as the integral of the heat flux on the resonating profile of the cavity, while the frequency shift is computed by EURIDICE® taking into account the deformed profile of the cavity. The output wave frequency shifts are evaluated during the experiments comparing the frequency at the end and at the beginning of the gyrotron pulse, both measured by an

oscilloscope (see as example the Figure 3.8, which is not referred to the test performed by KIT).

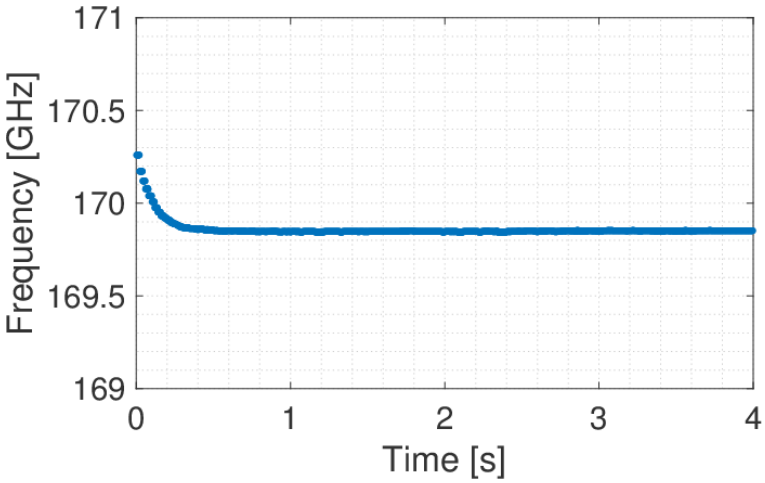

Figure 3.8: Frequency shift during gyrotron operations measured during experiments [39].

The results obtained with the MUCCA tool are in acceptable agreement with the linear fit of the results obtained during the experimental campaign performed by KIT [40]. The results of the validation process are positive because the slope of the frequency down-shift, dependent on the ohmic losses in the cavity, is well reproduced by the simulations. The relative errors computed on the slope and on the intercept of the two sets of results are ~ 4.5 % and below 1 %, respectively.

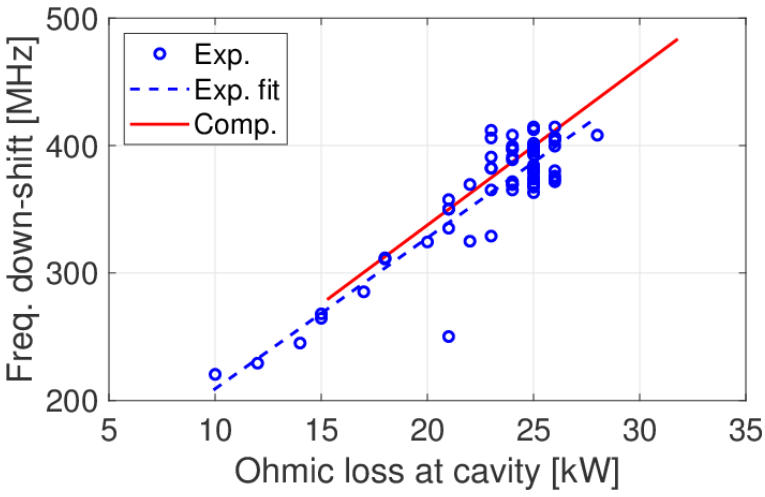

Figure 3.9: Frequency shift as a function of the ohmic loss at the cavity: measured and linear fit curve of the KIT experimental results (blue circles and dashed blue line) and results of the MUCCA tool on the 170 GHz, 1 MW ITER gyrotron cavity.

3.3 Generalization of the simulation results for the 170 GHz, 1 MW ITER cavity equipped with Raschig Rings

Aiming at improving the quality of the fit of the experimental frequency down-shift, a procedure is adopted to approximate the gyrotron behavior as a function of the deformation, based on the technical experience developed at KIT on the gyrotrons field [41]. Based on the 2016 experimental campaign on the 170 GHz, 1 MW ITER gyrotron, the frequency shift can be linearly related to the ohmic losses evaluated in the cavity region (see Figure 3.9):

$$\Delta f \cong A\, P_{loss} + B \tag{17}$$

in which $\Delta f = f - f_0$ is the frequency shift, and P_{loss} is the ohmic power dissipated on the cavity wall.

The frequency of the waves produced inside the gyrotron, at a given operating point, is proportional to the radius evaluated at the center of the mid-section of the cavity (R_{cav}):

$$f \cong \frac{C}{R_{cav}} \tag{18}$$

Consequently, the frequency shift can be expressed as a function of the radial thermal deformation of the cavity computed at the center of the mid-section of the resonator. In the equation (19), the subscript "0" indicates the initial nominal undeformed condition of the cavity.

$$\Delta f = -\left(\frac{f_0}{R_{cav,0}}\right)\Delta R \tag{19}$$

Finally, the power loss in the cavity region can be expressed proportionally to the value of the heat load applied on the center of the mid-section of the heated surface of the resonator (ρ).

$$P_{loss} \cong D\, \rho \tag{20}$$

From the above correlations, the ratio of the slope of the radial deformation in the center of the mid-section of the cavity depends only on the constant defined in

by A, since the constant D and the group $\left(\frac{R_{cav,0}}{f_0}\right)$ can be considered independent to the operating point of the gyrotron.

$$\frac{d\Delta R}{d\rho} \cong -D \left(\frac{R_{cav,0}}{f_0}\right) A \tag{21}$$

A set of simulations is performed with the four heat loads used in the paragraph 3.2 (corresponding to a different working conditions of the gyrotron) with different values of the thermal conductivity of the RRs region. Figure 3.10 shows the relation between the radial deformations computed at the center of the mid-section resonator and the value of the heat load applied on the same point. The simulations are performed by fixing the thermal conductivity of the RRs region (see legend of Figure 3.10). The dashed lines represent the linear fits of the results computed at the same value of the thermal conductivity.

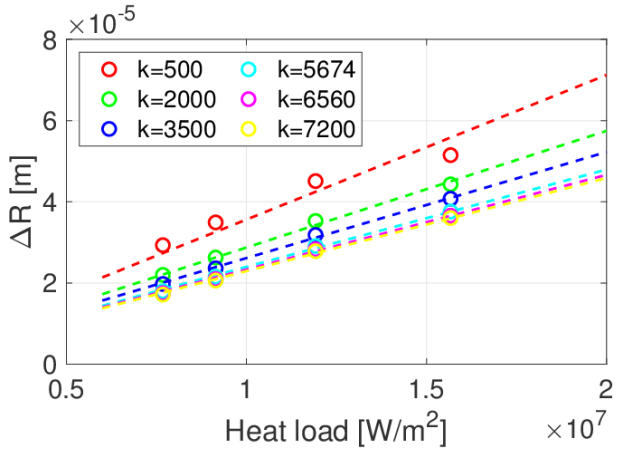

Figure 3.10: Computed radial deformations (circles) and linear fit curves (dashed lines) as a function of the heat loads both evaluated at the center of the mid-section of the resonator equipped with RRs. The parametrization is based on the thermal conductivity of the RRs region expressed by k.

The R^2 value of the fit curves shown in Figure 3.10 is reported in Table 3.1. The curves approximate very well the simulation results, in particular for high values of the RRs thermal conductivity where the R^2 is always higher than 0.995. The error bars shown in Figure 3.11 are computed based on the prediction bounds of the linear fit obtained with the interval of confidence of 80%, following the procedure defined for the statistical inference about the linear regression parameters, which is described in [42]. The reduced number of simulation results does not allow to obtain a lower error bar, even though the coefficient of correlation is acceptable for k_{RR}

greater that 2000 W/m K. Furthermore, the error bar on the lower value of conductivity is also affected by the low R^2 value. Since the preliminary calibration of the RRs thermal properties shows that the value of 2000 W/m K represents the upper bound for the finer calibration of the k_{RR}, no further investigations are performed in the case of 500 W/m K.

Table 3.1: Coefficient of correlation (R^2) of the linear fits for the different value of thermal conductivity simulated.

k_{RR} [W/m K]	R^2
500	0.883
2000	0.994
3500	0.997
5674	0.997
6560	0.997
7200	0.997

The slopes of the linear fit obtained from Figure 3.10 are reported in Figure 3.11 to show the general behavior of the deformation of the cavity, as a function of the thermal conductivity of the RRs, by removing the dependency of the gyrotron working condition.

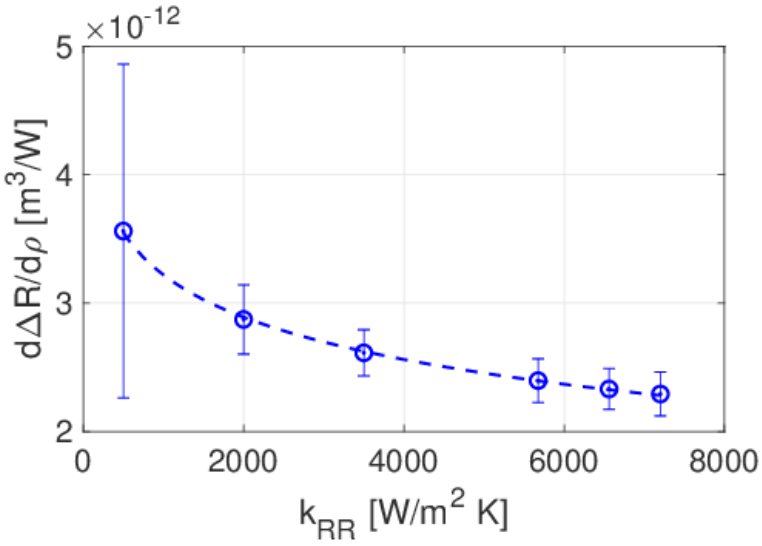

Figure 3.11: Fit curve (dashed line) of the computed value (circles) of the dΔR/dρ as a function of the thermal conductivity of the RRs region.

The fit curve of the dΔR/dρ as a function of the thermal conductivity of the RRs region is expressed by:

$$\frac{d\,\Delta R}{d\,\rho} = -4.77 \cdot 10^{-13} \cdot \ln k_{RR} + 6.50 \cdot 10^{-12} \qquad (22)$$

The fit curve reported in (22) is characterized by R^2 equal to 0.993.

The comparison of the results computed with the MUCCA tool and the outcomes of the experimental campaign (see Figure 3.9) suggests a growth of the value of the k_{RR} to reduce by ~ 4.5 % the slope of the computed frequency-shift curve. The target value of the k_{RR} is evaluated from equation (22), obtaining a thermal conductivity of the RRs region of ~ 2600 W/m K to be used in the TH simulations.

The results with the new value of the thermal conductivity are shown in Figure 3.12. The error bar on the experimental fit is computed by the experimental points shown in Figure 3.9, using the procedure described in [42], with a confidence interval of 80%, while the error bar on the simulation results are evaluated based on the error reported in Figure 3.11 for the related value of the RRs thermal conductivity. Both the validation and the calibration set of results lies inside the error bar built on the experimental results obtained by the statistical inference of the data available from the KIT test campaign. The agreement obtained using the new calibrated value of the thermal conductivity of the RRs region is improved, if compared

to the setting adopted in the validation process providing the consistency of the approach used for the characterization of the cavity. In particular, as far as the fit curve slope is concerned, the relative errors on the slopes and on the intercept of the two set of results are < 2 % and ~ 5 %, respectively.

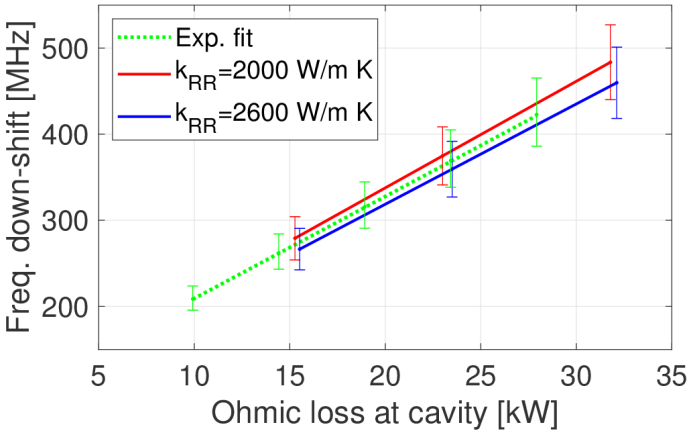

Figure 3.12: Results of the calibration of the thermal conductivity of the RRs region, based on the experimental results on the 1 MW cavity.

3.4 Summary

In this chapter, the results of the experimental campaign performed by KIT in 2016 on the 1 MW European gyrotron prototype for ITER have been used for the validation of the MUCCA tool. The thermal model has been previously calibrated based on the results of the experimental test performed by Areva in 2015 on the planar mock-up of the cavity, which is characterized by the same cooling promoter strategy involving the RRs. The experimental and the computed results have been compared in terms of frequency down-shift of the RF driven by the thermal deformation of the cavity, as a function of the ohmic power deposited on the resonating surface of the cavity. The results of the MUCCA tool are in agreement with the experimental measurements performed during tests. The fit curve of the computed results lies inside the error bar associated to the fit curve obtained from the results of the experimental campaign. The relative error between the simulated and the experimental results are ~5 %.

A finer calibration process has been performed modifying systematically the thermal properties of the RRs region modelled in the MUCCA tool, obtaining a general description of the cavity deformation based on the effective thermal conductivity of the porous medium characterized by the RRs. Based on the general

model obtained, a new set of MUCCA simulations has been performed starting from the same initial condition used in the previous validation simulations. The results achieved with the definition of the effective thermal resistance of the RRs region established “a priory” by the general model of the cavity, reduce the relative error at ~2 % with respect to the experimental results.

Chapter 4

Analysis of the 1 MW ITER gyrotron cavity equipped with Mini-Channels[i]

In this chapter, the MUCCA tool is applied on the design of the cavity equipped with MCs[ii], an alternative to the RRs cooling layout to be used on the 170 GHz, 1 MW gyrotron for the ITER EC system.

In the first paragraph, the results of the TH and the TM simulations are shown on a preliminary simplified geometry of the cavity. Starting from the TH results, a simplified model for the evaluation of the thermal behaviour of the cavity is presented. The simplified model aim at reducing the computational cost of the simulations performed by the MUCCA tool.

In the second section, the TH simulations are applied on a more recent and accurate geometry of the cavity, optimizing the MCs cooling concept. This study is performed in strict collaboration with Thales Electron Devices.

[i] The material presented in this chapter is mainly based on [35].

[ii] The information about the dimension of the resonating surface of the cavity described in this chapter, are under confidentiality restriction and they are normalized with respect to the total length and the maximum radius of the components.

4.1 Simplified thermal model of the cavity equipped with Mini-Channels

The development of the simplified thermal model of the cavity equipped with MCs is aiming at reducing the computational time used for the TH simulations (called in this paragraph "complete" TH model) of the MUCCA tool. The time required[iii] to conclude the simulation of the complete TH model is ~15 hours, which is the most relevant part of the overall time used to perform one iteration of the MUCCA tool (~20 hours in total, excluding the interactions between Polito and KIT).

The simulations performed in this paragraph are developed starting from a simplified version of the CAD model of the cavity equipped with MCs (see Figure 4.1). In this geometry, the axial length of the up-taper region is reduced removing the outlet cooling pipe to take advantage from the symmetry condition of the structure and to reduce the overall computational cost. The cooling strategy adopted includes 64 MCs (in the whole geometry), characterized by semicircular cross section and the diameter of 1.5 mm [35]. Following the rationale used in the cavity mock-up tested by Areva, the curved surfaces of the channels are faced inward, toward the heated surface of the resonator. The minimum distance between the heated surface of the cavity and the channels is 2 mm, defined by manufacturing constraints. The coolant conditions applied in the inlet section of the cavity (mass flow rate, temperature and pressure) are the same used for the analysis of the cavity equipped with RRs, and namely a mass flow rate of 45 l/min, an inlet pressure of 6 bar, and an inlet temperature of 27 °C.

The choice of a semicircular shape of the channels is mainly due to the manufacturing process adopted for the construction of the resonating region of the cavity. The channels are machined on the inner part of the cavity and, finally, the block above the channels is installed separately in order to obtain the desired cooling strategy for the cavity. Furthermore, the semicircular shape of the channels allows to reduce the coolant frontal area inducing a higher fluid speed inside the channels if compared to the circular shape, maintaining a high heat exchange area in the part of the channels closer to the heated surface of the resonator.

[iii] Highly affected by the computational power available: 2 Intel Xeon E5-2630 v3 eight core HT (2.4 GHz), 128 GB RAM.

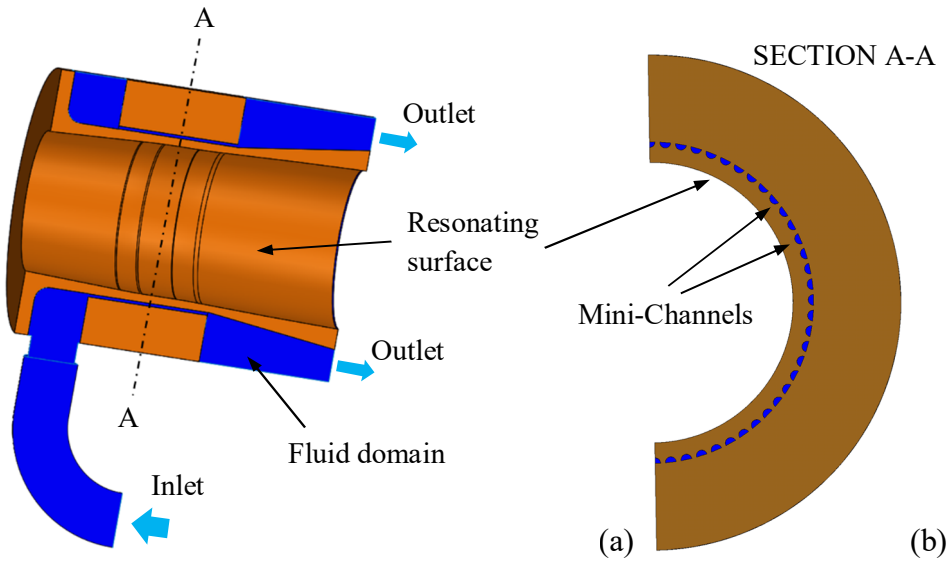

Figure 4.1: (a) Geometrical model of the cavity equipped with MCs for the 170 GHz, 1 MW gyrotron used in the TH simulations, and (b) cross section of the MCs region. Resonating structure is colored in brown and the fluid domain is colored in blue.

Here, the simplified model is used to estimate the HTC at the interface between the solid structure of the cavity and the coolant, defined using (23), to give a reliable temperature field in the glidcop sleeve of the resonator. The output temperature field is used for the evaluation of the resonating surface deformation in the TM model, which is the same for both approaches.

$$HTC = \frac{\Phi_{wall}}{\overline{T}_{wall} - T_{bulk}} \tag{23}$$

In which Φ_{wall} is the average heat flux evaluated on the wall surface, $\overline{T}_{wall}$ the average temperature of the same surface and T_{bulk} is the bulk temperature of the fluid.

The temperature and the deformation profiles on the heated surface of the resonator computed with the complete TH approach, are used as reference solution for the validation of the simplified model. On both complete and simplified model, the same heat load (see Figure 4.2) is applied on the heated surface of the resonator.

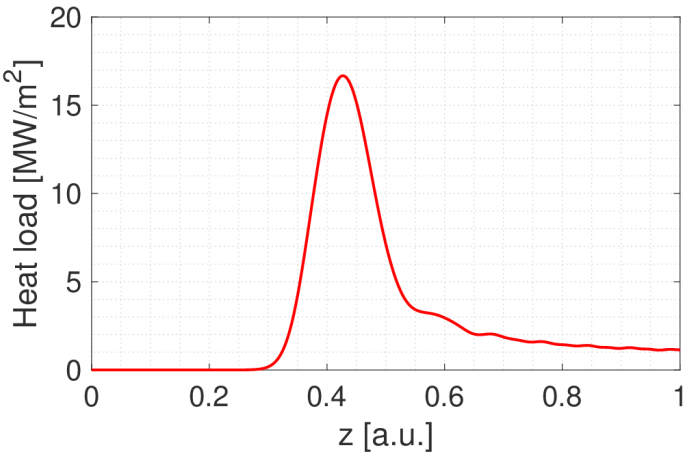

Figure 4.2: Heat load applied on the resonating surface of the cavity equipped with MCs used for both the complete and the simplified TH models.

Different strategies for the evaluation of the HTC are used in the different regions of the cavity. On the channels interfaces, the HTC is computed using the Sieder-Tate correlation [26] for the Nusselt number, in order to include the effects of the wall temperature:

$$Nu_{S.T.} = 0.027\, Re^{4/5} Pr^{1/3} \left(\frac{\mu}{\mu_s}\right)^{0.14} \tag{24}$$

in which Pr is the Prandtl number, μ and μ_s are the dynamic viscosity of the fluid evaluated at the inlet conditions and at the temperature of the solid interface, respectively. The characteristic dimension used to define the dimensionless numbers is the hydraulic diameter of the semicircular channels. The assumption made included: a uniform mass flow rate distribution between the MCs (to compute Re) and all the properties of the coolant evaluated at the inlet boundary conditions.

In order to reproduce the effects of the water cooling in the up-taper region of the cavity and on the "inlet manifold" (see Figure 4.3), the average value of the two HTC coefficients is evaluated in these regions directly from the complete TH simulation by means of the field function "*Heat Transfer Coefficient*", defined in the software STAR-CCM+®, evaluated at the inlet coolant temperature. Figure 4.3 shows the HTC at the solid-water interface as obtained from the complete TH simulation. The simulation models adopted for the complete TH analysis follow the same setup (materials properties, boiling and turbulence model) applied in the simulation of the mock-up equipped with MCs, already validated against experimental results [33].

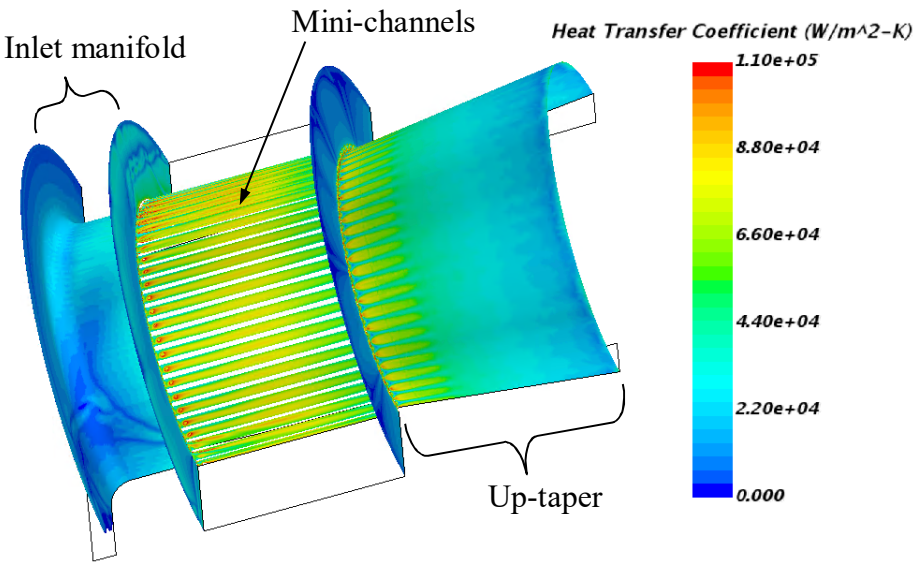

Figure 4.3: HTC map on the solid-water interfaces computed in the compete TH simulation of the cavity equipped with MCs.

The average computed value of the $HTC_{up\text{-}taper}$ is ~3.75 x 10^4 W/m^2 K in the case of nominal inlet flow rate (i.e. 45 l/min). Figure 4.3 shows that the $HTC_{up\text{-}taper}$ changes considerably moving toward the outlet of the cavity. Close to the channels outlets, the high value of the HTC is due to the positive cooling effect of the fluid which leave the MCs and hits, at high velocity, the solid surface of the resonator. The fluid near the outlet of the cavity shows a lower speed in the region in contact with the solid surface (see Figure 4.4), and, consequently, a lower value of the HTC.

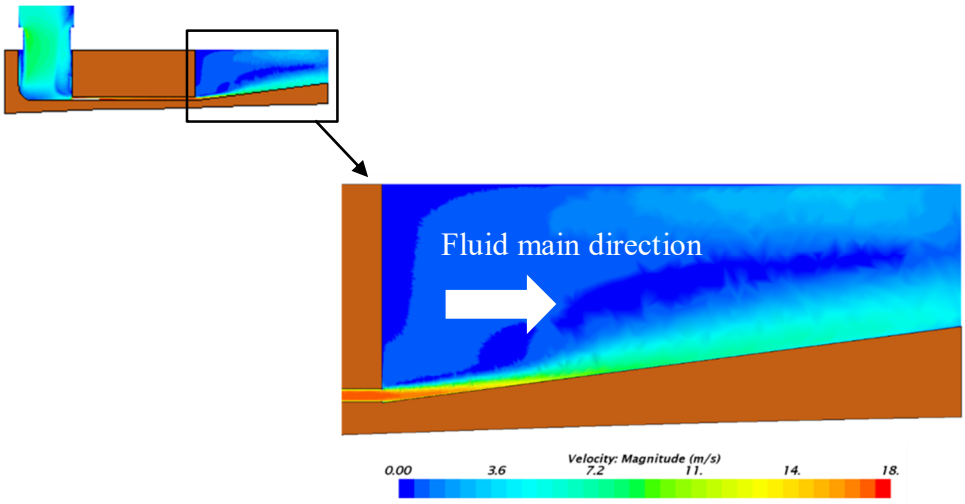

Figure 4.4: Fluid speed computed in the symmetry plane of the fluid region in the up-taper of the cavity equipped with MCs.

The evaluation for the average value of the $HTC_{up\text{-}taper}$ for different cavity inlet mass flow rates, is correlated to the effective outer diameter ($D_{effective\ outer}$) of the annular fluid region in the up-taper region, according to equation (25).

$$Nu = \frac{HTC_{up-taper} \cdot D_h}{k} = 0.023 \left(\frac{\rho\, v\, D_h}{\mu}\right)^{4/5} Pr^{0.4} \qquad (25)$$

in which Nu is the Nusselt number, $D_h = D_{effective\ outer} - D_{inner}$ is the hydraulic diameter in an annular duct and v is the fluid average velocity. The water density (ρ), the viscosity (μ) and the Prandtl number (Pr) are evaluated at the inlet thermodynamic conditions. The value of the effective outer diameter defined for the evaluation of the hydraulic diameter of the annulus (see Table 4.1) is related to the HTC obtained with the CFD simulation in nominal mass flow conditions and then maintained unchanged for the other evaluations.

Table 4.1: Dimensions of the up-taper region used for the definition of the average HTC.

Average inner diameter [mm]	51
Outer diameter [mm]	68
Effective outer diameter [mm]	52.3

As far as the region placed before the MCs block is concerned, the average $HTC_{inlet\ manifold}$ is 2.25 x 10^4 W/m^2 K, computed from the complete TH simulation with nominal coolant mass flow rate. Due to the less relevance of this region of the cavity in the evaluation of the temperature distribution (negligible heat load in this region with respect to the other sections of the cavity), the average HTC obtained with the nominal mass flow rate is kept constant for the simulations with modified mass flow rate.

The average temperature and displacements (radial and axial) profiles computed on the heated surface of the resonator are shown in Figure 4.5, comparing the results obtained with the complete TH simulation with those obtained with the simplified model. The model used for the evaluation of the TM behavior of the cavity is the same in both complete and simplified approaches. The comparison shows a good agreement on the temperature profile on the mid-section of the resonator. The temperature peak evaluated with the complete TH model is slightly shifted along the direction of the fluid by the effects of the advection, which is not present in the simplified model. The evaluation of the radial deformation in the simplified model is slightly underestimated in the central region of the cavity, nevertheless the overall behavior of the profile is coherent with the results obtained using the temperature field originating from the complete TH simulation. The profiles of the axial displacement are almost superimposed in the two sets of simulations. Since the temperature in the up-taper region of the cavity is affected by the HTC averaging process, the most important differences are observed in this part of the structure.

A set of TH simulations with different coolant mass flow rates (see Table 4.2) is performed to validate the simplified model against the complete TH simulations. Of course, the inlet temperature and the pressure are the same used the complete simulations with nominal mass flow rate.

Table 4.2: Flow conditions used for the validation of the simplified model.

Mass flow rate [l/min]	Re in the MCs	$Re_{up\text{-}taper}$*	$HTC_{up\text{-}taper}$ [W/m^2 K]
30	9.5 x10^3	7.2 x10^3	2.68 x10^4
45	1.4x10^4	1.1 x10^4	3.70 x10^4
60	1.9 x10^4	1.5 x10^4	4.66 x10^4

*The $D_{effective\ outer}$ of the up-taper region (see Table 4.1) is maintained constant in the simulations.

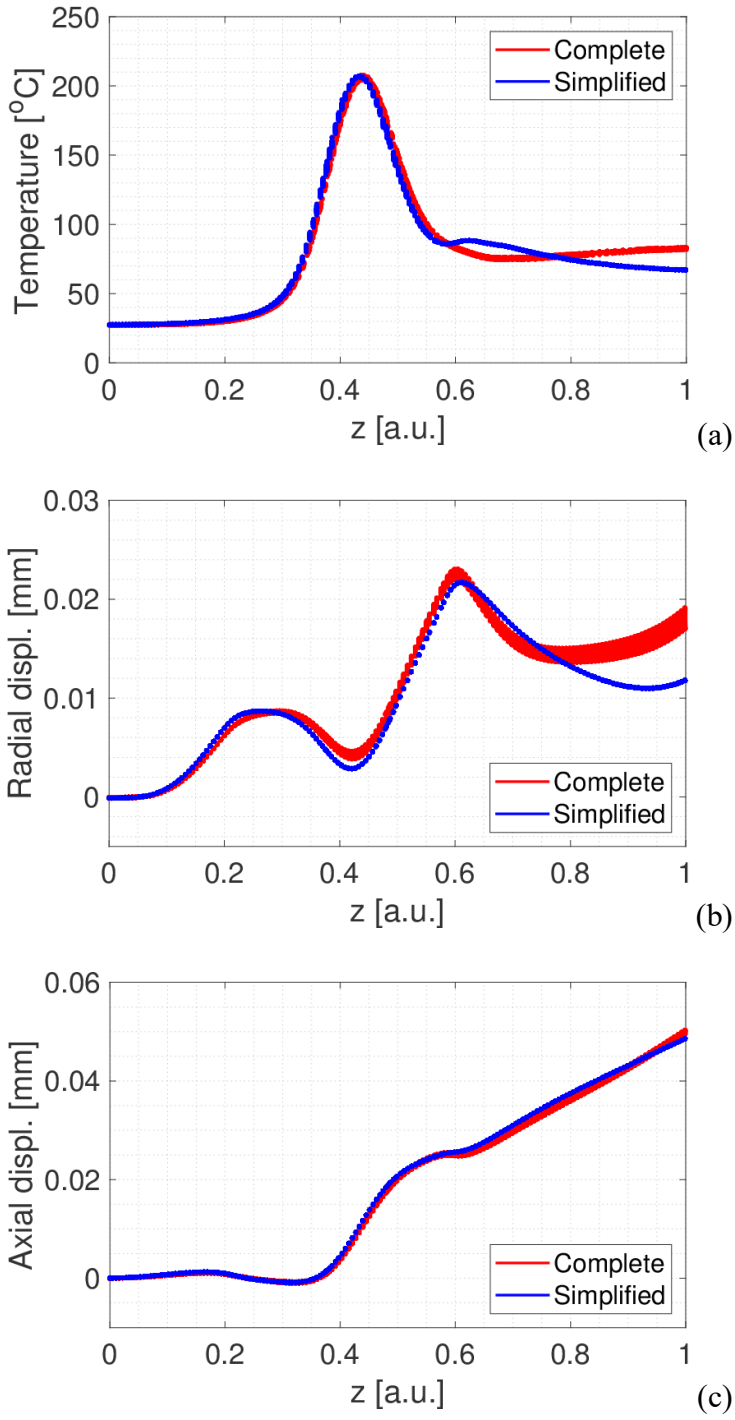

Figure 4.5: Computed (a) temperature, (b) radial and (c) axial displacements profiles with the complete and the simplified models for the definition of the thermal behavior of the cavity equipped with MCs.

The temperature profiles computed with a coolant flow rate of 30 l/min and 60 l/min are shown in Figure 4.6a and Figure 4.6b, respectively. The definition of the HTC in the MCs region adopted in the simplified model gives a very good estimation of the temperature profile at the different operating conditions of the cooling circuits of the cavity simulated. The temperature profiles in the up-taper region follow the trend of the CFD results, showing that the definition of the effective outer diameter proposed for this region works quite well in this geometry also with a different coolant mass flow rates.

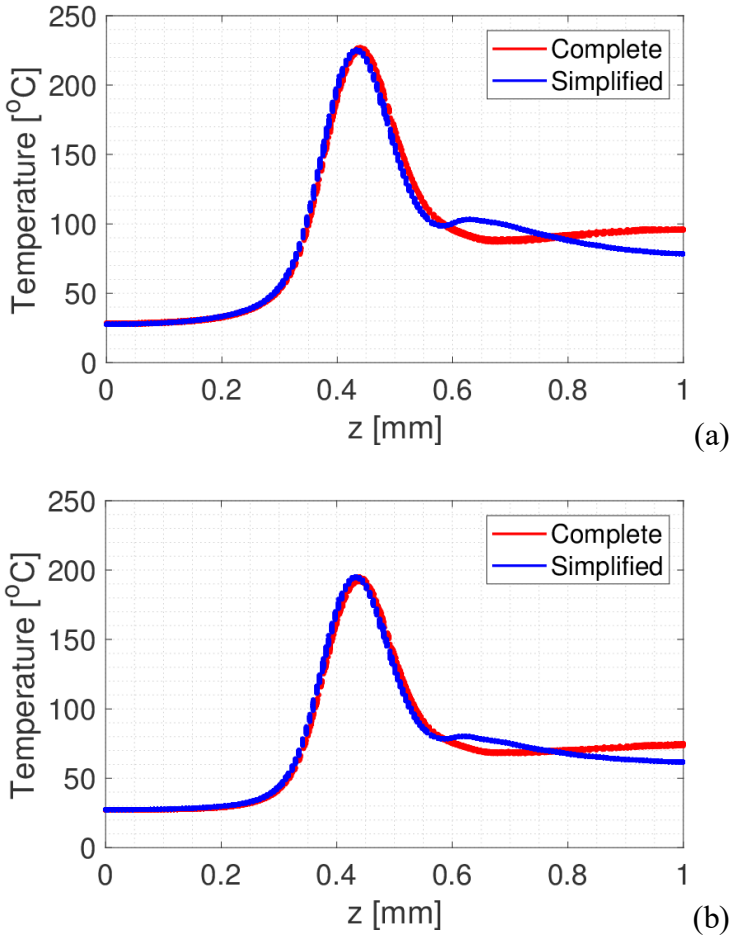

Figure 4.6: Temperature profiles computed with the complete simulation (red lines) and with the simplified model (blue line) with total inlet coolant flow rate of (a) 30 l/min and (b) 60 l/min.

The development of the simplified model to evaluate the effectiveness of the gyrotron cavity cooling, taking into account the cooling effect of water flow, shows very good results in terms of temperature and deformations computed on the heated

surface of the resonating structure if compared to the complete TH model. The evaluation of the average value for the HTC in the up-taper region of the resonator requires the detailed analysis of the results computed by the complete TH model, due to the relevant effects of the coolant velocity and its pathway in this region. The simplified model proposed is able to reproduce adequately well the results of the complete simulations, reducing considerably the computational time of the overall procedure. In this way it is possible to perform extensive parametric studies on the same cavity geometry, with various heat load profiles and mass flow rates. However, variations in the geometry of the cavity require a complete simulation of the component in order to obtain the thermal behavior of the structure and to evaluate the coolant effect in the regions located outside the channels.

4.2 Generalization of the MUCCA simulations results of the cavity equipped with Mini-Channels

The MUCCA tool is now used for the design and optimization of the cooling strategy to be adopted for a new version of the cavity equipped with MCs for the ITER gyrotrons. The CAD drawing of the cavity and the launcher used to define the model adopted in the following simulations, is shown in Figure 1.11.

Thanks to an innovative manufacturing process planned to be used for this cavity, a less stringent constraint is applied in the definition of the channels dimension and shape. The most important differences with respect to the simplified version of the cavity (see paragraph 4.1), involve the minimum thickness of the resonator in the mid-section region, the position and the longitudinal length of the channels. Finally, the outlet region of the cooling circuit of the cavity, which includes the outlet pipe located in correspondence with the launcher section, is included in the model.

Figure 4.7 shows the geometry used for the simulation of the cavity equipped with MCs. The MCs are drilled directly on the resonator structure without any modification to its external and internal surfaces. Furthermore, the longitudinal dimension of the channels covers the entire region of the mid-section and a significant length of the up-taper region, aimed at improving as much as possible the cooling effects in the relevant regions of the resonator. Above the mid-section of the resonator, a copper region called “water stopper” (in green in the Figure 4.7) is in contact with the resonator in order to close the upper flat surface of the channels. The section of the water stopper located near the inlet region of the cooling circuit is

shaped with a smooth curved, called “nose”, to reduce as much as possible the coolant pressure losses helping the coolant enter the inlet section of the channels. The details of the MCs cooling geometry and of the water-stopper block are shown in Figure 4.8.

As already stated in paragraph 1.5, the inlet and outlet pipes are not in symmetric relative position, thus the complete 3D simulation of the geometry is need.

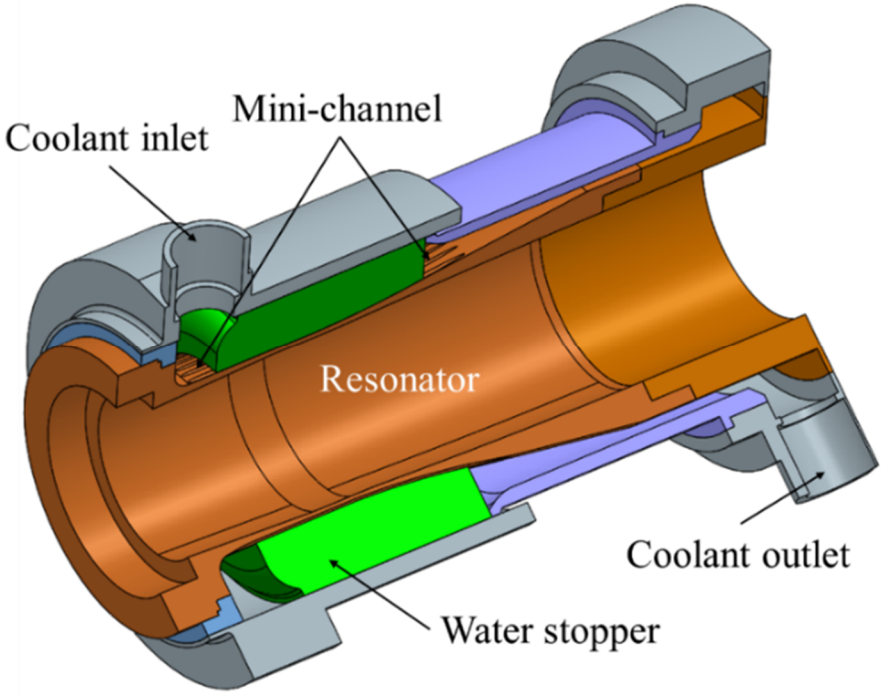

Figure 4.7: CAD model of the cavity equipped with MCs.

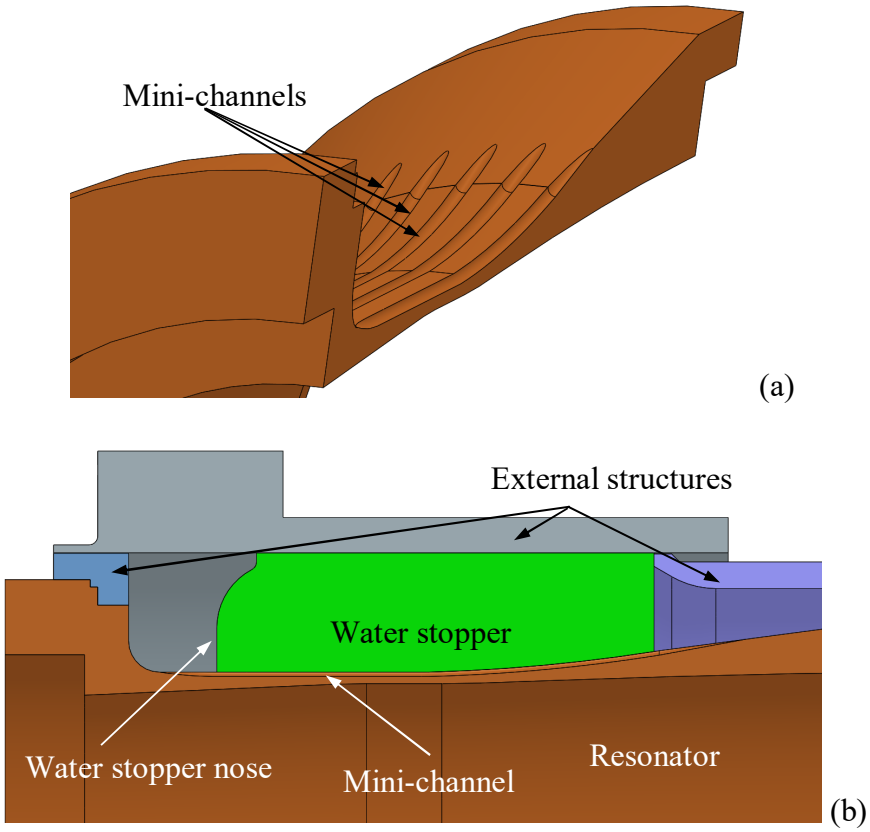

Figure 4.8: Detail of (a) the construction of the mini-channels and of (b) the water-stopper block.

To cool the cavity, inlet water at 40 °C and of 8 bar is used. Thanks to the cavity manufacturing process adopted, the resonator and the water-stopper block can be considered in perfect contact. To reduce the computational domain, the external solid structures of the cavity are not simulated in the TH and TM modules of the MUCCA tool and proper boundary conditions on the surfaces, in contact with the external regions, are applied. The interfaces between the resonator and the water stopper are mechanically connected in the TM simulations, and the lower part of the resonator (the base that is closer to the coolant inlet pipe) is mechanically fixed, see Figure 4.9. The other surfaces are free to move, following the boundary conditions also used for the cavity equipped with RRs.

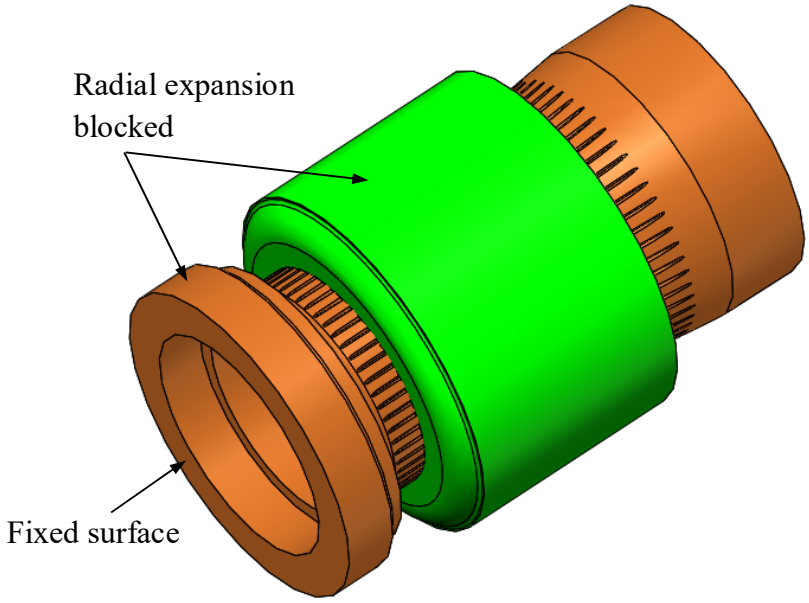

Figure 4.9: Mechanical constraints applied on the cavity equipped with MCs.

The design and the optimization of the cooling circuit of the resonator equipped with MCs relies on the use of 54 semi-circular parallel channels, which follow the outer profile of the resonator, kept unchanged during the geometry optimization. Three different channels diameters (i.e. A = 1 mm, B = 1.5 mm and C = 2 mm) are simulated on the same resonating structure in order to evaluate the hydraulics of the coolant, and the thermo-mechanical response of the resonator. In the three simulated scenarios, the minimum distance between the lower part of the channel and the heated surface of the resonator is fixed, as well as the water conditions on the inlet section of the cavity.

The coolant pressure drop (symbols) computed between the inlet and the outlet section of the cavity and the quadratic fits (curves) are shown in Figure 4.10 for the three proposed designs. The black dashed line at 8 bar indicates the pressure drop limit of the cooling circuit.

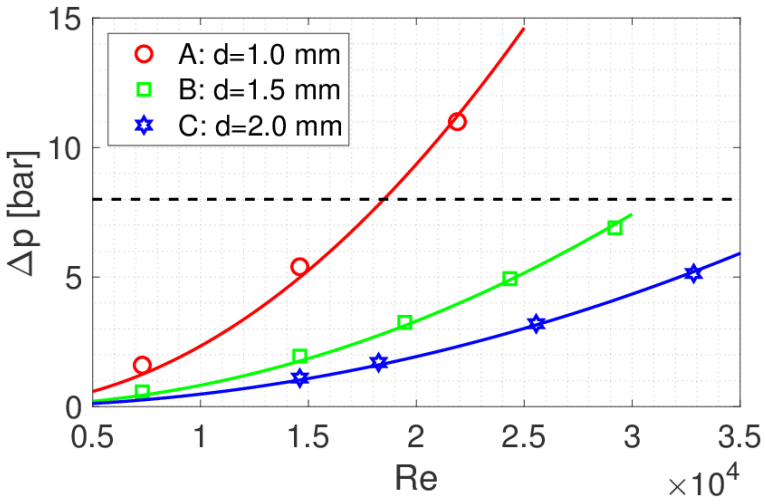

Figure 4.10: Coolant pressure drop curve (open symbols) computed for the three MCs dimensions proposed with the polynomial fit of the CFD results (solid lines). The pressure drop limit of the cavity cooling circuit is also reported (black dashed line).

Equation (26) is the general form of the quadratic fit, which reproduces well the computed pressure losses (the R^2 of the fit curves is >0.99 in the three cases), where "a" is the coefficients from Table 4.3 and Re is the Reynolds number in the channels. In the simulations used for the evaluation of the pressure drop characteristic curves, the heat load is not applied in order to remove the temperature effects on the water properties.

$$\Delta p = a \cdot Re^2 \tag{26}$$

Table 4.3: Coefficient of the polynomial fit for the pressure drop in the cavity equipped with MCs.

Case	MCs diameter [mm]	a
A	1	2.34×10^{-8}
B	1.5	8.26×10^{-9}
C	2	4.83×10^{-9}

For the operating points below the pressure drop limit shown in Figure 4.10, three heat loads (see Figure 4.11) are used to evaluate the temperature (see Figure 4.12) and the deformation (Figure 4.20) on the heated surface of the resonator.

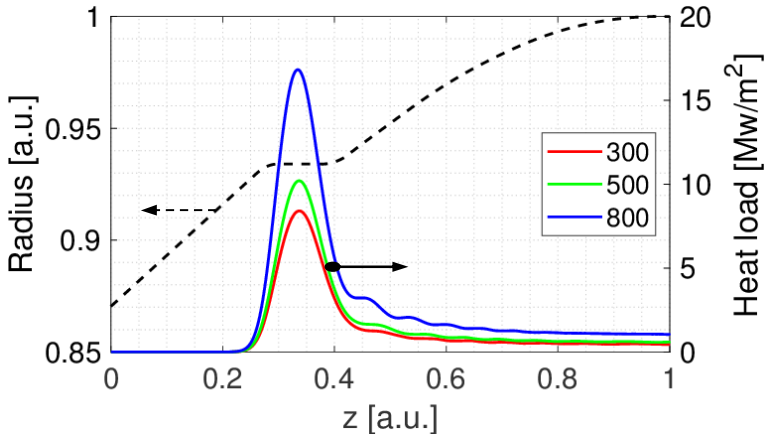

Figure 4.11: Heat loads (left axis) applied on the heated surface of the resonator (right axis) equipped with MCs.

Case B simulated with a mass flow rate of 50 l/min, (nominal value) is used as reference for the following discussion. In the next plots, the computed profiles are not azimuthally averaged in order to show the homogeneity obtained with the MCs cooling configuration on the heated surface of the resonator.

The temperature profiles show, as expected, that the maximum value is located in the mid-section region due to the higher heat flux applied. The temperature increase in the outlet region of the cavity is due to lower cooling performances due to the absence of the channels in this region of the resonator.

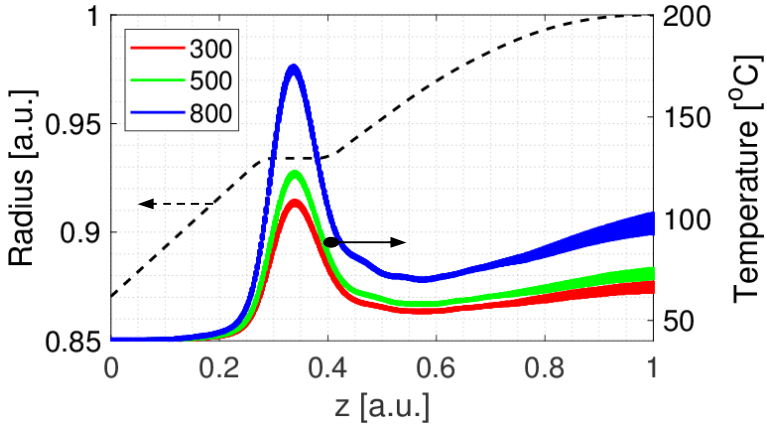

Figure 4.12: Case B: computed temperature distribution on the heated surface of the resonator of the cavity equipped with MCs with inlet mass flow rate of 50 l/min and various heat loads.

Figure 4.13 shows the mass flow rate distribution in the channels of the cavity for the case B with the nominal mass flow rate (i.e. 50 l/min). The relative error (ε) reported is computed with respect to the ideal mass flow rate in the case of uniform mass flow distribution between the channels. The mass flow balance is very good ($\varepsilon_{max} \sim 4$ %), considering only a single inlet and outlet pipe in the cooling circuit of the cavity. The effect of the good mass flow rate repartition in the mid-section of the resonator is very important to obtain a homogeneous temperature distribution and deformation which, during the operation of the gyrotron, maintain the circular shape of the central region of the cavity unchanged.

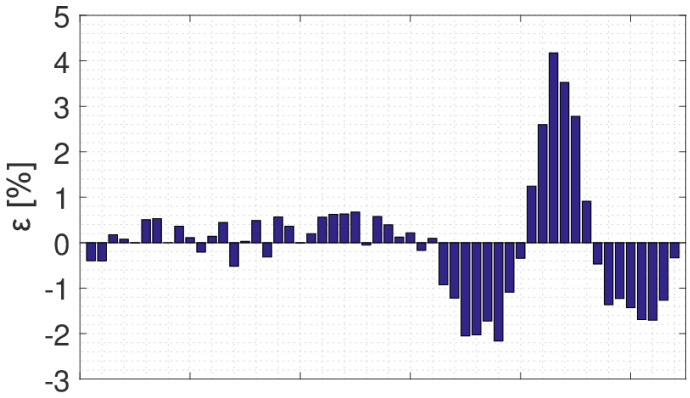

Figure 4.13: Computed relative error of the mass flow rate inside the channels with respect to its average value for case B with nominal mass flow rate.

As already observed in the TH simulation of the preliminary version of the cavity, also the up-taper region is well cooled if compared to the cavity equipped with RRs (see Figure 3.4). This happens thanks to the high speed of the fluid which exits from the channels and hits the outer surface of the resonator (see Figure 4.15).

Figure 4.15 and Figure 4.15 show, respectively, the temperature map and the velocity magnitude of the coolant as computed in a longitudinal cross section of the cavity for case B with nominal mass flow rate and 800 kW heat load. The temperature peak is localized in the central part of the mid-section of the resonator, efficiently cooled thanks to the high velocity of the fluid in the channels (~20 m/s). For the same simulation, the map of the absolute pressure in the coolant is shown in Figure 4.16. The overall pressure drop in the fluid is mainly due to the inlet section of the channels, which produce a localized pressure drop of ~3 bar over a total ~5 bar, computed between the inlet and the outlet section of the simulated cavity.

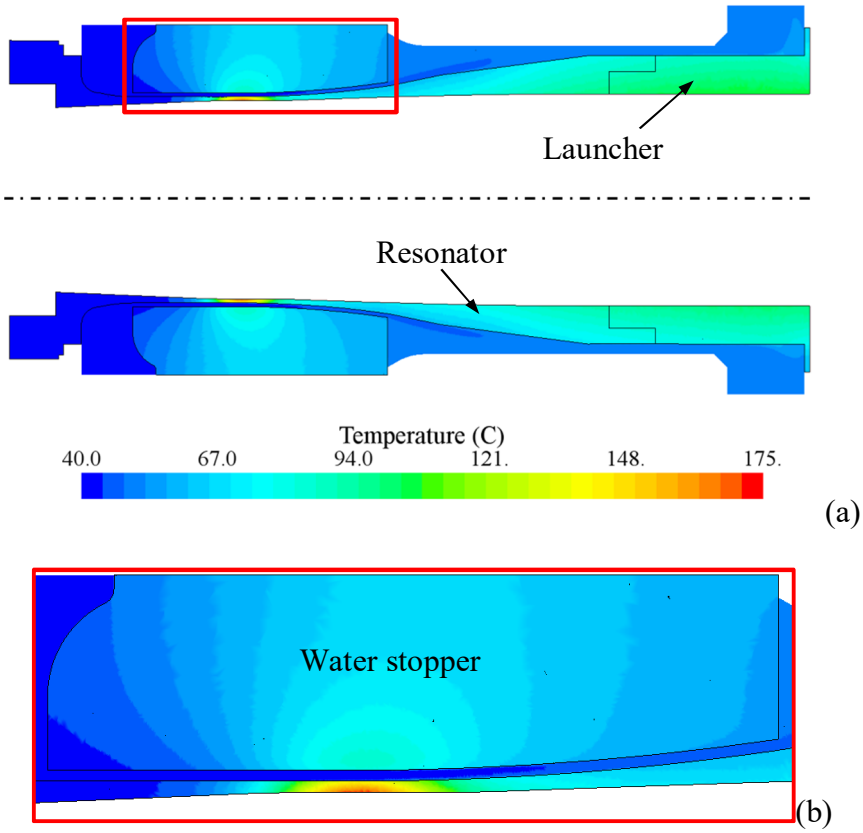

Figure 4.14: Computed (a) temperature map in the longitudinal cross section of the cavity equipped with MCs for case B with nominal mass flow rate and 800 kW heat load, and (b) zoom in the mid-section region of the resonator.

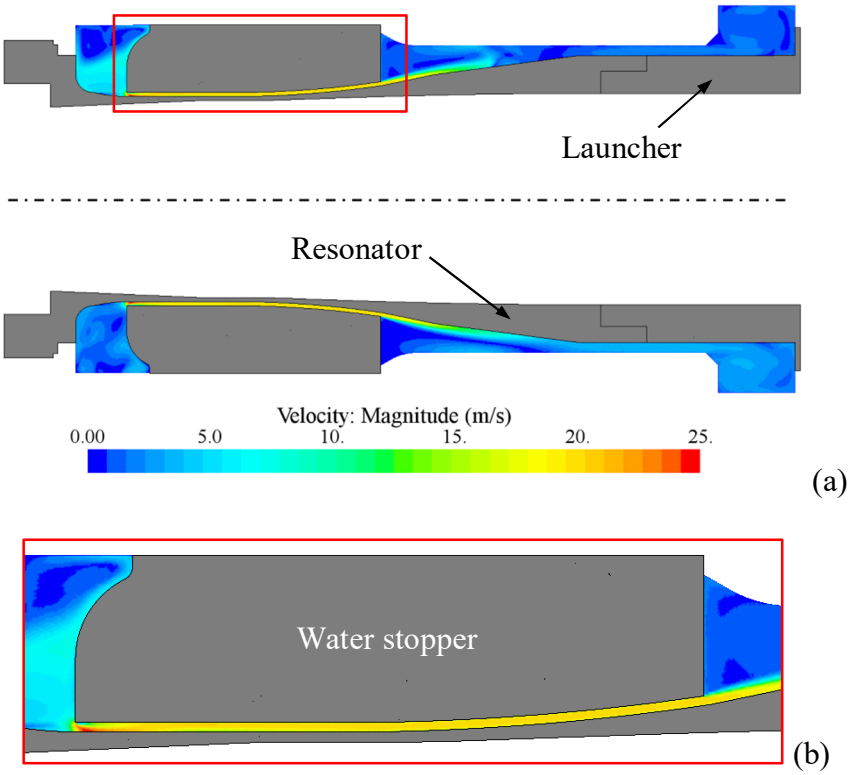

Figure 4.15: Computed (a) velocity map in the longitudinal cross section of the cavity equipped with MCs for case B with nominal mass flow rate, and (b) zoom in the mid-section region of the resonator.

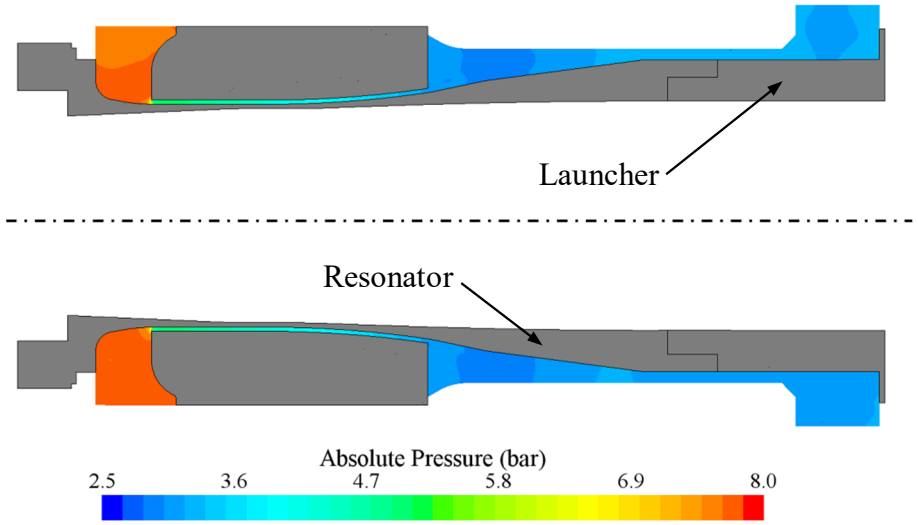

Figure 4.16: Computed absolute pressure in the longitudinal cross section of the cavity equipped with MCs for case B with nominal mass flow rate.

No boiling occurs in this specific case thanks to the high coolant mass flow rate inside the channels. However, if the mass flow rate is reduced to 15 l/min, while other parameters are kept constant, the coolant boiling occurs, close to the peak load location, on a longitudinal length of some millimeters (see Figure 4.17).

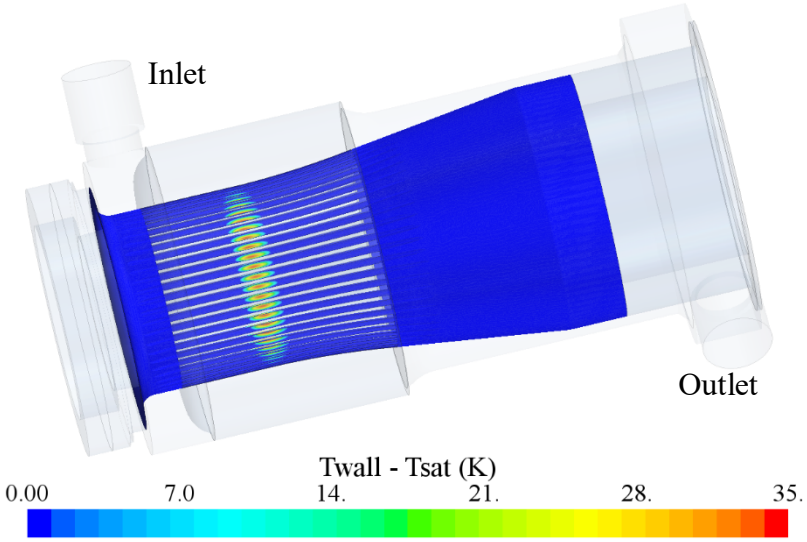

Figure 4.17: Computed temperature difference between the solid surface (T_{wall}) and the fluid saturation temperature (T_{sat}) in the interface of the cavity equipped with MCs, for case B with inlet flow rate of 15 l/min and 800 kW working condition.

The temperature difference computed in the three heat load profiles is reflected on the deformation profiles, see Figure 4.18, which are more relevant in the case of the 800 kW heat load, due to higher temperature reached on the solid structure of the resonator. The radial component of the deformation is highly dependent on the mechanical constraints applied on the external region of the water-stopper (the surfaces in contact with the stainless steel region) which avoids the radial expansion of the resonator. In the region in correspondence the water stopper (~0.2 < z < ~0.6), the radius of the inner surface of the resonator tends to move inward, modifying considerably the flat shape of the resonating mid-section surface (see Figure 4.18a). This deformation field obtained in the structure, certainly affects the resonating behavior of the cavity and its effects have to be carefully investigated during the design phase of the component.

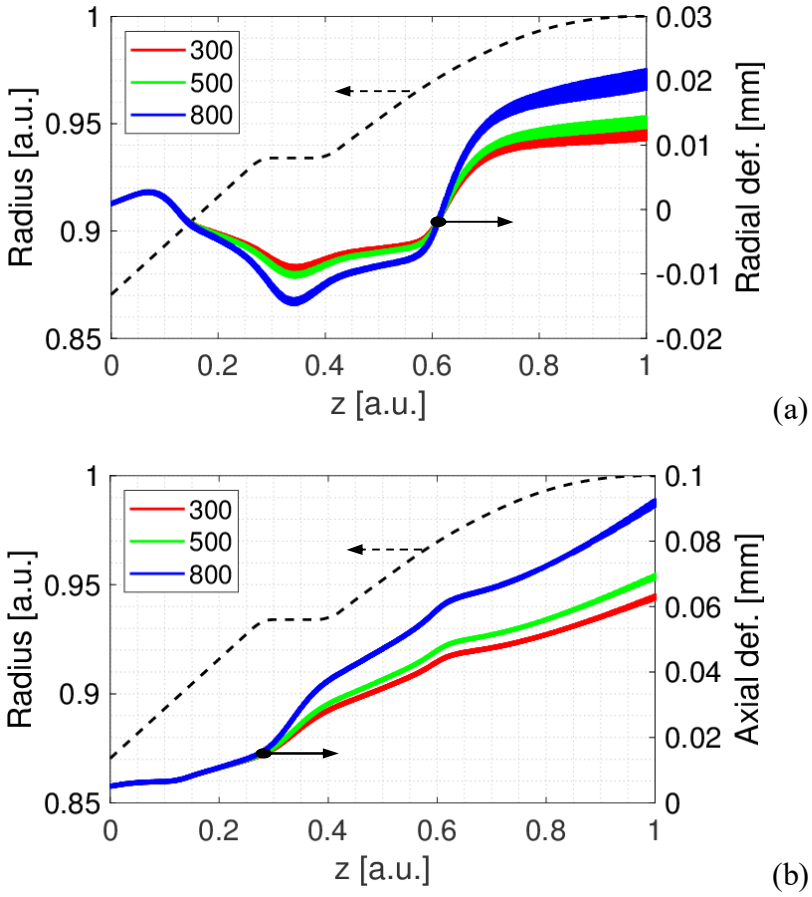

Figure 4.18: Computed (a) radial and (b) axial deformations on the heated surface of the resonator for case B with nominal mass flow rate.

The global behavior of the cavity equipped with MCs is described in terms of the maximum temperature computed on the heated surface of the resonator (see Figure 4.19) for the various inlet coolant mass flow rates considered, as a function of the peak value of the heat loads applied. The figures legends indicate with a letter the geometry used (see Table 4.3) and with a number the inlet flow rates, expressed in l/min. The maximum temperature computed on the heated surface of the resonator is always below 250 °C, which is considered the temperature limit for the cavity operation. The results show a linear trend of the maximum temperature in the case of the higher coolant mass flow rate (e.g. cases B30-60 and C40-90). For the lower values of the Reynolds number inside the MCs (e.g. case A10 and B15), the temperature computed at the higher heat flux is lower the expected temperature, evaluated considering a perfect linear trend with respect to the two lower point, thanks to the presence of boiling in correspondence with the temperature peak (see Figure 4.17) that improves the cooling capability of the component. In order to simplify the comprehension of Figure 4.19 and Figure 4.20, the conditions used for the simulation are shown in Table 4.4.

Table 4.4: Details of the simulations performed for the resonator equipped with MCs.

Label	Channels diameter [mm]	Mass flow rate [kg/s]	Re inside channels [-]
A10	1.0	0.17	7300
A20	1.0	0.33	14600
B15	1.5	0.25	7300
B30	1.5	0.50	14600
B40	1.5	0.66	19500
B60	1.5	1.0	29200
C40	2.0	0.66	14600
C50	2.0	0.83	18300
C70	2.0	1.16	25600
C90	2.0	1.5	32900

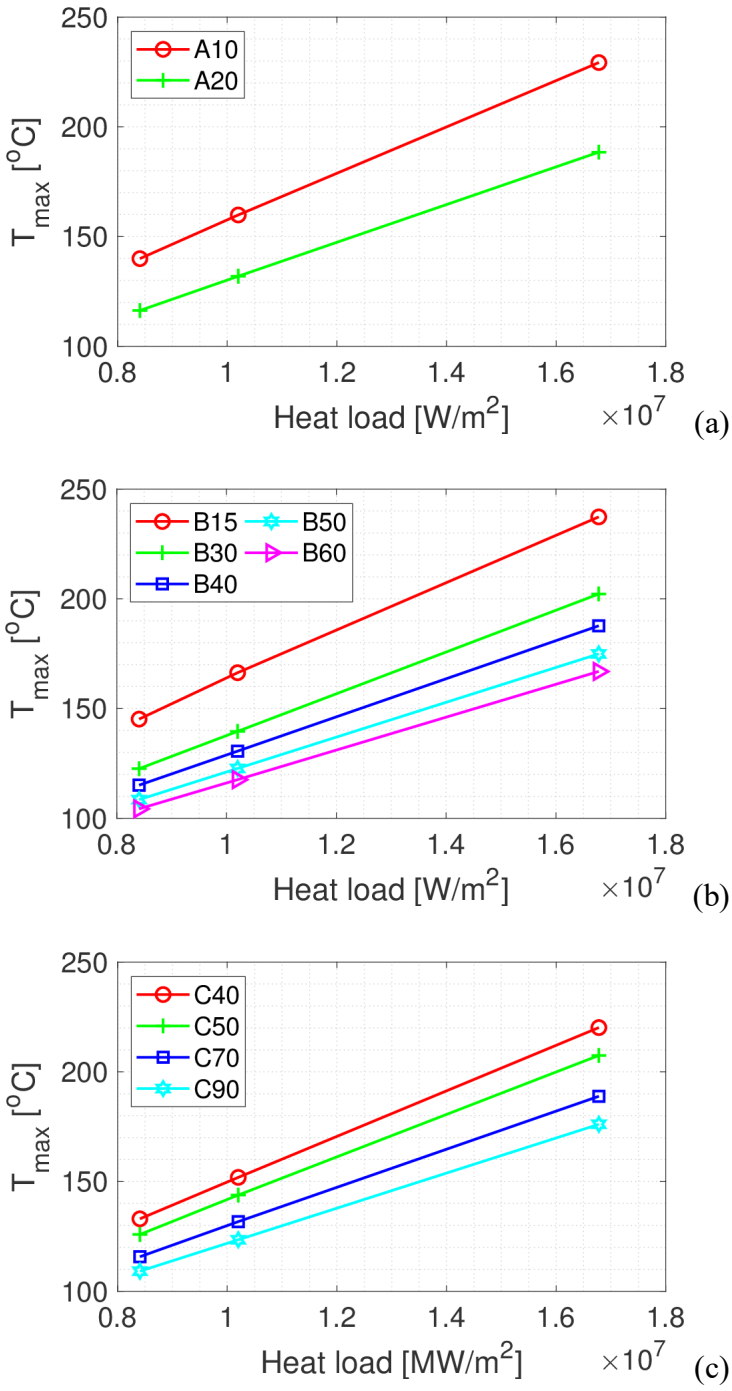

Figure 4.19: Computed maximum temperature on the heated surface of the resonator for case (a) A (d = 1 mm), (b) B (d = 1.5 mm) and (c) C (d = 2 mm).

Following the generalization procedure adopted in the case of the cavity equipped with RRs (see paragraph 3.3), the general behavior of the cavity equipped with MCs is described in Figure 4.20, which shows the average radial deformations computed at the center of the mid-section of the resonator, as a function of the value of the heat load applied on the same location. The deformation is linearly dependent on the heat load and the linear fit obtained from the simulations of each resonator cooling design have not intersection with the others, meaning that the qualitative behavior of the component is not dependent to the channels diameter in the range of conditions simulated. The minus sign in the deformation shown in Figure 4.20 are due to the reduction of the computed internal radius of the resonating surface of the cavity, since the presence of the water stopper region does not allow the resonator to expand. This behavior is completely different with respect to the cavity equipped with RRs, in which the thermal expansion of the resonator is not stopped by a solid region placed above the heavily heated part of the cavity.

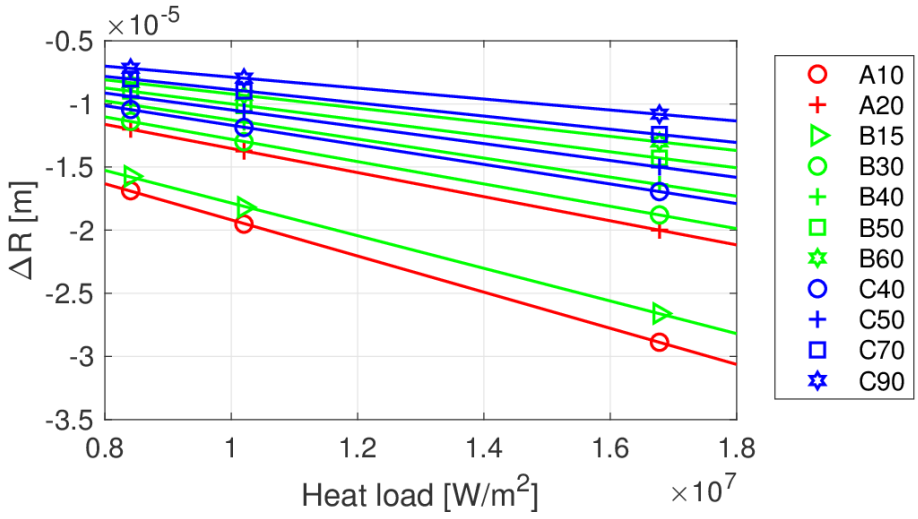

Figure 4.20: Computed radial deformation as a function of the heat load, both evaluated at the center of the mid-section of the resonator equipped with MCs, for various channels dimensions and mass flow rates (see text).

Following the procedure described in Paragraph 3.3, the slopes of the curves obtained from the linear fits of the computed results shown in Figure 4.20 are reported in Figure 4.21, as a function of the average Reynolds number evaluated inside the channels at the inlet water conditions, and assuming a uniform mass flow rate distribution among the channels.

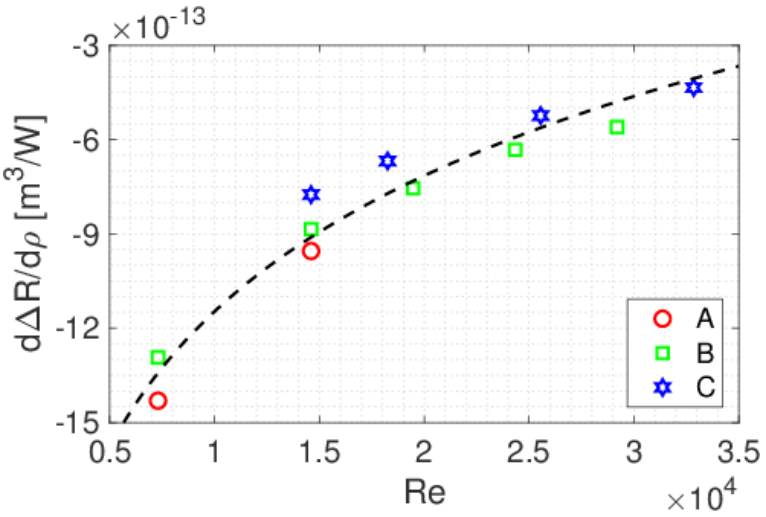

Figure 4.21: Variation of the ΔR/dρ as a function of Re inside the channels of the cavity equipped with MCs.

The results computed in the three geometries are fitted with the logarithmic curve reported as a dashed black line in Figure 4.21 and defined in (27), which is characterized by R^2 of 0.947. The error due to statistical inference on the fit slopes of Figure 4.20 is, in any situation, smaller than 0.5% due to the very high quality of the linear fit on the computed data. Furthermore, the limited number of simulations results (i.e. 3) does not allow to perform a valid statistical inference on the fit parameters. For these reason the value of the error are not reported in Figure 4.21.

$$\frac{d\,\Delta R}{d\,\rho} = 6.23 \cdot 10^{-13} \cdot \ln Re - 6.88 \cdot 10^{-12} \tag{27}$$

In this way, the behavior of different layout of the cavity equipped with MCs can be generalized as a function of the Reynolds number with an average relative error of 6 % (max 15 %) and therefore to determine a priori the thermal response of the resonating structure induced by a change of the dimension of the diameter of the channels or by the variation of the inlet mass flow rate. The results of this procedure can be used to reduce the design phase period for the definition of the strategy to be adopted in the cavity cooling circuit.

In order to verify the method proposed for the general description of the resonator, a set of simulation is performed modifying the number of the channels in the resonator cooling structure. In total, 72 semicircular channels with 1 mm of diameter is modelled, applying the flow rate of 35 l/min to obtain an average Reynolds number of ~19000. The results of the new resonator cooling structure is compared

in Figure 4.22 with the fit curve (black dashed line) obtained from the computed results obtained previously. The prediction bounds of the fit curve (black dotted lines) is obtained with a confidence interval of 95 %. Based on the simulations result, the effect of the number of channels in the resonator cooling structure seems not relevant in the model proposed.

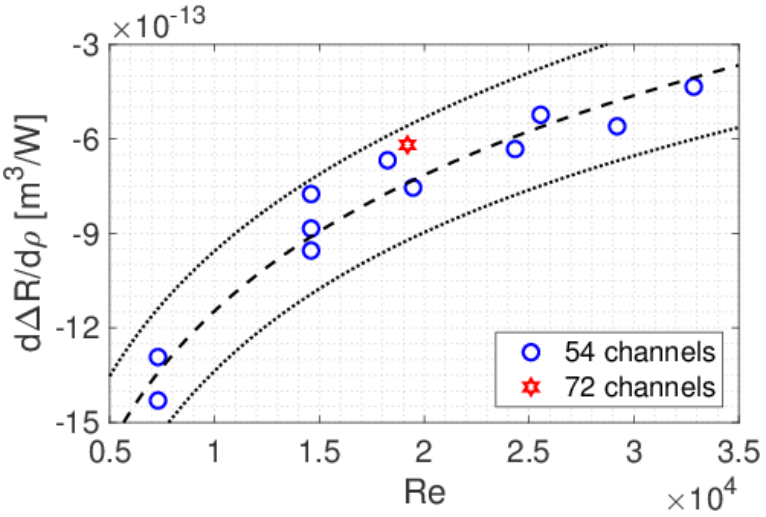

Figure 4.22: Comparison between simulation results with resonator equipped with 54 MCs (blue circles) and with 72 MCs (red star). Fit curve of the simulations results with 54 MCs is reported (black dashed line) with prediction bounds (black dotted lines) obtained with confidence interval of 95 %.

From the simulations point of view, it is clear that the deformation behavior of the heated surface of the cavity depends from many geometrical and coolant flow conditions. However, the description of the global TH and TM behavior of the cavity equipped with MCs based on the average Reynolds number of the coolant inside the channels, which is proposed in this work, seems reasonable for the first stage of the design process of the component.

4.3 Summary

In this chapter, the MUCCA tool has been applied on the cavity equipped with MCs for the 1 MW European gyrotron. The MCs strategy represents the cooling alternative to the use of the RRs porous medium, which is currently applied on the ITER gyrotron prototypes, as discussed in Chapter 3.

A set of simulations has been performed on a preliminary cavity geometry in order to define a simplified thermal model aiming at reducing the computational

cost of the TH simulations of the MUCCA tool. In this model, the heat transfer coefficient of the coolant has been evaluated by empirical correlations based on the Reynolds number computed on the different locations of the cavity cooling structure. The results of the simplified thermal model are in agreement with the MUCCA tool results involving CFD simulation of the coolant behavior. The reduction of the computational time is consistent, which allows to increase the number of simulation necessary to determine parametrically the behavior of the cavity, fixing the geometrical characteristics of the component.

In the last part of the chapter the MUCCA tool has been used for the design and the optimization of the MCs cooling strategy to be applied on the ITER gyrotrons. A parametrical study on the channels dimension has been performed determining the general behavior of the resonating structure deformation based on the average Reynolds number of the coolant inside the channels, fixing the number of the channels (i.e. 54). The same strategy adopted in the Chapter 3 has been used for the generalization of the description of the resonator. Finally, a set of simulation has been performed modifying the number of the channels (i.e. 72) obtaining results which are well described by the general model defined with a lower number of channels.

The TH results of the simulation performed on the cavity equipped with MCs are very promising, since the mass flow rate repartition in the channels is good and the maximum temperature computed on the internal surface of the resonating region is lower if compared to the RRs design, in almost similar heat load and mass flow rate conditions. The most relevant drawback of the MCs cooling alternative is the high pressure drop computed between the inlet and the outlet section of the cavity, which needs a particular attention in the design phase of the in order to respect the working characteristics of the gyrotron cooling circuit.

The experimental campaign on the cavity equipped with MCs has not been performed yet, thus it is not possible to validate the results obtained with the MUCCA tool. Thales Electron Devices has planned a campaign for 2019 – 2020 to design and test a relevant mock-up of the cavity equipped with MCs. The test campaign will be used to validate the simulation methods adopted and to verify the manufacturability of the component consistently with the new process planned.

Chapter 5

Analysis of the 2 MW DEMO gyrotron cavity with coaxial insert[i]

In this chapter, the MUCCA tool is applied for the simulation of the coaxial cavity[ii] under development at KIT for the 170 GHz, 2 MW gyrotrons to be used in the DEMO EC system [43]. The main characteristic of this cavity is the presence of the coaxial insert used to improve the gyrotron performances.

A preliminary steady state simulation of the cavity resonator and of the coaxial insert is performed applying fixed heat load to evaluate the main thermo-mechanical characteristics of the cooling configuration of the two components[iii]. Based on these results, some improvements of the cooling circuit of the gyrotron cavity are proposed to reduce the temperature non uniformity computed on the resonator.

In the last part of the chapter, transient simulations are performed on the cavity resonator and on the coaxial insert to evaluate the time behaviour of the two resonating structures and to determine the maximum pulse length with the cooling strategy adopted.

---

[i] The material presented in this chapter is mainly based on [44] and [44].

[ii] The information about the dimensions of the geometries of the cavity and of the coaxial insert described in this chapter, are under confidentiality restriction and are reported scaled with respect to the total length and the maximum radius of the components.

[iii] The setting of the boiling model used in the cavity equipped with MCs is used also in the simulations of the coaxial cavity.

5.1 The resonator of the coaxial cavity

The upper view and the longitudinal cross section of the cavity of the 170 GHz, 2 MW gyrotron are shown in Figure 5.1a and Figure 5.1b, respectively [44]- [45]. The cut planes shown in Figure 5.1a pass through the centre of the inlet and of the outlet pipes of the cavity, which are not in reciprocal symmetric position. The angle between the centres of the two pipes is ~150°. This does not allow to perform any symmetric simplification of the geometry. Therefore it is necessary to perform a full 3D simulation to assess correctly the fluid flow path in the cooling circuit of the cavity. The axial dimension of the resonator is ~15 cm and the internal radius of the resonator is ~3 cm.

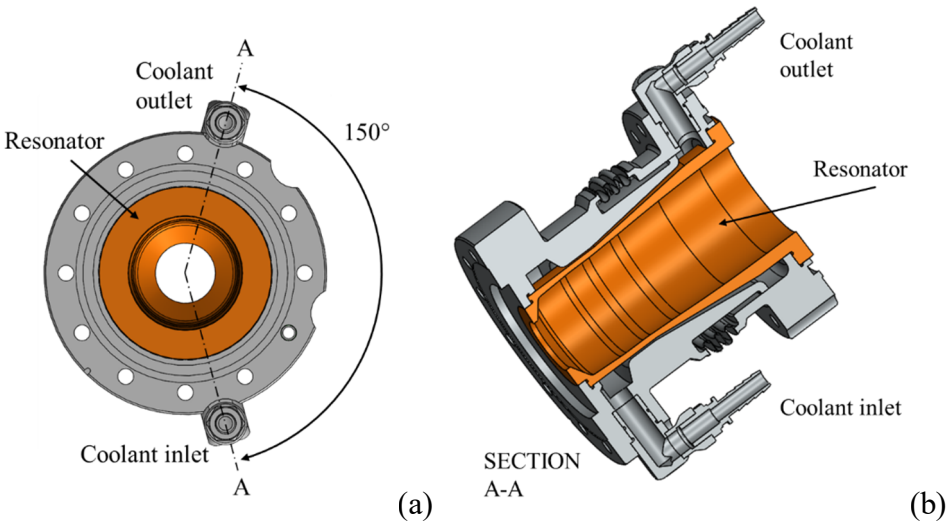

Figure 5.1: CAD model of the cavity of the 170 GHz, 2 MW gyrotron for DEMO: (a) upper view and (b) longitudinal cross section along A-A planes.

The radial profile of the resonator and of the heat load applied at the beginning of the transient are shown in Figure 5.2, with the later already used in the preliminary steady state simulation performed on the resonator. The initial heat load is computed with the EURIDICE® code assuming the nominal un-deformed profiles of the resonating surfaces of the cavity, which is assumed at constant temperature of 27 °C.

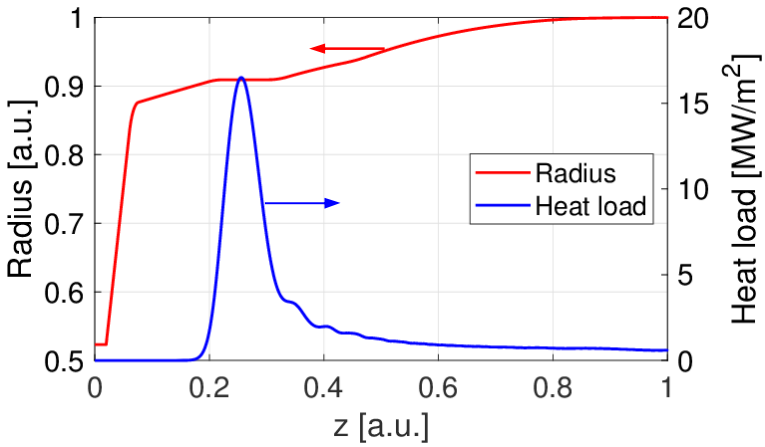

Figure 5.2: Initial heat load (blue, right axis) and radial profile of the resonator heated surface (red, left axis) of the coaxial cavity for the 170 GHz, 2 MW gyrotrons.

The cooling configuration of the resonator relies on an annular cooling channel running between the outer surface of the resonator and the inner surface of the external stainless steel structure. The minimum thickness of the annulus is located near the mid-section region of the resonator to increase the fluid speed in the most critical region of the cavity, i.e. where the heat load is peaked (see Figure 5.2). The details of the resonator are shown in Figure 5.3.

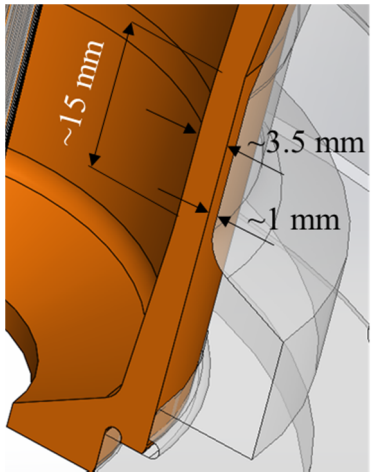

Figure 5.3: Zoom of the central region of the annular cavity.

The inlet section of the resonator cooling circuit is characterized by a volumetric flow rate of 3.7 m^3/h at the constant temperature of 40 °C and the pressure of 8 bar [44]. As performed in previous analyses, see Chapter 3 and Chapter 4, the reference pressure set on the outlet section of the cavity is used to compute the target pressure on the inlet section and therefore to evaluate if boiling occurs.

5.1.1 Preliminary steady state simulation on the annular cooling geometry of the coaxial cavity

A set of preliminary TH and TM steady state simulations is performed on the resonator of the coaxial cavity to evaluate the temperature distribution and the deformations on its heated surface. The aim of this analysis is to highlight the criticalities on the cooling performance of the resonator caused by the annular cooling configuration adopted. Based on the steady state results, two modifications, aimed at enhancing the thermal performance of the cavity cooling circuit, are proposed to improve the overall thermal behaviour of the resonator.

The temperature maps and the temperature profile computed on the heated surface of the resonator are shown in Figure 5.4a and Figure 5.4b, respectively. The profile in Figure 5.4b is not azimuthally averaged in order to point out the non-uniformity computed along the axial length of heated surface by means of the line thickness, and to locate the main criticalities related to the cooling strategies adopted.

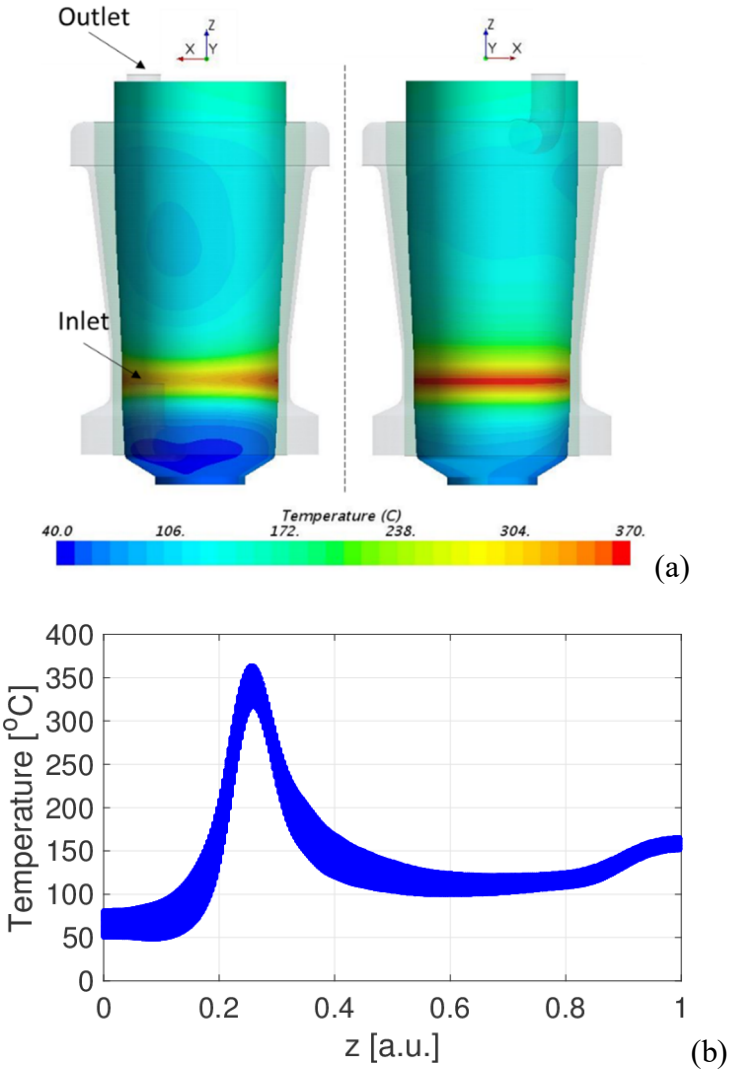

Figure 5.4: Computed (a) temperature maps and (b) profile on the heated surface of the resonator in the annular cooled cavity.

The maximum temperature computed on the heated surface of the coaxial cavity is ~365 °C, located in the mid-section region of the resonator (z ~ 0.25). The temperature non-uniformity in correspondence with the temperature peak is ~50 °C, caused by a non-optimum mass flow rate distribution on in the mid-section region of the cavity, as shown by the coolant streamlines displayed in Figure 5.5. The fluid velocity in the region closer to the inlet pipe (red circle of Figure 5.5) is significantly higher if compared with the velocity computed in the opposite position of the cooling circuit of the resonator. This behavior leads to a strong non-uniform value of the HTC and, consequently, a different cooling of the resonating structure as shown

in Figure 5.4. Thanks to the absence of shrinkages in the cooling circuit of the resonator and the very low pressure impedance of the annular cooling strategy, the coolant pressure drop between the inlet and the outlet is ~0.6 bar.

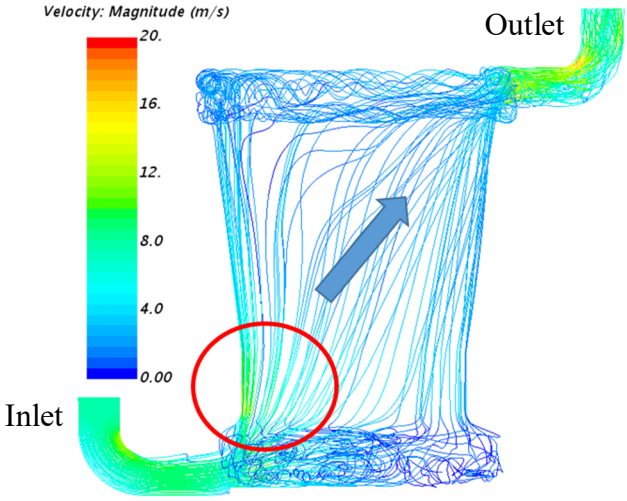

Figure 5.5: Coolant streamlines in the cooling circuit of the annular cavity. The red circle highlights the region with higher fluid velocity. The blue arrow displays the main flow direction.

The temperature map in the resonator and in the coolant obtained with a longitudinal cross section of the cavity, and the temperature map on a cross section orthogonal to the longitudinal axes located in correspondence with the temperature peak, are shown in Figure 5.6 (the temperature non-uniformity already discussed in the previous plot is stressed again). In addition, the non-uniformity is also observed in the upper region of the cavity due to the non-perfect mass flow rate distribution of the coolant in this region. In contrast with the cavity designed for ITER equipped with RRs (see Chapter 3), the temperature results show that the local temperature peak is not located in the up-taper region the coaxial cavity, since the frontal flow area is maintained approximatively constant along the whole length of the resonator cooling region.

The axial and the radial displacements computed on the heated surface of the resonator reflect the temperature non-uniformity and they are shown in Figure 5.7: such result is evident on the region with the peak heat load ($0.2 < z < 0.4$), in the case of the radial displacement, and on the lower part of the resonating surface ($z \sim 0$) in the case of the axial displacement, which is dependent to the mechanical constraint applied on the structure. Fixed mechanical constraint is applied on the

top of the cavity close to the outlet pipe (z = 1), in which both deformations are zero. Thanks to the annular cooling configuration, the surface of the resonator facing to the fluid is free to expand, since it is not in contact with the external structure of the cavity.

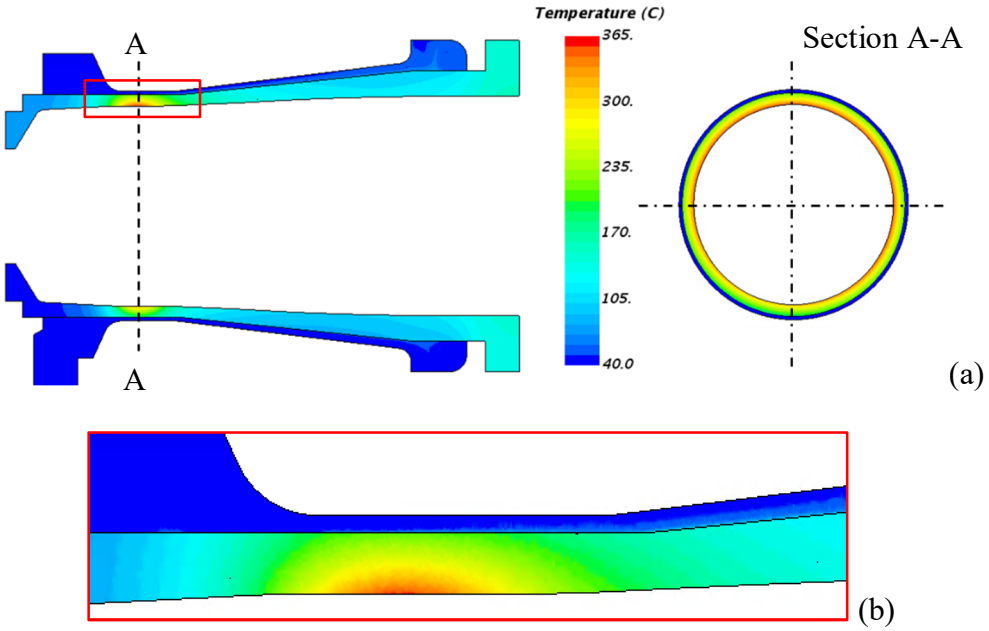

Figure 5.6: (a) Computed temperature maps of the annular cavity resonator on a longitudinal cross section in correspondence with the inlet pipe and on a cross section (A-A) orthogonal to the longitudinal axes in correspondence with the peak temperature and (b) zoom in the mid-section region of the resonator.

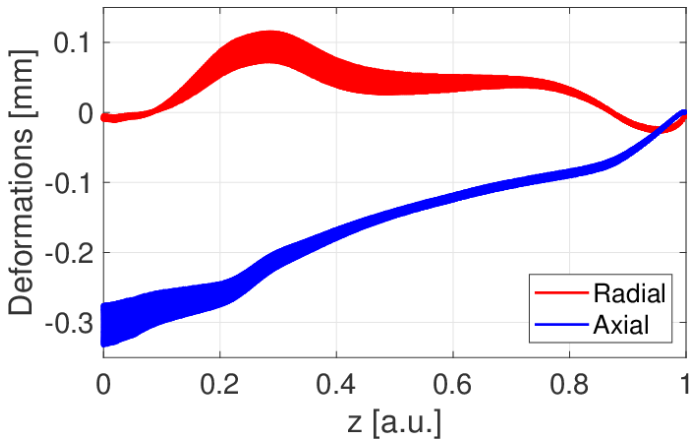

Figure 5.7: Radial and axial displacements of the heated surface of the resonator with annular cavity.

5.1.2 Optimization of the resonator annular cooling strategy

Two different optimization strategies of the cooling circuit of the cavity are proposed aimed at reducing the temperature non-uniformity in the mid-section region of the resonator.

The first option reverses the flow direction, modifying the cavity connection with the external cooling circuit of the gyrotron. This cooling strategy is called for simplicity "Top-Down" (T-D) configuration, as an alternative to the nominal "Bottom-Up" (B-U) configuration, which results are discussed above. Figure 5.8 shows the streamlines in the T-D configuration monitoring the velocity magnitude of the coolant which are compared, in the polar plot of Figure 5.9, to the velocity of the B-U configuration, computed on a cross section in the region of the mid-section of the resonator.

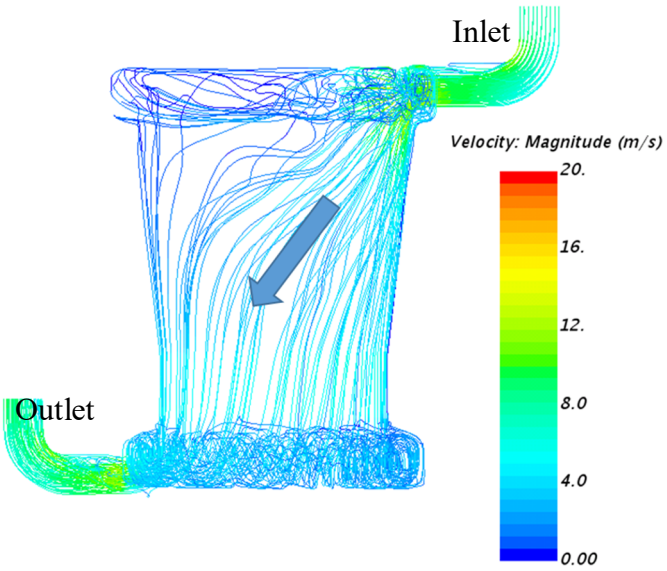

Figure 5.8: Computed fluid streamlines for the annular coaxial cavity in the T-D cooling configurations. The blue arrow shows the main flow direction.

In the T-D configuration, the fluid experiences a more uniform mass flow distribution on the lower region of the cavity due to a larger distance from the cavity inlet section. The comparison of the velocities magnitude computed at $z \sim 0.25$ (see Figure 5.9) shows that in the nominal B-U configuration the fluid velocity is highly non-homogeneous, as already shown in Figure 5.5. In this configuration the maximum velocity (> 10 m/s) is computed close to the fluid inlet (located at 75° in the

polar plot) turning into a higher HTC. Vice versa, in the opposite region, the velocity is considerably lower (< 5 m/s), with a consequent lower cooling capability. Furthermore, in the T-D configuration, the velocity is sensibly more homogeneous around ~ 6 m/s, leading to a more uniform HTC distribution, strictly related with the temperature distribution on the heated surface of the resonator.

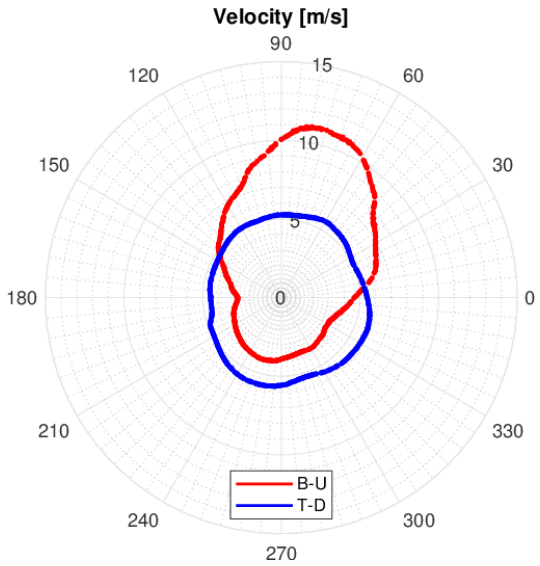

Figure 5.9: Comparison of the computed velocity on the centerline of the annular section (z ~ 0.25) in the B-U and T-D configurations.

The temperature profile computed in the T-D configurations of the annular cavity is shown in Figure 5.10: the temperature variation observed in the region of the temperature peak is considerably reduced in the T-D configuration with respect to the B-U configuration (from ~50 °C to ~5 °C) thanks to the better mass flow rate distribution in this part of the circuit. The inversion of the inlet and outlet pipes moves the problem of the temperature non-uniformity in the upper part of the cavity (high z) in which the flow is less homogeneous due to the proximity of the upper pipe, corresponding to the coolant inlet in this case. The computed pressure drop in the T-D configuration in line with the pressure drop estimated for the B-U configuration (~0.7 bar).

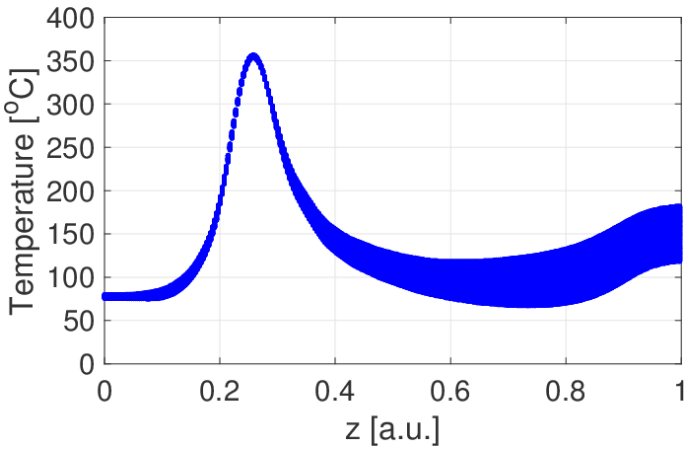

Figure 5.10: Temperature profile on the resonator heated surface with T-D annular cooling configuration.

The polar plot of the temperatures computed on the heated surface of the resonator close to the temperature peak (z ~ 0.25) is shown in Figure 5.11 for the B-U and T-D cooling configurations, with the inlet pipe is located at 75° for first case and 285° for the latter. The more homogeneous temperature profile on the heated surface close to the heat flux peak, obtained by the variation of the coolant direction, may be taken into account for the development of the future cavities cooling circuit.

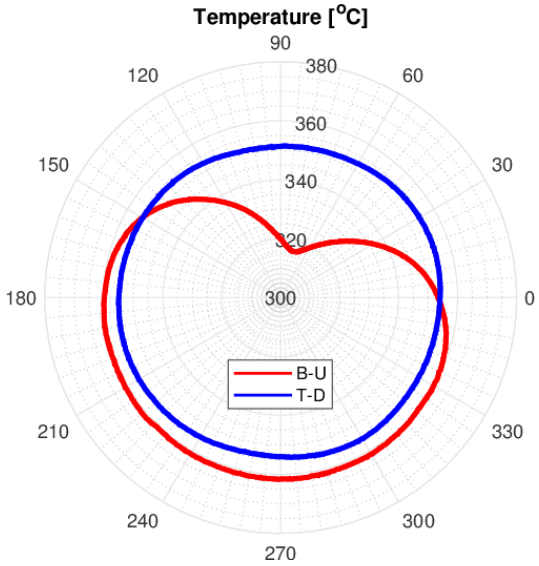

Figure 5.11: Polar temperature distribution in correspondence with the flat region of the resonator heated surface (z ~ 0.25) of the annular cavity in the B-U (red) and the T-D (blue) cooling configurations.

The temperature maps of the annular cavity resonator in the T-D configuration are shown in Figure 5.12 on a longitudinal and on an orthogonal cross section to the axis of the cavity. As already shown in Figure 5.11, the temperature homogeneity near the temperature peak is excellent, if compared to the B-U configuration. The issue of the temperature non-uniformity is moved on the top part of the cavity due to the proximity of the inlet pipe in the T-D cooling configuration.

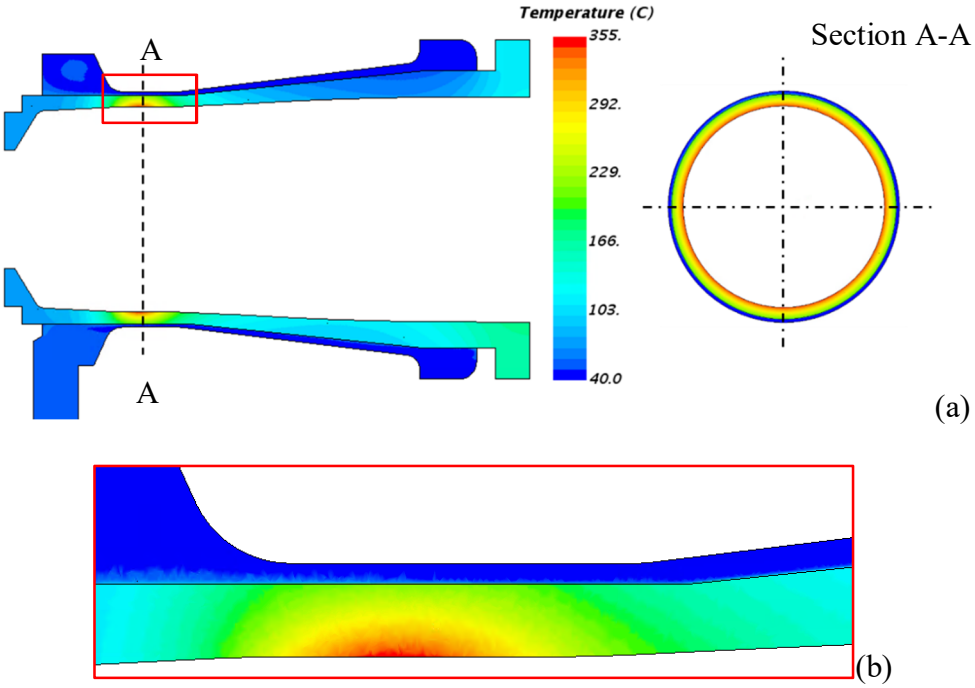

Figure 5.12: Temperature maps of the annular cavity resonator in the T-D configuration on a longitudinal cross section in correspondence with the outlet pipe and on an orthogonal cross section (A-A), located in correspondence with the temperature peak (a) and zoom in the mid-section region of the resonator (b).

The second optimized option proposed for the coaxial cavity considers additional inlet and outlet pipes in the cooling circuit of the resonator. This modification aims at improving the mass flow rate repartition on the overall cooling structure. In this case, the cooling circuit of the cavity needs a consistent modification of the water system of the gyrotron and, for this reason, requires a feasibility study to assess the effects that this modification may have on the other systems. Four inlet (blue) and four outlet (red) pipes distributed in staggered position are applied on the cavity to replace the single inlet and single outlet pipes of the nominal geometry (see Figure 5.13). To be consistent with the previous results, the nominal (B-U) coolant flow configuration is used in the following simulations.

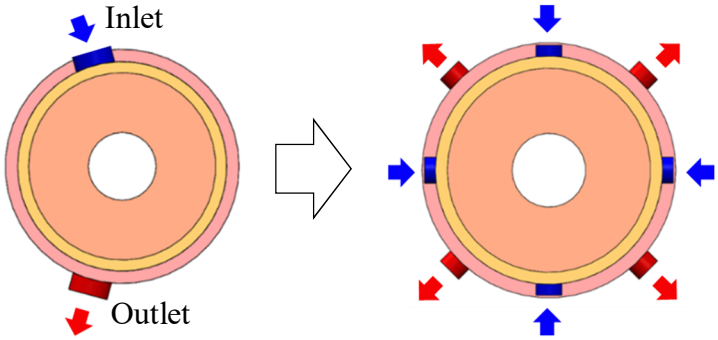

Figure 5.13: Optimization of the inlet and outlet pipes in the cavity.

The temperature profile of the annular cavity with four inlets and four outlets (4 I/O pipes) is shown in Figure 5.14: as expected, the temperature distribution computed on the heated surface of the resonator is quite homogeneous due to a better azimuthal repartition of the mass flow rate in the mid-section region that is obtained using the multiple piping system. In addition, the computed temperature distribution is homogeneous in the full length of the resonator, overcoming the issue observed with the T-D cooling configuration with single pipe. Moreover, the pressure drop is also reduced to ~0.4 bar due to the lower velocity in the inlet and outlet pipes.

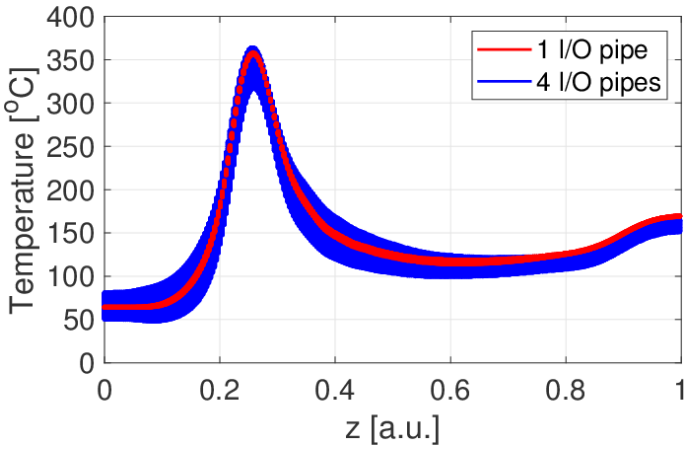

Figure 5.14: Comparison between temperature profiles on the heated surface of the annular cavity in the case of single I/O pipe (blue) and with four I/O pipes (red), respectively, in the case of B-U configuration.

The temperature map in the annular resonator is shown in Figure 5.16 when the multiple piping system is considered. In such configuration, the simulation takes advantages of the symmetry that allows to reduce the computational domain to 1/8,

see Figure 5.15. As already shown in Figure 5.14, the temperature distribution is more homogeneous than in the nominal single piping system with B-U cooling configuration always for the better mass flow rate repartition.

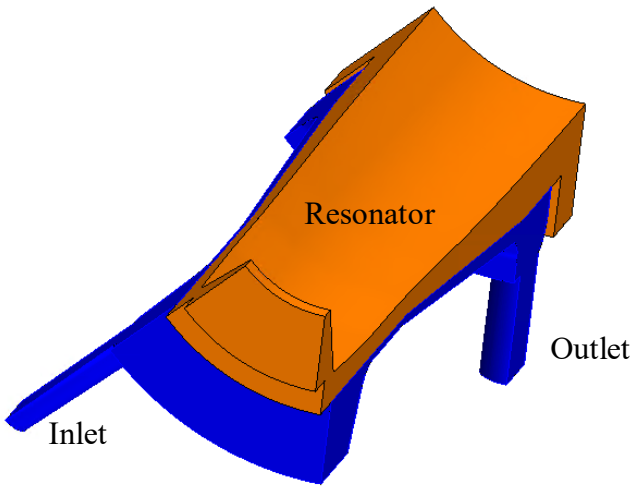

Figure 5.15: Computational domain for the annular cavity with 4 inlet/outlet pipes.

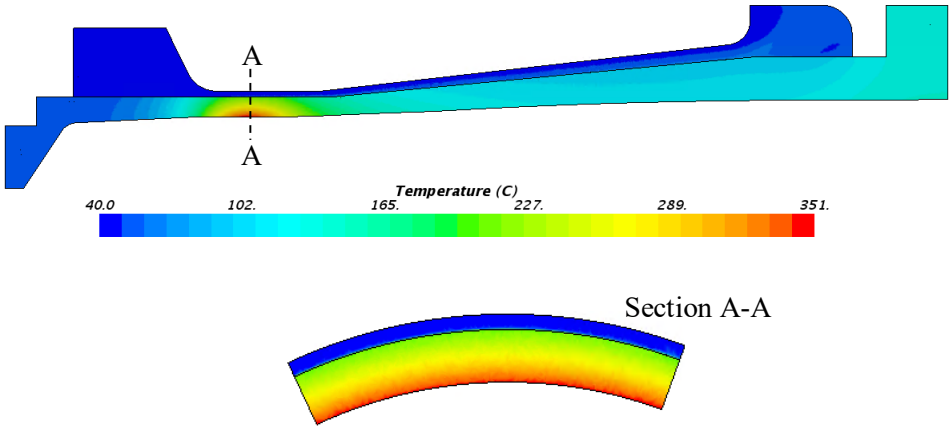

Figure 5.16: Temperature maps of the annular cavity resonator in the B-U configuration with 4 inlet/outlet pipes: longitudinal cross section in correspondence with the outlet pipe and cross section (A-A) orthogonal to the longitudinal axes, located in correspondence with the temperature peak.

5.1.3 Preliminary steady state simulations on the coaxial cavity equipped with Mini-Channels cooling geometry

A preliminary TH simulation of the steady state approach is also performed on the coaxial cavity for the 170 GHz, 2 MW gyrotron with resonator cooling circuit equipped with circular MCs, see Figure 5.17. The aim of this study is to estimate the improvements given by the presence of MCs on the temperature peak computed on the heated surface of the resonator. The geometry used for this simulation has been developed independently by KIT [46]. The design of the cavity with MCs is proposed in order to replace the annular cooling strategy relying on the very promising results obtained with the MCs configuration designed for the ITER gyrotron and compared with other possible alternatives involving the meander flow or the hypervapotron cooling concepts [19].

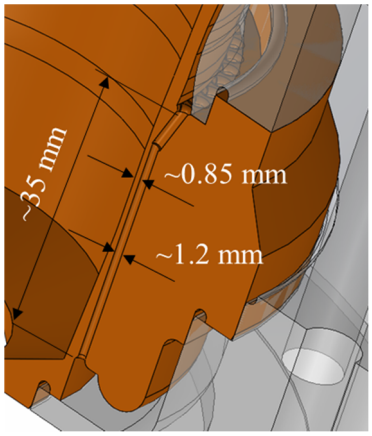

Figure 5.17: Zoom of the central region of the cavity equipped with mini-channels.

In the proposed geometry of the coaxial cavity equipped with MCs, the reduction of the resonator thickness between the heated surface and the coolant interface is expected to contribute to the global reduction of the temperature profile computed on the heated surface of the resonator with respect to the annular cooling configuration. Therefore, the maximum temperature reached cannot be directly compared for the two layouts. The boundary conditions and the heat load applied on the heated surface of the resonator are the same already used in the coaxial cavity with the annular cooling configuration.

Figure 5.18 shows the absolute pressure map computed on a cross section of one channel. The pressure drop computed between the inlet and the outlet pipe of the coaxial cavity equipped with MCs is ~3.3 bar, which is remarkably higher if

compared to the annular geometry with the same mass flow conditions (i.e. ~0.7 bar). In the whole cooling circuit of the cavity, the inlet section of the channels contributes heavily (~45 %) in the overall computed pressure drop, as show in the Figure 5.18.

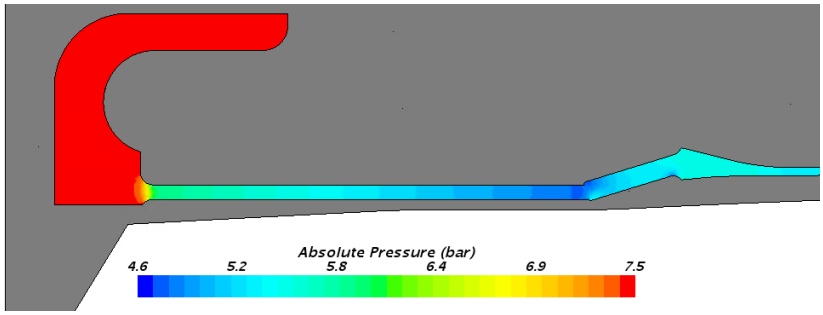

Figure 5.18: Absolute pressure map computed on a section of one mini-channel.

Figure 5.19 shows the temperature profile evaluated on the heated surface of the resonator with MC cooling configuration: the maximum temperature is ~210 °C and the temperature profile is quite homogeneous if compared to the annular configuration. The temperature non-uniformity is ~13°C and it is almost constant in the whole length of the resonator (see Figure 5.19).

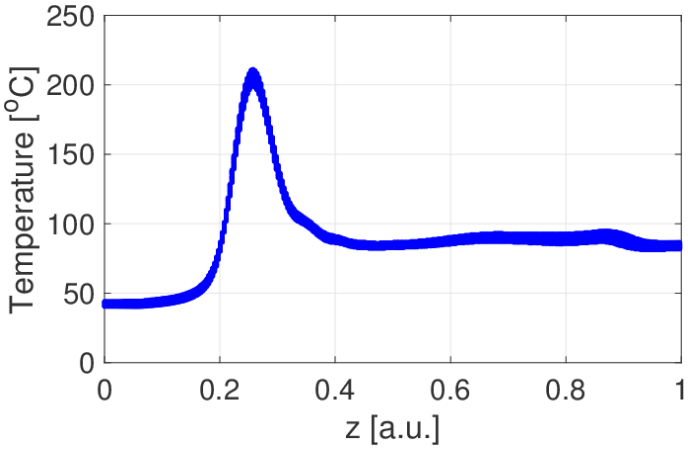

Figure 5.19: Temperature profile computed on the heated surface of the coaxial cavity equipped with mini-channels.

The temperature maps on the cross section on a longitudinal on an orthogonal (to the resonator axis) plane located in correspondence with the temperature peak (z ~ 0.25) are shown in Figure 5.20. In addition, Figure 5.21 shows the comparison between the temperatures on the heated surface of the cavity, close to the location of the temperature peak, for the coaxial cavity equipped with the annular cooling

design and with the MCs. The temperature distribution observed in the coaxial cavity equipped with MCs is considerably more homogeneous if compared to the annular cooling strategy due to a better coolant distribution. On the other side, the differences on the temperature between the two cavities are also due to the different thicknesses of the glidcop in the resonator region, and a direct comparison on the maximum temperature computed on the resonating surface cannot be performed.

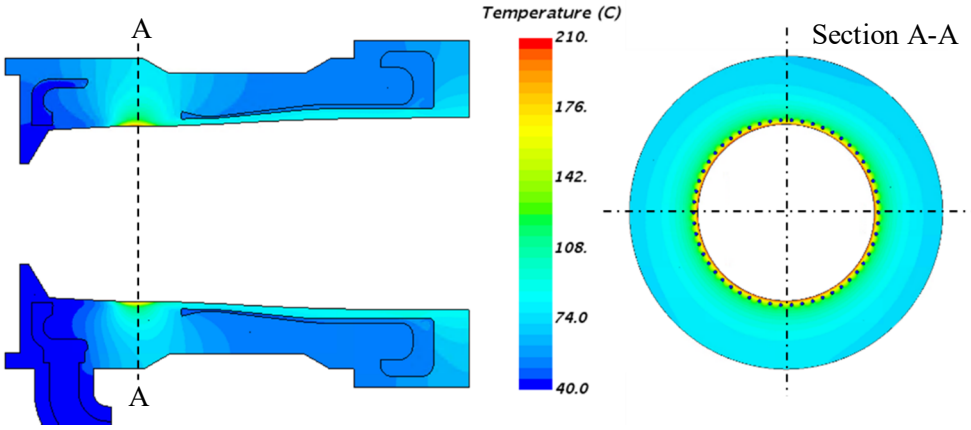

Figure 5.20: Temperature maps of the cavity resonator equipped with MCs computed on a longitudinal cross section in correspondence with the inlet pipe and on an orthogonal cross section (A-A), located in correspondence with the temperature peak.

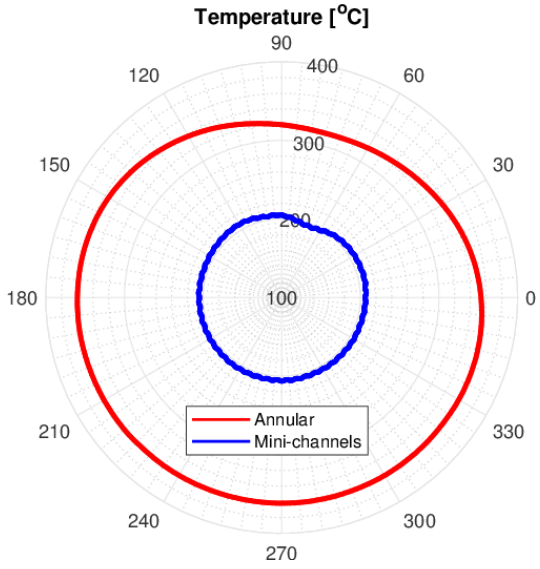

Figure 5.21: Comparison of the polar temperature distribution in correspondence with the flat region of the resonator heated surface (z ~ 0.25) computed for the annular cavity (red) and for the cavity equipped with MCs (blue).

5.2 The coaxial insert

The complete structure of the coaxial insert (in purple) is shown with the external surface of the cavity (in green) in Figure 5.22. The coaxial insert is a long component (total length of ~1.5 m) made of copper, which starts from the base of the gyrotron and crosses entirely the cavity region, see Figure 1.13. Here, only the portion of the cavity which is placed inside the cavity is modelled to reduce the computational cost. The external surface of a portion of the insert located inside the cavity is covered by corrugations (see Figure 5.22), which are removed in the simulations in order to be consistent with the 2D approach used in the code EURIDICE® [36].

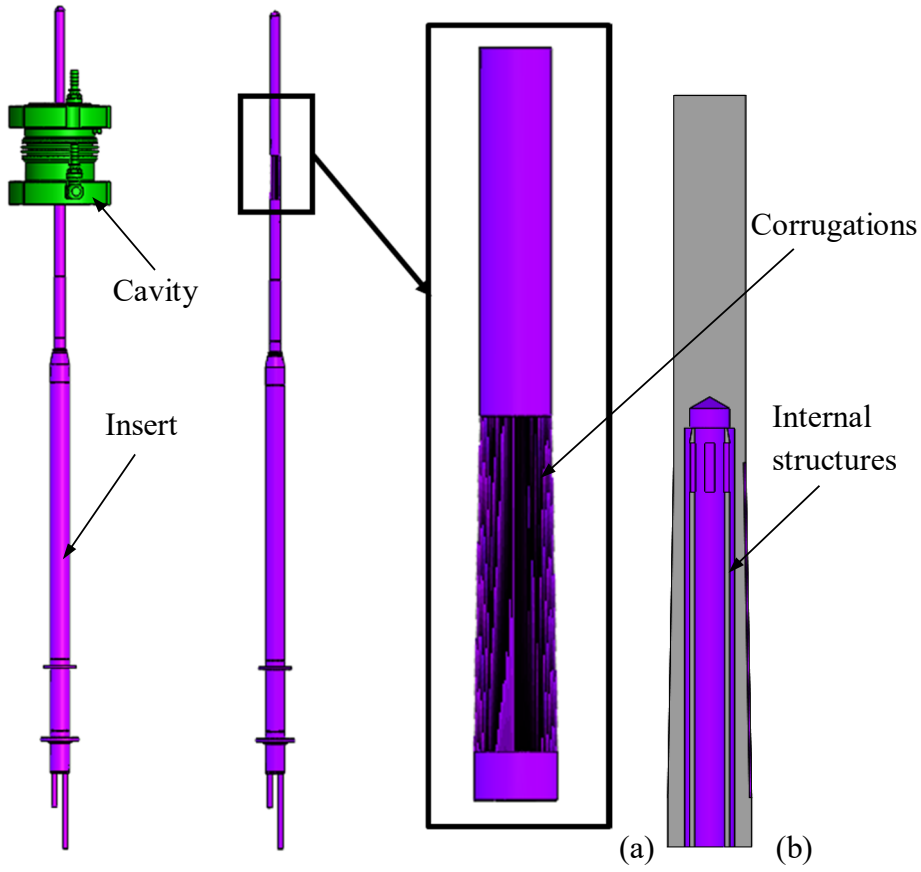

Figure 5.22: CAD model of the coaxial insert: (a) simplification procedure for the definition of the coaxial insert geometry used in the model and (b) cross section of the coaxial insert used in the model.

The longitudinal cross section of the coaxial insert is shown in Figure 5.22b, in which the internal structures of the component are visible. The radial profile of the external surface of the coaxial insert, which is the resonating heated surface of this

component, and the heat load applied at the initial iteration of the MUCCA tool are shown in Figure 5.23. As performed with the simulation of the resonator, the initial heat load is computed by the code EURIDICE® taking into account the nominal undeformed resonating profile of the coaxial insert.

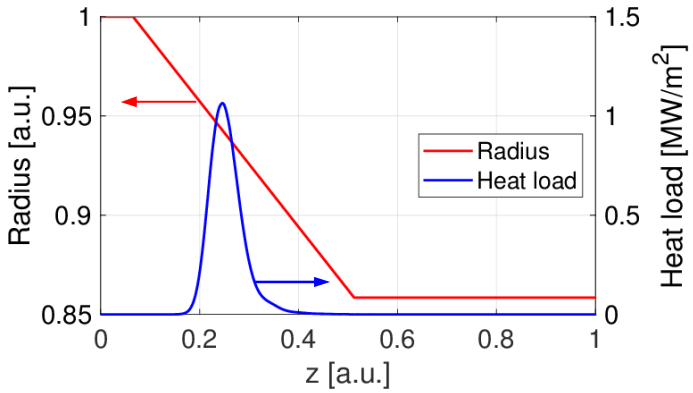

Figure 5.23: Initial heat loads (blue) and heated surface profile of the coaxial insert (red) applied at the initial stage of the simulation.

The cooling circuit of the coaxial insert is obtained in the free space between the external and the internal solid structures of the insert. The fluid moves from the bottom part of the insert in a circular pipe toward the upper part of the cooling circuit of the insert that is located inside the cavity region. In the upper region, four rectangular-shaped holes allow the fluid to move in the external annular region obtained from the external surface of the inner solid structure and the internal surface of the external solid structure which constitutes the insert. In the external annular channel, the coolant moves from the top part of the component to the bottom, where the outlet pipe of the cooling circuit is located. The computational domain used in the simulation of the coaxial insert is shown in Figure 5.24, where the relevant components of the structure are clearly displayed with different colours. Thanks to the symmetry of the component, only ¼ of the insert domain is modelled in the simulations.

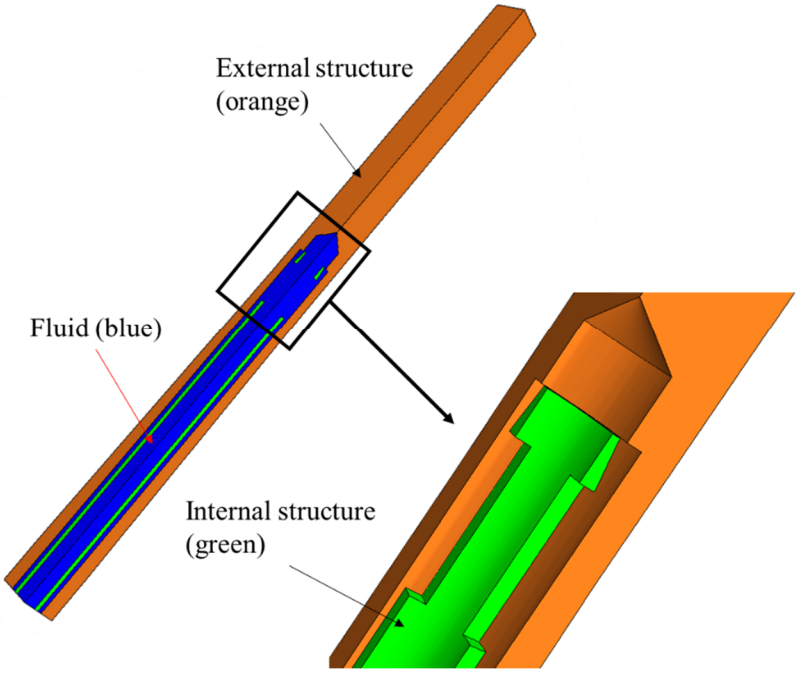

Figure 5.24: Computational domain of the coaxial insert.

Concerning the cooling circuit of the insert, the inlet and the outlet sections are locate in the bottom region of the component, far from the cavity region. The fluid at the inlet has the same characteristics of the coolant at the inlet section of the resonator cooling circuit (i.e. absolute pressure of 8 bar and temperature of 40 °C). In order to evaluate correctly the properties of the coolant on the inlet section of the simulated domain, a steady state CFD simulation with empirical pressure drop correlations is performed on the lower part of the coaxial insert (see Appendix F), considering an insert inlet mass flow rate of 0.6 m^3/h [36].

5.2.1 Preliminary steady state simulation on the coaxial insert

As performed with the resonator of the coaxial cavity, a set of preliminary simulations is performed on the insert of the gyrotron in order to assess the thermal and mechanical behavior of this component. The steady state temperature map and profiles computed on the heated surface of the coaxial insert are shown in Figure 5.25, while the heat flux applied on the heated surface of the insert is shown in Figure 5.23. Also in this case, the temperature profile computed on the heated surface of the resonator is not azimuthally averaged in order to observe the temperature non-uniformity.

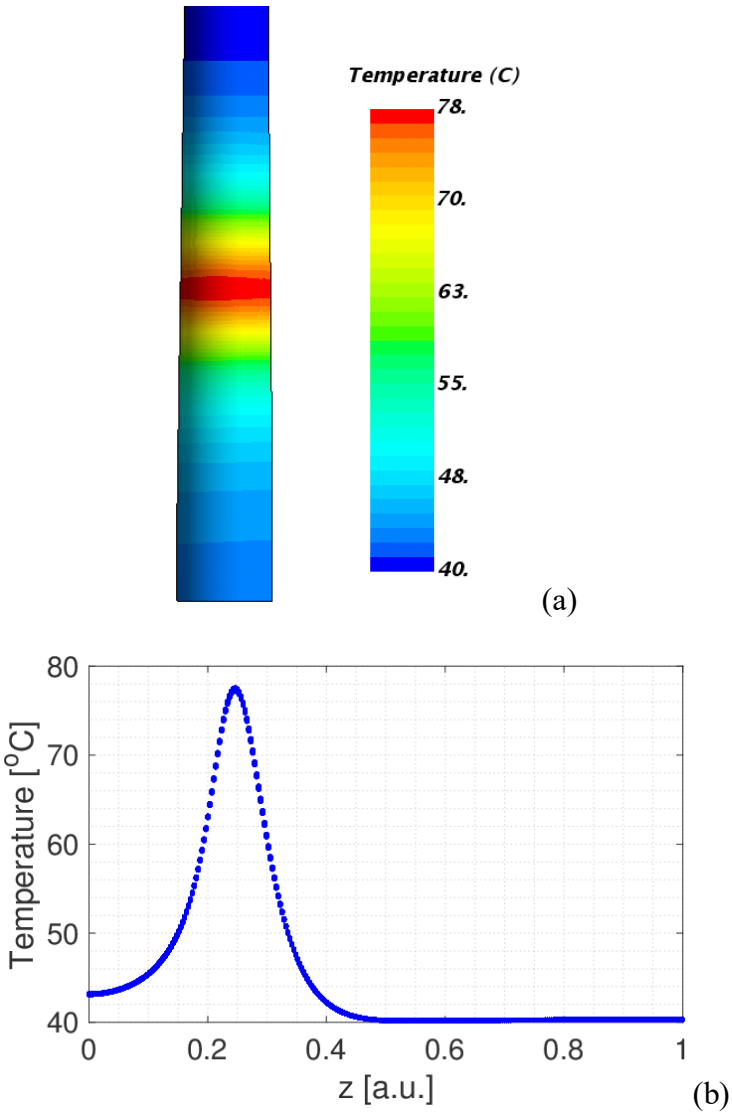

Figure 5.25: Computed temperature (a) map and (b) profile on the heated surface of the coaxial insert.

The maximum temperature computed on the heated surface of the insert is ~78 °C, located on the position of the heat load peak (see Figure 5.25). The temperature map on a symmetry plane of the coaxial insert and on a cross section orthogonal to the longitudinal axis, located in correspondence with the temperature peak are shown in Figure 5.26. The temperature distribution in the external region of the insert is perfectly homogeneous, thanks to the geometry symmetry of the coaxial insert and of the design of the cooling circuit. The azimuthal temperature difference on the peak region is < 0.5 °C (see Figure 5.25b) and the fluid boiling is not observed due to the low temperature reached in the solid-fluid interfaces (< 70 °C).

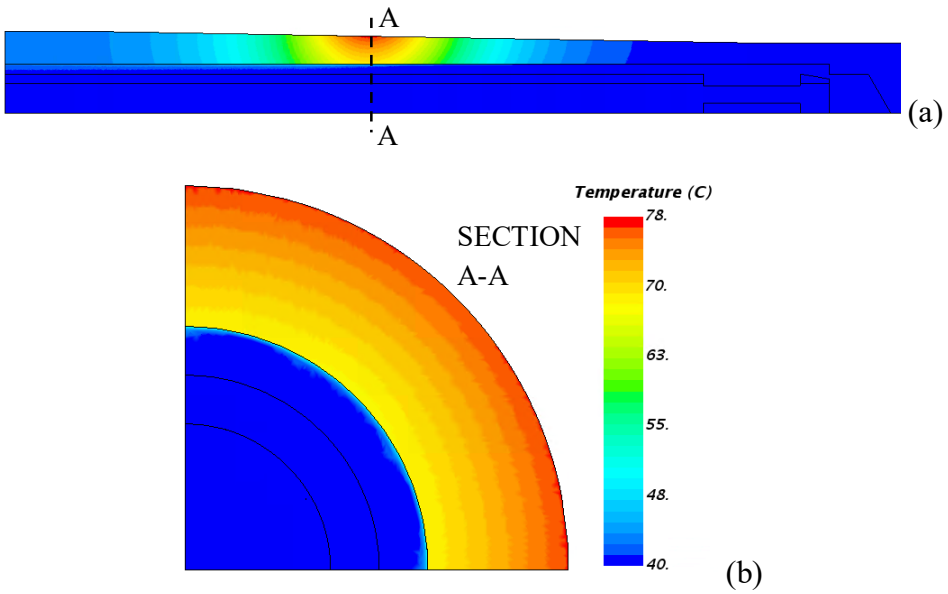

Figure 5.26: Computed (a) temperature map on a symmetry plane of the coaxial insert and (b) temperature map on a cross section orthogonal to the longitudinal axes, located at the temperature peak.

Concerning the mechanical behavior, the axial and the radial displacements computed on the heated surface of the coaxial insert are shown in Figure 5.27. The lower part of the insert ($z = 0$) is fixed, and the upper region is free to expand, as defined by the TM boundary conditions. The magnitude of heat load applied on the heated surface of the insert leads a temperature distribution that produces deformations which are approximatively one order of magnitude smaller when compared to the deformation of the heated surface of the resonator (see Figure 5.7). Thus, the general evolution of the cavity is expected to be determined mainly by the deformations computed in the resonator.

The temperature map of the solid region of the coaxial insert and the velocity field of the coolant in the top region of the component are shown in Figure 5.28. The flow field in the upper region shows the effects of the rectangular holes in the variation of the flow direction. A set of simulations with the same boundary condition has been also performed with the realizable two-layer, k-ε turbulence model [34] showing negligible differences on the overall computed results in terms of pressure drop, maximum temperature of the solid structure and fluid path on the top region of the insert. Finally, the computed pressure drop between the inlet and the outlet section of the coolant circuit of the coaxial insert is ~0.4 bar.

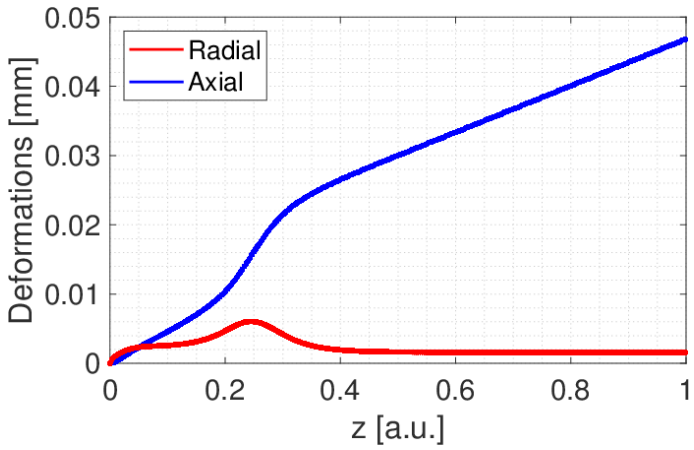

Figure 5.27: Axial (blue) and radial (red) displacements of the heated surface computed for the coaxial insert.

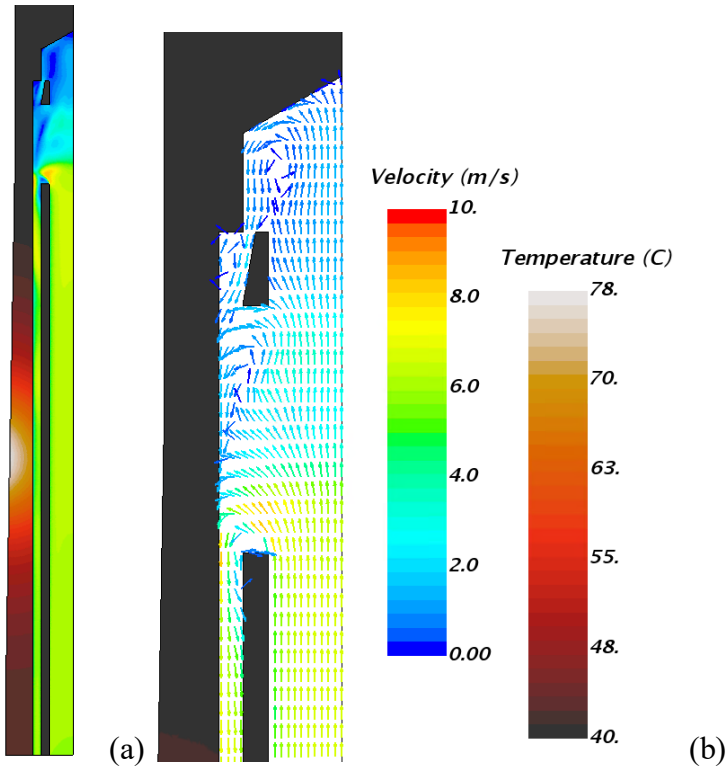

Figure 5.28: Computed (a) map of coolant velocity and solid temperature on the coaxial insert and (b) flow field on the upper region of the coolant domain of the coaxial insert.

5.3 Simulation of the evolution of the working condition of the 170 GHz, 2 MW coaxial cavity

In this paragraph, the results of the MUCCA tool applied on the annular coaxial cavity equipped with annular cooling configuration are discussed. The aim of this study is to compute the evolution of the average temperature profiles (see Figure 5.29), of the heat loads (see Figure 5.30), and of the average radial profiles (see Figure 5.31) on the heated surfaces of the resonator and of the coaxial insert.

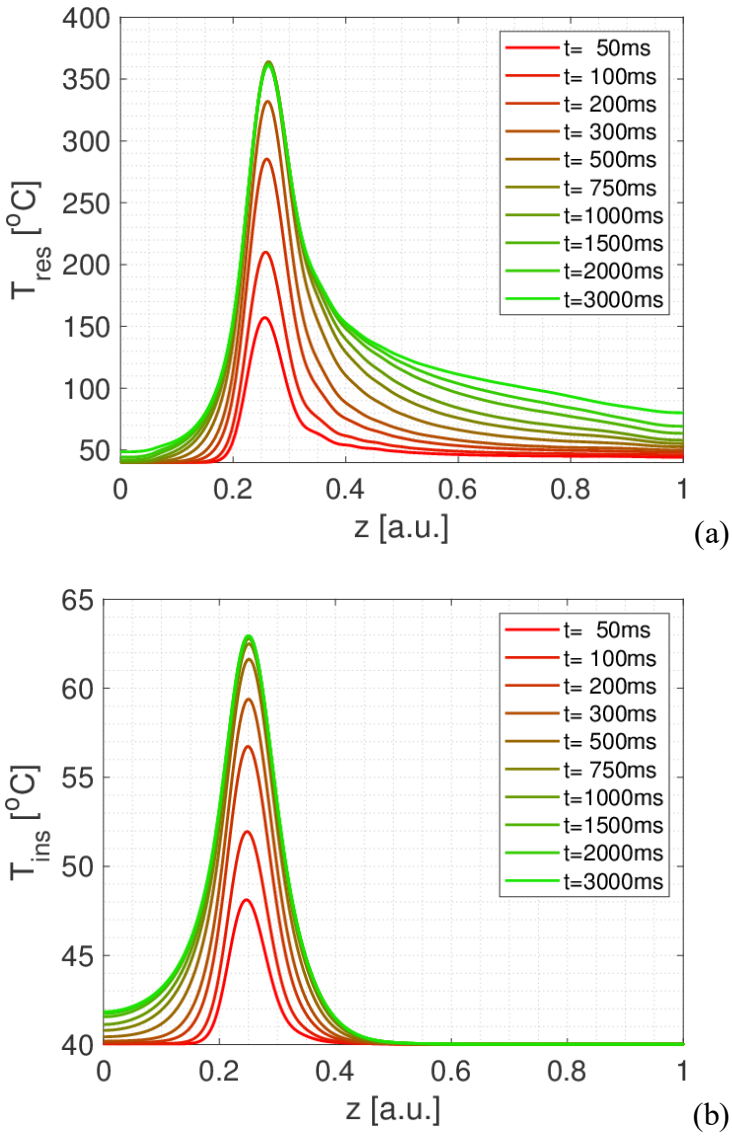

Figure 5.29: Evolution of the temperature profiles on the heated surface of the resonator (a) and of the coaxial insert (b), respectively.

The temperature profiles computed on the heated surfaces of the resonator (Figure 5.29a) and of the insert (Figure 5.29b) qualitatively follow two different evolutions. The first difference is observed on the time at which the peak temperature is reached, namely ~500 ms in the resonator and ~750 ms in the insert. This difference is due to the different cooling of the two components and the different thicknesses of the two structures, which are ~0.85 mm and ~3 mm for the resonator and the insert, respectively. In the upper region of the resonator (high z in Figure 5.29a) and in the lower region of the insert (low z in Figure 5.29b) the evolution of the temperature profiles toward the steady state condition is considerably longer with respect to the other regions of the components. For both components, the temperature profile on the entire length of the heated surface do not reach the stable conditions before 3 s of simulation.

Figure 5.30 shows the evolution of the heat load applied on the heated surface of the resonator (Figure 5.30a) and of the coaxial insert (Figure 5.30b). The legends report the time instants when the heat load is applied, and maintained constant up to the consecutive step (for clarity, not all the time intervals used in the simulation are reported in the figures below). The variation of the heat load in the resonator and in the coaxial insert is more relevant on the mid-section of the resonator, where the temperature (see Figure 5.29) and, consequently, the thermal deformation (see Figure 5.31) of the heated surface of the structures are more significant for the cavity behavior.

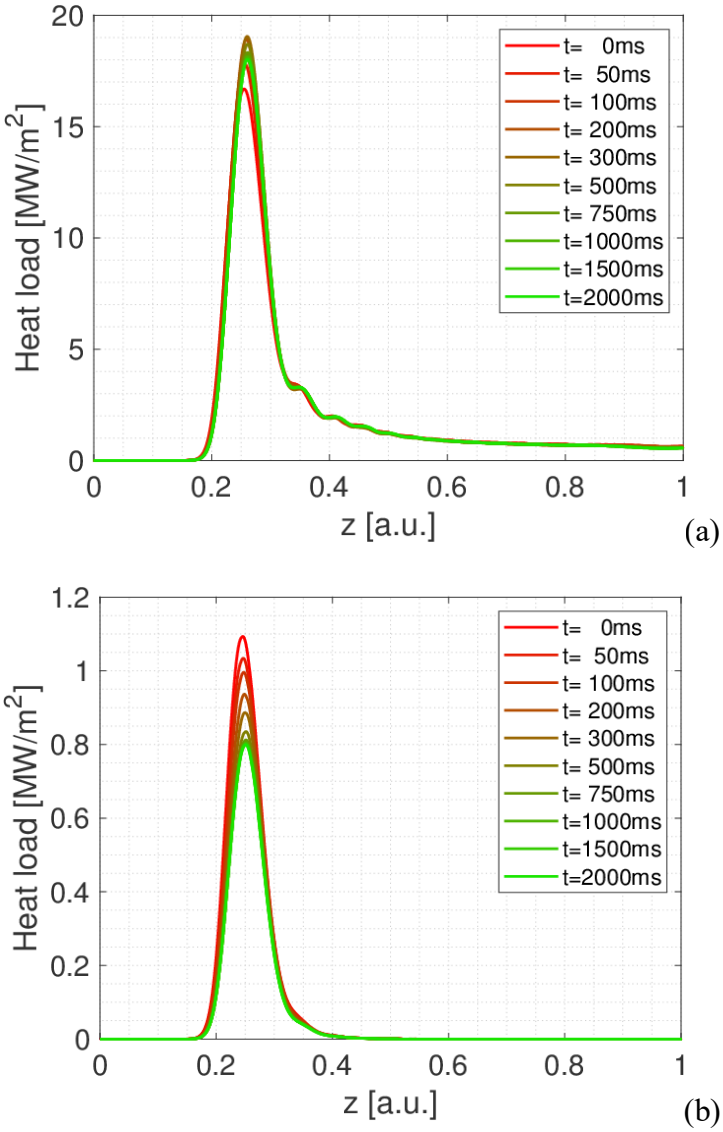

Figure 5.30: Evolution of the heat load profiles on the heated surface of the resonator (a) and of the coaxial insert (b), respectively.

The average profile of the deformation computed on the heated surface of the resonator and the zoom in the mid-section region are shown in Figure 5.31, in which the black dashed line represents the initial cold profile. The variation of the profile of the eternal surface of the coaxial insert is negligible (~ one order of magnitude lower) with respect to the deformation of the resonator and it is not reported here.

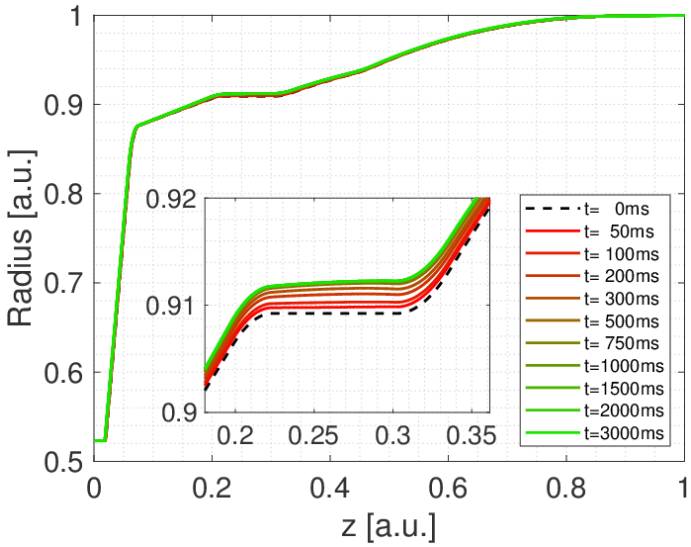

Figure 5.31: Evolution of the deformed profile of the critical region of the resonator heated surface.

The temperature maps on a cross sections of the resonator and on a symmetry plane of the coaxial insert computed at t = 3 s are shown in Figure 5.32. As already observed in Figure 5.29, the temperature peak is localized in the region of the mid-section of the resonator where the heat load is higher.

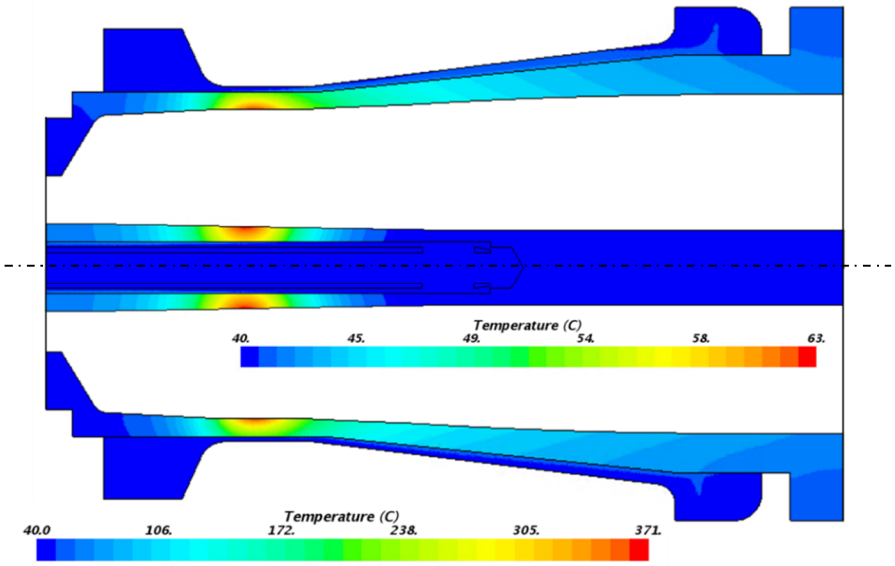

Figure 5.32: Temperature map on a longitudinal cross section of the resonator and of the coaxial insert at t = 3 s. The cross section of the insert has been duplicated and located inside the resonator structure. The internal legend refers to the coaxial insert only; the external legend refers to the resonator structure only.

The evolutions of the temperature and heat load peaks on both resonator and coaxial insert are shown in Figure 5.33 and Figure 5.34, respectively. Figure 5.33b shows that the temperature peak in the resonator remains below ~250 °C in the first 150 ms of operation. Given that the Glidcop® temperature of 250 °C is the safe limit for the gyrotron operations [36], this result indicates that a pulse length of up to 150 ms can be achieved with the existing cooling configuration. In order to improve the pulse duration of the gyrotron, the definition of a better cooling strategy is required.

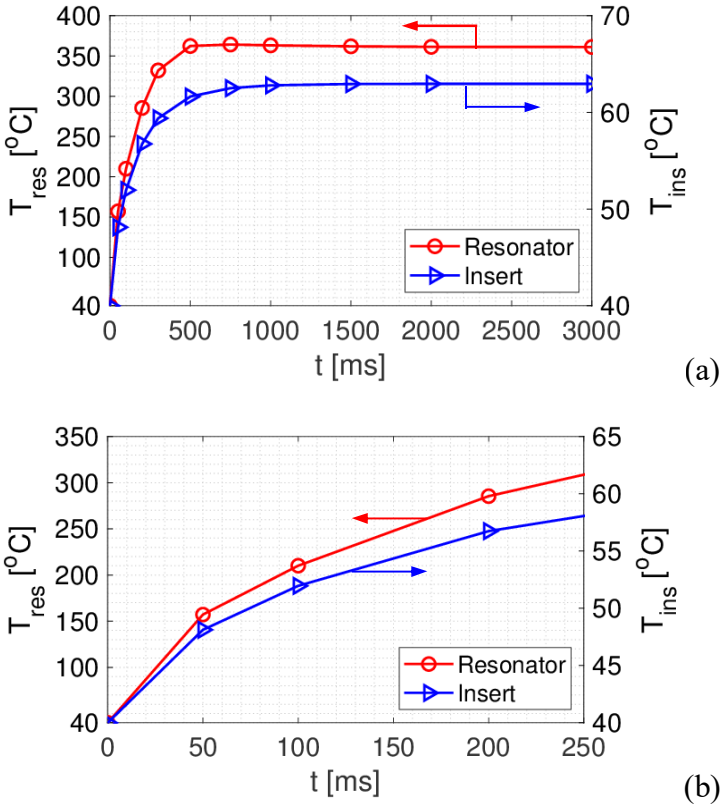

Figure 5.33: Maximum temperature evolution on the resonator and insert heated surface (a) and zoom on the first 250 ms (b).

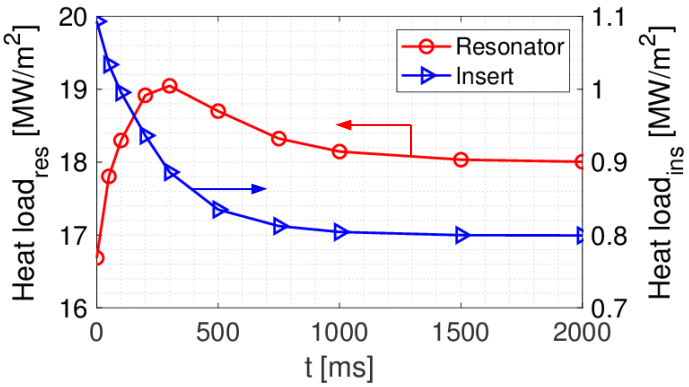

Figure 5.34: Evolution of the computed peak value of the heat loads.

The variation of the maximum value of the heat load is not negligible, in particular as far as the coaxial insert is concerned, when the peak is reduced by ~30 % with the respect the initial condition. Since the point where the electromagnetic field is maximum, this variation occurs at an approximately fixed distance from the resonator wall. Since the radial expansion of the resonator is one order of magnitude larger than the radial expansion of the insert, the location of the maximum field is moving away from the insert during the transient phase mainly caused by the conical shape of the heated surface of the insert. This behavior results in a reduction of the heat load evaluated on the heated surface of the insert [36].

5.4 Summary

This chapter describes the application of the MUCCA tool on the coaxial cavity for the 2 MW gyrotron, which is under development at KIT for the DEMO reactor. The model involves the cavity resonator equipped with annular cooling concept and the coaxial insert. The transient evolution of the cavity has been monitored in order to determine the duration of the pulse in safety conditions for the components of the cavity (the maximal temperature of the resonating surface of the cavity is limited to 250 °C). In the relevant conditions for the gyrotron operations, the computed results show that the maximum temperature value is reached after ~150 ms, pointing out the limits of the annular cooling concept to adequately cool the cavity during long pulse operations. The cooling behaviour of the coaxial cavity has been improved by using a resonator geometry equipped with MCs, proposed independently by KIT. In this case, steady-state simulation has been performed on the resonator of the cavity only. The results show that the maximum allowed temperature of 250 °C has not reached in the resonator heated surface, allowing to increase the pulse operation up to the theoretical steady state condition of the gyrotron.

Chapter 6

Conclusion and perspective

The MUlti-physics tool for the integrated simulation of the Cavity (MUCCA) tool, developed since 2016 during my PhD activity, has been presented here, describing the models developed and the relevant results obtained in the study of the gyrotron cavities for the Electron Cyclotron (EC) system for ITER and DEMO fusion reactors. The MUCCA tool defines an innovative approach on the multiphysics simulation of the gyrotron cavity combining Thermal-Hydraulic (TH), Thermo-Mechanical (TM), and Electro-Dynamic (ED) simulations in a self-consistent iterative procedure used to characterize the behaviour of the component and to predict the cavity performances during gyrotron operations.

The validation of the MUCCA tool has been performed on the cavity of the 170 GHz, 1 MW ITER gyrotron equipped with Raschig Ring (RRs) using the available results of the experimental campaign performed by Karlsruhe Institute of Technology (KIT) in 2016. The results are very promising, showing that the dependency of the waves frequency down-shift observed inside the gyrotron during the operation, as a function of the power losses in the cavity, is well reproduced by the tool. Based on the experimental results, an analytical model is developed. Such model is used to couple the frequency shift with the deformation computed on the resonating surface and the heat load, defining “a priori” the setup for of the simulations, i.e. the thermal conductivity of the RRs region in the MUCCA tool.

On the 170 GHz, 1 MW gyrotron cavity layout, the MUCCA tool is applied for the analysis and the development of the Mini-Channels (MCs) cooling system, which is proposed as the best alternative to the RRs for the ITER gyrotrons cavity.

A set of simulations has been performed to characterize the overall behaviour of the cavity in terms of coolant pressure drop, temperature and deformation profiles computed on the heated surface of the resonator as a function of the channels dimension and coolant mass flow rate. The analytical procedure developed for the cavity equipped with RRs is applied here to predict the behaviour of the cavity deformation as a function of the average Reynolds number of the coolant inside the channels. Currently, a significant experimental campaign on a fully-relevant gyrotron cavity equipped with MCs has not been performed yet and the MUCCA tool cannot be completely validated with the channels cooling configuration. The experimental results on the planar mock-up of the cavity, tested in 2016 by Areva, show very good agreement with the thermal results computed with the MUCCA tool. The suggestions coming from the simulations performed with the cavity equipped with MCs have not be considered for ITER gyrotron, since the RRs cooling strategy was chosen before the development of this activity and because of the preliminary stage of the MUCCA tool. Using as reference geometry the MCs layout applied on the ITER cavity design, Thales Electron Devices (manufacturer of the European gyrotrons) scheduled for 2019 – 2020 a relevant test campaign on a fully-relevant cavity mock-up aiming at characterizing the thermal and mechanical behaviour of this component, adopting an innovative manufacturing procedure for the relevant part of the resonator. The tests will be also used to verify the manufacturing procedure proposed for the construction of the cavity and to obtain a relevant set of measurements for the validation of the model developed in the MUCCA tool. In this direction, the MUCCA tool can be considered an important tool to support the design process of the cavity, which allows to simulate easily lots of cooling alternatives and working conditions of the gyrotron.

The procedure adopted in the simulation of the ITER gyrotron cavities has been applied to a more complex resonating structure as shown in the transient assessment of the coaxial cavity for the 170 GHz, 2 MW gyrotron for DEMO EC system, developed by Karlsruhe Institute of Technology (KIT) with annular cooling strategy. In the cavity region of this gyrotron there are two resonating components: the resonator and the coaxial insert, the latter used to improve the overall performance in terms of power associated to the RF waves. The procedures adopted in the MUCCA tool are applied separately for the two components in the TH simulations. The interaction between the resonator and the insert are considered in the TM and the ED simulations, in which the two components are coupled by means of suitable boundary conditions. The transient analysis performed with the MUCCA tool shows that steady state operation of the two components is not reached in the first 3 s of the

pulse. In addition, the transient evolution of the different parts of the two components follows different time scales, which can significantly affect the global behaviour of the cavity. In the case of the coaxial gyrotrons, relevant results from experimental campaigns are not available at the moment, even though a test campaign is planned at KIT on a coaxial cavity prototype with the annular cooling strategy. In the relevant conditions for the gyrotron operations, the computed results show that the temperature limit of 250 °C (set to define the safe condition for the gyrotron) is reached on the heated surface of the resonator after ~150 ms, pointing out the limits of the annular cooling concept to adequately cool the cavity during long pulse operations. The cooling behaviour of the coaxial cavity is considerably improved, with respect to the annular design, by using a resonator geometry equipped with MCs. In this case, the enhanced cooling allows to increase the pulse operation up to the theoretical steady state without reaching the temperature 250 °C with the same boundary condition imposed. The results of the test campaign planned by Thales Electron Devices will be useful for the thermal improvement of the coaxial cavity.

At the present state, the lack of available experimental results is one of the weak point of the MUCCA tool. In fact the validation of the full MUCCA tool with different resonator cooling concepts, is not possible at this stage of the work. However, experimental campaigns on RRs gyrotron are presently ongoing at Swiss Plasma Centre of Lausanne and the tests on MCs cooling strategy are planned in the next future.

As far as the improvement of the features of the MUCCA is concerned, the forthcoming efforts are focused on the optimization of the interactions between the TH-TM-ED models, now implemented with separate computational tools in a soft-coupling fashion. In this way, the optimization of the MUCCA tool can reduce significantly the time spent to complete the iterative process, reducing the external human actions in the management of the simulations. The final goal in the software optimization is focusing in developing a single code that includes the three modules in a self-sustained computational environment. This should improve the flexibility of the MUCCA tool for the application on different cavity designs and it should ease simulations. With this things done the code could be used efficiently in design and research activities for the development of future gyrotrons' cavities.

Appendix A

Material properties

In this appendix, the equation used to define the thermal and mechanical properties of the Glidcop® [30] and of the copper [29] used in the simulations of the gyrotron cavities and of the mock-ups are presented.

Glidcop® density

The density of the Glidcop®, expressed in kg/m^3, is described by (28) as a function of the temperature, expressed in Celsius degree.

$$\rho = 8872.0 - 0.45628 \cdot T - 8.7038 \cdot 10^{-5} \cdot T^2 \tag{28}$$

Glidcop® specific heat

The specific heat of the Glidcop®, expressed in J/kg K, is described by (29) as a function of the temperature, expressed in Celsius degree.

$$cp = 383.4 + 0.1413 \cdot T - 2.9794 \cdot 10^{-5} \cdot T^2 \tag{29}$$

Glidcop® thermal conductivity

The thermal conductivity of the Glidcop®, expressed in W/m K, is described by (30) as a function of the temperature, expressed in Celsius degree.

$$k = 368.23 - 0.2612 \cdot T + 3.07 \cdot 10^{-4} \cdot T^2 \quad (30)$$

Glidcop® thermal expansion coefficient

The thermal expansion coefficient of the Glidcop®, expressed in 10^{-6}/K, is described by (31) as a function of the temperature, expressed in Celsius degree.

$$\alpha = 16.0773 + 8.371 \cdot 10^{-3} \cdot T - 3.4349 \cdot 10^{-6} \cdot T^2 \quad (31)$$

Glidcop® and copper Young modulus

The Young modulus of the Glidcop® and of the copper, expressed in GPa, is described by (32) as a function of the temperature, expressed in Celsius degree.

$$E = 126.4176 - 3.7884 \cdot 10^{-2} \cdot T - 1.8237 \cdot 10^{-5} \cdot T^2 \quad (32)$$

Glidcop® and copper Poisson ratio

The Poisson ratio of the Glidcop® and the copper is considered constant in the simulations, equal to 0.34.

Copper density

The density of copper is considered as constant, equal to 8933 kg/m^3.

Copper specific heat

The specific heat of the copper, expressed in J/kg K, is described by (33) as a function of the temperature, expressed in Kelvin.

$$cp = 316.21 + 0.3177 \cdot T - 3.4936 \cdot 10^{-4} \cdot T^2 + 1.661 \cdot 10^{-7} \cdot T^3 \quad (33)$$

Copper thermal conductivity

The thermal conductivity of the copper, expressed in W/m K, is described by (34) as a function of the temperature, expressed in Kelvin.

$$k = 420.75 - 6.8493 \cdot 10^{-2} \cdot T \quad (34)$$

Copper thermal expansion coefficient

The thermal expansion coefficient of the copper, expressed in 10^{-6}/K, is described by (35) as a function of the temperature, expressed in Kelvin.

$$\alpha = 13.251 + 6.903 \cdot 10^{-3} \cdot T + 8.5306 \cdot 10^{-7} \cdot T^2 \quad (35)$$

Appendix B

Comparison of the results computed with the steady state and the transient approaches on the cavity equipped with Raschig Rings

During the initial part of the MUCCA tool development, a set of simulations on the gyrotron cavity equipped with RRs is performed using both the steady state and the transient approaches and applying the same initial boundary conditions (i.e. mass flow rate, heat load, coolant temperature and pressure) and simulations models. The aim of this analysis is computing the final operation condition of the cavity to verify if the two MUCCA tool approaches give the same result.

The following figures show the average temperature (Figure B.1) and the average radial profiles (Figure B.2) computed on the heated surface of the resonator of the cavity using the steady state (Figure B.1a and Figure B.2a) and the transient (Figure B.1b and Figure B.2) approaches of the MUCCA tool. As far as the steady state approach is concerned, the labels in the legend indicate the iteration of the MUCCA tool in which the result is computed.

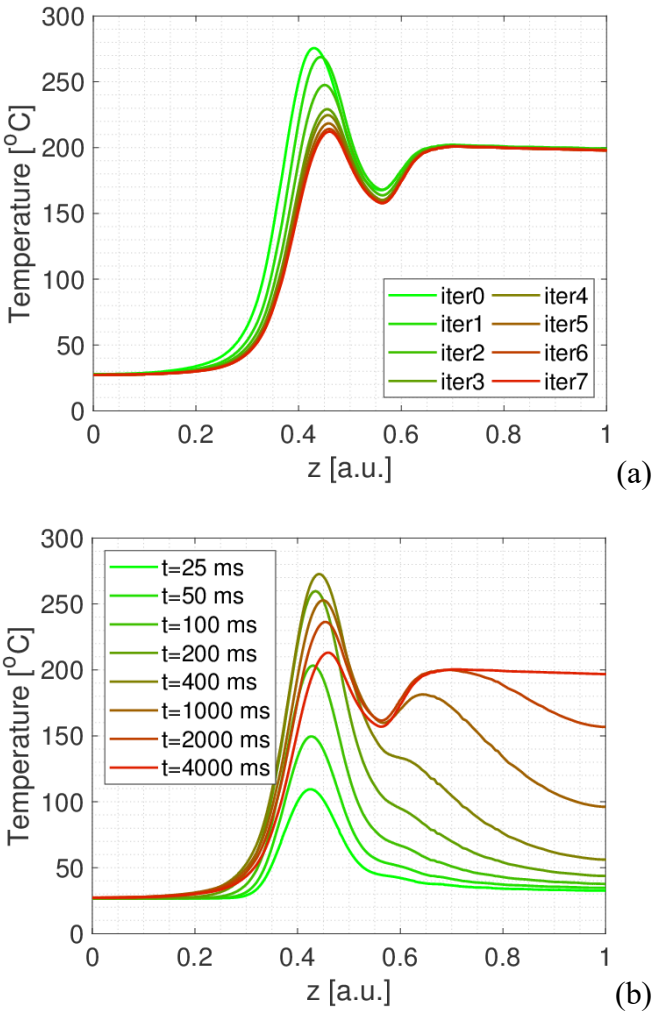

Figure B.1: Computed evolution of the average temperature profile of the heated surface of the resonator of the cavity equipped with RRs applying (a) the steady state and (b) the transient approach of the MUCCA tool.

The temperature behavior computed with the transient approach of the MUCCA tool is completely different if compared with the evolution computed with the steady state approach. In the steady state simulation approach the computed temperature profile tends to the final condition reducing progressively the resonator temperature peak. The same behavior is observed in the deformation profile computed on the resonating surface of the cavity (see Figure B.2a). In the simulation in which the transient approach is used, the steady state condition of the cavity is reached after ~4 s from the beginning of the transient. The temperature peak in the mid-section region of the resonator, reaches the maximum value of ~272 °C after

~500 ms. Hereafter, the peak is reducing progressively up to the end of the simulation in which it is stabilized at ~210 °C. A similar behavior is observed for the deformation of the mid-section region of the heated surface of the resonator, due to the direct correlation with the temperature field in the solid structure of the cavity (see Figure B.2b).

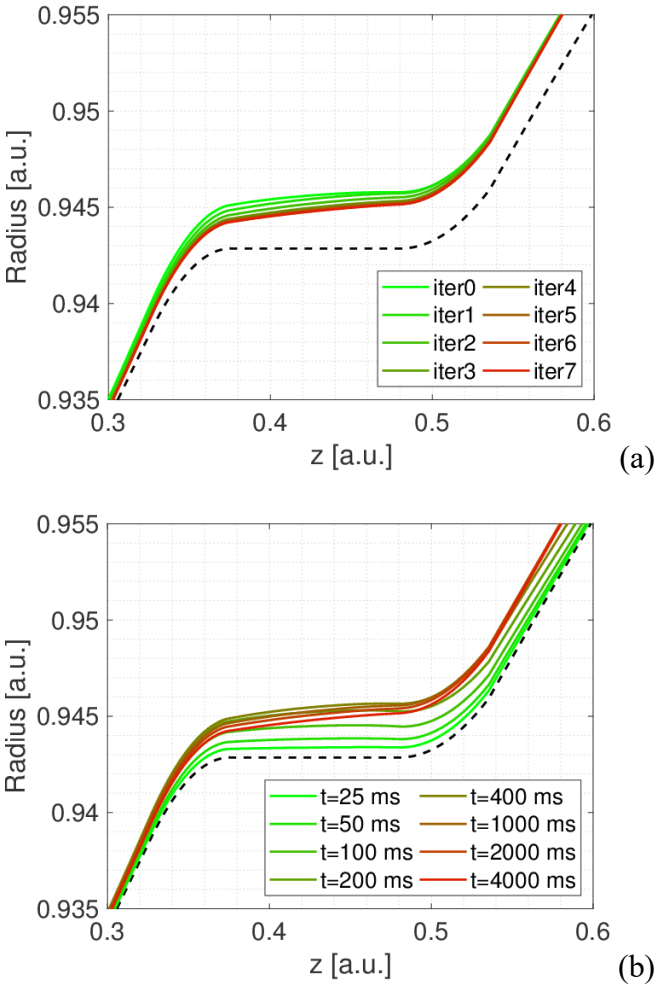

Figure B.2: Computed evolution of the radial profile of the heated surface of the resonator of the cavity equipped with RRs applying (a) the steady state and (b) the transient simulation approach of the MUCCA tool.

The results of the final stage of the two simulation approaches are very similar both in terms of average temperature and average deformation profiles. This results shows that the two approaches are mutually consistent for the evaluation of the final steady state condition of the cavity. The advantages of the steady state approach is the possibility to reduce considerably the number of iterations required to finalize the iterative procedure of the MUCCA tool (5 – 6 iterations are sufficient) with

respect to the transient approach. The disadvantages of this approach is the unphysical meaning of the intermediate iteration results for the description of the transient evolution of the cavity, which is relevant during the development of a new design of the cavity, as shown in the simulation performed for the study of the coaxial cavity for the 2 MW gyrotron (see Chapter 5). The transient approach needs approximatively three time more iterations of the MUCCA tool to reach a steady state cavity operation condition if compared to the steady state approach.

Appendix C

Description of the FE200 AREVA test facility

The experimental test facility FE200, localized at the AREVA NP Technical center of Le Creusot (France), is used to perform the two experimental test campaigns on the gyrotron mock-up equipped with RRs and MCs in 2015 and 2016, respcetively. The results of the test are used for the validation and the calibration of the simulations setup appliyed in the MUCCA tool. The two mock-ups are built to reproduce as better as possible the cooling behaviour of the cavity and they are tested in a scenario which is comparable to the gyrotron operation in terms of the maxium heat load applied on the heated surface of the components and of the water Reynolds number in the relevant region of the cooling domain.

The planar mock-up of the cavity (see Figure C.1) is located inside the vacuum chamber of the facility, which internal pressure is maintained at 10^{-5} mbar by vacuum pumps to limits the presence of impurities [31]. The mock-up is connected by the inlet and the outlet pipe with the primary hydraulic loop of the test facility (see Figure C.2) in which the water flow could be set between 0.6 kg/s (~36 l/min) and 6 kg/s (~360 l/min). The temperature of the coolant in the primary hydraulic loop can be controlled up to 230 °C and the pressure at the inlet section of the mock-up can be set between 6 bar and 33 bar [31].

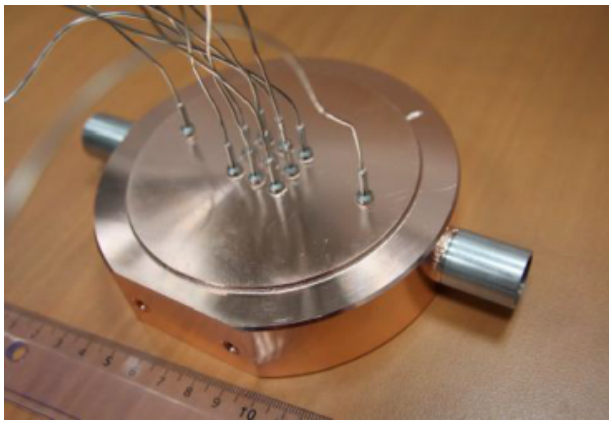

Figure C.1: Picture the mock-up tested in the FE200 test facility in 2016.

A secondary loop is placed entirely outside the vacuum chamber of the test facility used to cool-down the primary cooling circuit, to control the coolant temperature in the inlet section of the mock-up, and to perform the calorimetry evaluation on the primary circuit. The mass flow rate and the pressure of the primary coolant are monitored by mass flow and pressure meters located at the mock-up inlet section (see Figure C.2). In addition, two T-type thermocouples are located before and after the mock-up to perform the calorimetry evaluation directly on the primary coolant circuit (see Figure C.2).

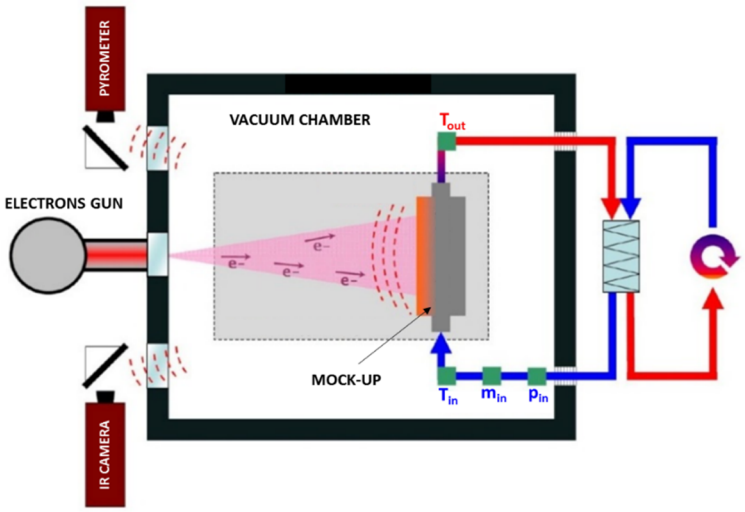

Figure C.2: Sketch of the FE200 test facility. The wall of the vacuum chamber (black line) together with the mock-up (dark grey), the electron beam (pink region) as well as the mock-up cooling primary and secondary circuits (red and blue arrows) are shown. Also the relevant diagnostics are shown in the effective position inside the cooling circuits of the mock-up (adapted from [31]).

The temperature measurement on the heated surface of the mock-ups is performed by a pyrometer pointed on the target region, which has been calibrated in the range 350 °C – 500 °C in the case of the 2015 test campaign for the RRs cooling tests, and in the range 265 °C – 455 °C in the case of the 2016 test campaign used for the MCs layout of the mock-up [31].

A set of thermocouples is used to measure the temperature inside the solid structure of the mock-up equipped with MCs[i]. In total, 11 K-type thermocouples are present (see Figure C.1): 2 thermocouples are present upstream and downstream the central region of the mock-up with measured spot located in the water stream. The remaining 9 thermocouples are located above the target region of the mock-up, in contact with the solid structure of the block placed above the target and with measuring point located at different height from the heated surface of the mock-up. The distance between the thermocouples and the height of the measurements spot with respect to the heated surface of the mock-up are shown in Figure C.3 and Table C.1, respectively. The error of the K-type thermocouples measurement is assumed to ± 1.5 °C [32]. No additional information on the other measurement devices are furnished during both test campaigns [31].

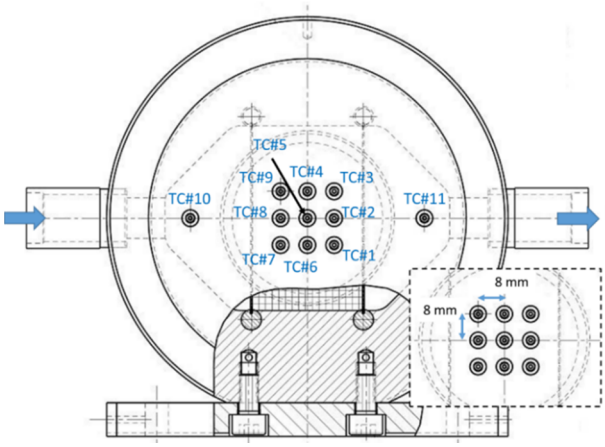

Figure C.3: Position of the thermocouples in the mock-up (the thermocouples are numbered from #1 to #11). The inset shows the zoom of the region where the 9 thermocouples are positioned, together with their relative distance. The main flow direction in the mock-up is also shown with the light blue arrows.

[i] Similar thermocouple layout is present in the mock-up with RRs used in the test campaign performed in 2015. The results obtained in the 2015 test campaign are not used for the validation due to the lack of information which are relevant for the correct understanding of the measurements.

Table C.1: Distance of the thermocouples from the heated target surface.

Label	Distance from heated surface
TC#1, TC#6, TC#7	4.75 mm
TC#2, TC#5, TC#8	5.75 mm
TC#3, TC#4, TC#9	7.75 mm

The CAD model of the mock-up equipped with MCs used in the 2016 test campaign is shown in Figure C.4. The mock-up is installed in a flat basement allowing the correct positioning in the test facility.

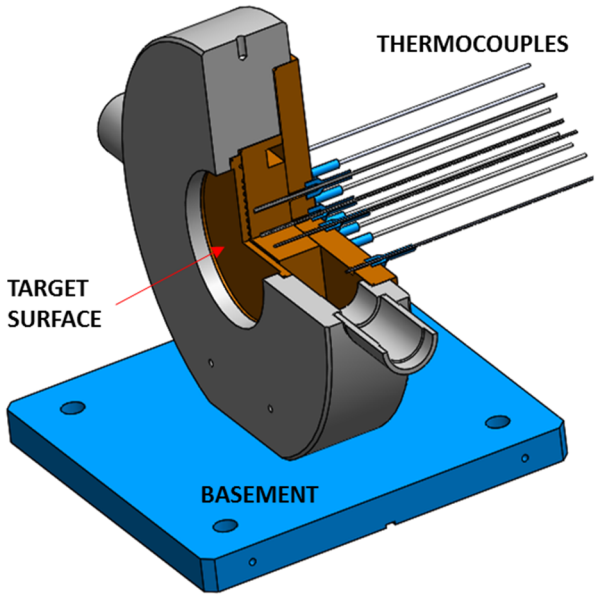

Figure C.4: Section of the CAD model of the mock-up installed in the test facility.

Appendix D

Preliminary design of the Mini-Channels geometry

The geometry of the mock-up equipped with MCs shown in the Figure 2.10 and Figure 2.11 is the results of a design process performed on its cooling structure. A preliminary model is used to determine the dimensions of the by-pass channel which allow to respect the pressure drop constraints imposed by the test facility, fixing the characteristics (diameter and length) of the MCs.

An analytical simplified pressure drop model implemented in Matlab® is used to evaluate the distribution of the coolant mass flow rate between the mini-channels and the by-pass channels and to compute the overall pressure drop between the inlet and the outlet section of the mock-up. Several simulations have been performed modifying the dimension of the by-pass channels to achieve the best configuration which allows to respect the pressure drop limit of the facility. The mass flow rate in the inlet section of the mock-up is divided in two parallel streams. A set of empirical pressure drop correlations (see details below) is used to model the coolant behaviour. The different components of the cooling circuit have been modelled by means of the related hydraulic impedances, sketched in Figure D.1.

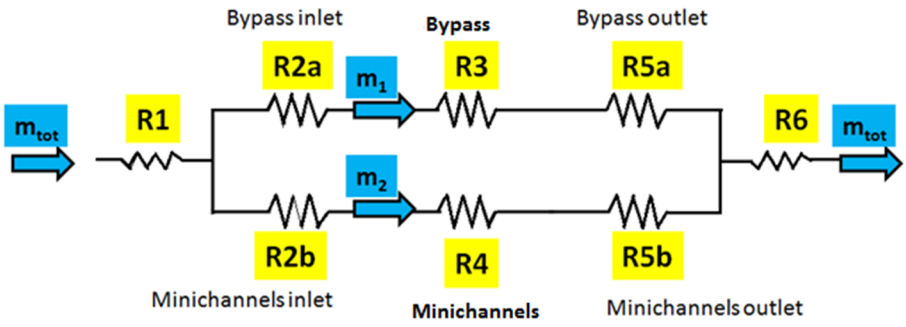

Figure D.1: Sketch of the analytical simplified model for the evaluation of the pressure loss in the cavity mock-up equipped with mini-channels. The mass flow rate repartition is highlighted in light blue while the various hydraulic impedance are highlighted in yellow.

Following the coolant direction in the mock-up cooling circuit, the hydraulic impendences are defined as:

- R1 represents the contribution of the localized pressure drop due to the enlargement of the cross section of the fluid from the mock-up inlet pipe to the mixing chamber, in the region located upstream of the central block;
- R2a (R5a) and R2b (R5b) give the contributions of the inlet (outlet) sections of the mini-channels and of the bypass channel, respectively. The hydraulic impedances are computed as localized pressure drop coefficients, characteristic of the sudden contraction (enlargement) of a pipe from (to) an infinite environment;
- R3 and R4 describe the distributed pressure losses along the mini-channels and the bypass channels, respectively;
- R6 represents the contribution of the localized pressure drop due to the reduction of the cross section of the fluid from the manifold that is located downstream of the central block of the mock-up to the outlet pipe.

The effects of the inlet and the outlet manifolds of the mock-up are not included in the analytical model due to the complexity of the geometry. In order to integrate their effects on the hydraulic description of the mock-up, a set of pure hydraulic CFD simulations without any obstacle along the fluid path are used. The hydraulic characteristic curve obtained in this way is included in the analytical pressure drop model of the mock-up equipped with MCs.

The evaluation of the localized pressure losses at the level of the MCs and of the bypass inlet and outlet sections (R2a, R2b and R5a, R5b in Figure D.1) are performed by (36) [47]:

$$\Delta p_{R2+R5} = 1.4 \times \frac{G^2}{2\,\rho} \tag{36}$$

in which G represents the specific mass flow rate inside the channel, and ρ is the fluid density.

The evaluation of the pressure drop along the MCs and by-pass channels length is computed by (37):

$$\Delta p_i = f_{R_i} \times \rho \, \frac{v^2}{2\,D_h} l \tag{37}$$

in which: v is the fluid speed, D_h and l are the hydraulic diameter and the length of the channels, respectively, finally f_{R_i} is the friction factor that characterize the geometries of the two channels, given by the semi-empirical correlations (38) and (39) for the rectangular and semi-circular shape, respectively.

$$f_{R3} = [0.79 \times \log(Re_C) - 1.64\,]^{-2} \tag{38}$$

$$f_{R4} = [-1.8 \times \log_{10}(6.9/Re)]^{-2} \times g(c) \tag{39}$$

in which Re_C is the Reynolds number modified based on the aspect ratio of the rectangular cross section of the channel [48], and Re is the Reynolds number evaluated using the hydraulic diameter. The function $g(c)$ depends on the channel geometry: in case of semi-circular ducts in complete turbulent flow regime $g(c) = 1$, while for laminar conditions $g(c) = {}^{c}/_{64}$, in which c is 63.017 [49].

Figure D.2a shows the hydraulic characteristic curves computed with the analytical simplified model of the hydraulic impedances in the mock-up equipped with MCs. The results are shown modifying the side dimensions of the by-pass, maintaining unchanged the characteristics of the semicircular channels. The region delimited by the black dashed lines between 36 l/min and 90 l/min indicates the limits on the mass flow rate of the FE200 test facility. The pressure threshold at 5 bar represents the maximum pressure drop allowed by facility during the test campaign.

The results obtained with the simplified model show that the mock-up characterized by two squared by-pass channels with side dimension of 5.5 mm allows to respect the constraint of a maximum pressure drop of 5 bar imposed for the test campaign applying on the inlet section the maximum mass flow rate of 90 l/min. The Figure D.2b shows the average Reynolds number evaluated on the MCs cross

section (blue dotted line) fixing to 5.5 mm the side dimension of the by-pass channel and the same quantity evaluated on the full size geometry of the cavity in nominal mass flow conditions (green dashed line). The comparison shows that the behavior of the gyrotron cavity at the nominal mass flow rate is represented by the mock-up with inlet mass flow rate of ~70 l/min. In addition, Figure D.2b reports the fraction of the mass flow rate flowing inside the MCs according to the analytical model.

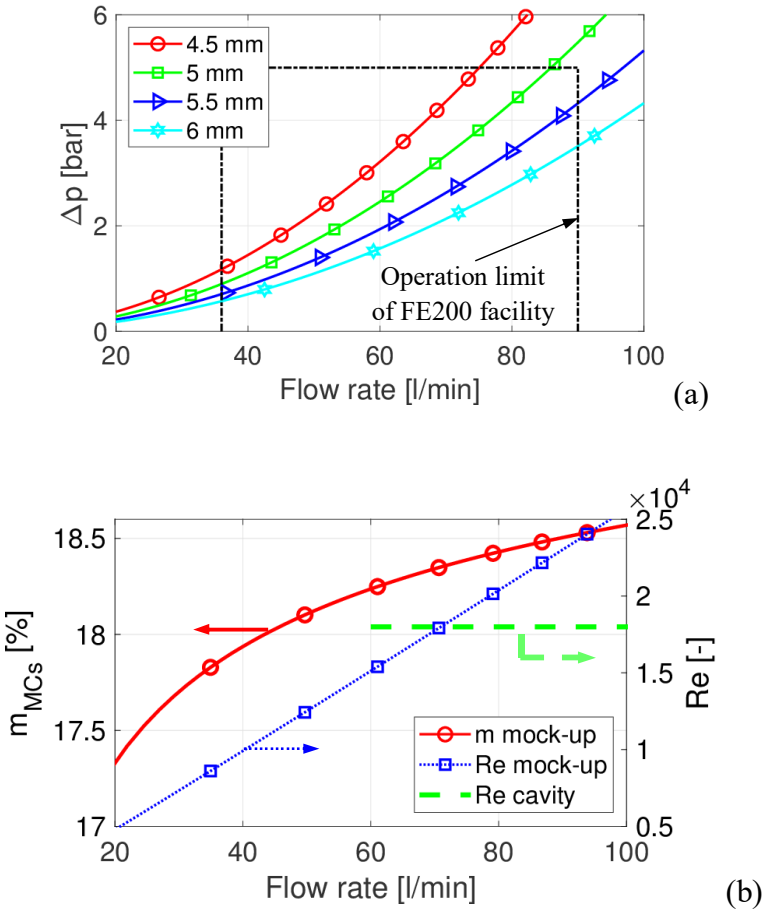

Figure D.2: (a) Hydraulic characterization of the mock-up equipped with MCs computed with the simplified model, for different dimension of the bypass channels (solid lines). The region inside the dashed black rectangle indicates the operational range of the FE200 test facility. (b) Left axis: computed fraction of the mass flow rate inside the MCs (solid line with circles). Right axis: comparison between mock-up (dotted line with squares) and full size cavity (thick dashed line) average Re number inside the MCs. The dimension of the by-pass channel is fixed to 5.5 mm of side.

The results of the analytical model are used for the definition of the mock-up geometry which is used in the CFD simulation. For the 2016 test campaign the same

CAD model is used to manufacture the mock-up, which is characterized by squared shaped bypass channels with side of 5.5 mm.

Appendix E

Simulation procedure for the definition of the Raschig Rings domain

The procedure applied in the definition of the RRs domain is implemented in the software STAR-CCM+® using the lagrangian Discrete Element Method (DEM) model [20].

In the first stage of the procedure, a cylinder with exactly the same geometrical characteristics of the single RR (i.e. the external radius and the length) is defined in the simulation in order to models its external volume as a solid particle easily managed by the software. In the same time, the volume occupied by the entire RRs region (or a part of it to reduce the computational domain in the DEM simulations) is created. The function of this block is obtaining an empty box which will be successively filled with the cylindrical dummy particles. The total number of RRs present in the unit volume of the porous region is defined according the test performed by Tecnalia [50], which results are and reported in the internal report [37][i].

The injecting simulation of the RRs is performed defining a random injection process of the particles to fill uniformly the box previously defined. The simulation is stopped when the suitable number of particles inside the volume is reached. Since the particles in the simulations are set as non-deformable, due to the lack of information about the mechanical behaviour of the single RR, the penetration of the RRs

[i] The information present in [37] are confidential.

particles is possible to obtain the desired level of void fraction of the porous medium generated. Finally, the position and the orientation of each dummy particle of the RRs region is extracted thanks to a user defined java® [51] macro and the information collected are then used to replace the dummy particles with the more detailed version of the RRs.

Thanks to the geometry reduction performed in the definition of the module of the RRs region, the complete space allocated for the pours medium inside the cavity and inside the mock-up is filled repeating the RRs module (see Figure E.1) previously obtained. This strategy reduced considerably the time need to fill the RRs region in the DEM simulation and in the procedure used to obtain the solid structure of the RRs region.

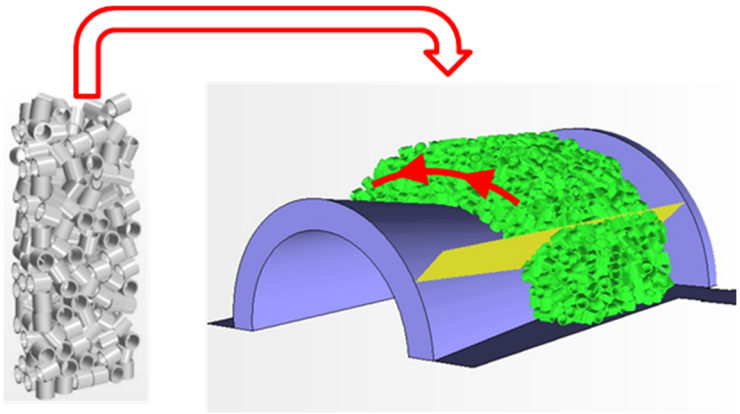

Figure E.1: Sketch of the filling process of the cavity equipped with RRs.

The RRs region is now fused with the resonating region of the cavity obtaining a single solid region. The thermal property which characterize the glidcop and the RRs regions (i.e. thermal conductivity) are defined by suitable field functions which assign the correct value depending on the position of each point of the domain.

Finally, the fluid region of the cavity and of the mock-up is defined subtracting from the original fluid domain (previously defined without the presence of the RRs region) the solid domain which includes the RRs region.

Appendix F

Evaluation of the pressure loss in the lower region of the coaxial insert

The effects of fluid path in the initial part of the insert has been evaluated by empirical pressure drop correlations and by a CFD simulation on the bent region of the coaxial insert cooling circuit (see Figure F.1) in order to set properly the inlet coolant condition (pressure) in the upper part of the insert.

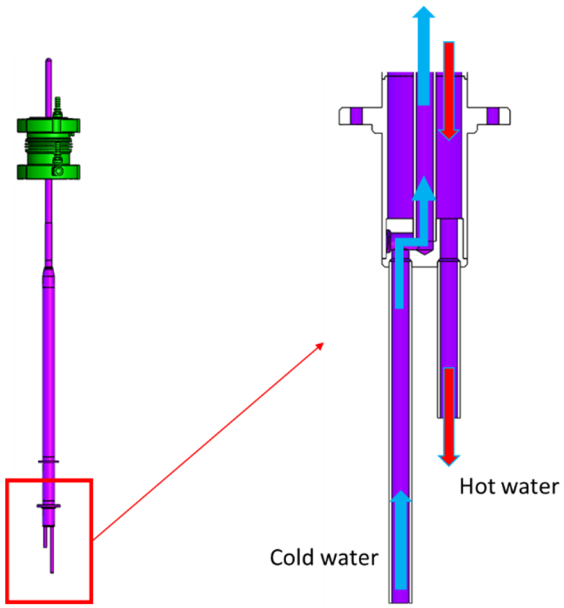

Figure F.1: Cut section of the inlet and outlet region of the coaxial insert.

The computed pressure drop experienced by the coolant from the inlet section of the insert to the cavity region is ~2.8 bar, subdivided in:

- ~2.1 bar in the bent region of the lower part of the insert, evaluated by a pure hydraulic CFD simulation;
- ~0.6 bar computed as distributed pressure loss in the straight pipe of the coaxial insert, by using the empirical Blasius pressure drop correlation [47];
- ~0.1 bar from the gravity head.

According this results, the pressure defined at the inlet section of the coaxial insert simulations of the MUCCA tool is set to 5.2 bar.

References

[1] F. Romanelli, Fusion Electricity, a roadmap to the realisation of fusion energy, EFDA, 2012.

[2] "The world bank," [Online]. Available: http://www.worldbank.org/. [Accessed 28 November 2018].

[3] T. Donné and W. Morris, European Research Roadmap to the Realisation of Fusion Energy, EUROfusion, 2018.

[4] J. P. Freidberg, Plasma physics and fusion energy, Cambridge University Press, 2007.

[5] B. B. Kadomtsev, T. F. S., W. M. L., R. P. H. and M. V. S. Yoshikawa M., "Tokamaks," *Nuclear Fusion,* vol. 30, no. 9, pp. 1675-1694, 1990.

[6] I. IO, "ITER Newsline - it's now official: First Plasma in December 2015," 20 June 2016. [Online]. Available: https://www.iter.org/newsline/-/2482. [Accessed 15 November 2018].

[7] "ITER," [Online]. Available: https://www.iter.org. [Accessed 26 November 2018].

[8] "EUROfusion," [Online]. Available: https://www.euro-fusion.org. [Accessed 28 November 2018].

[9] "The Nuclear Fusion Programme at a Glance," [Online]. Available: https://www.fusion.kit.edu. [Accessed 28 November 2018].

[10] "Fusion power," [Online]. Available: https://en.wikipedia.org/wiki/Fusion_power. [Accessed 26 November 2018].

[11] M. V. Kartikeyan, E. Borie and M. K. A. Thumm, Gyrotrons: high power microwave and millimeter wave technology, Springer, 2004.

[12] C. Darbos, F. Albajar and T. Bonicelli, "Status of the ITER Electron Cyclotron Heating and Current Drive System," *Journal of Infrared, Millimeter, and Terahertz Waves,* vol. 37, no. 1, pp. 4-20, 2016.

[13] M. Thumm, "State-of-the-Art of High Power Gyro-Devices and Free Electron Masers," KIT Scientific Publishing, Karlsruhe, 2015.

[14] J. Jelonnek, *High Power Microwave Technology. Section 3.5, Gyrotron.*

[15] E. Borie, "Review of gyrotron theory," Institut für Technische Physik, Karlsruhe, 1991.

[16] P. A. Lindsay, R. M. Jones and R. J. Lumsden, "Some observations on gyrotron interaction models," *International Journal of Electronics,* vol. 57, no. 6, pp. 915-951, 1984.

[17] C. J. Edgcombe, Gyrotron Oscillators: Their Principles and Practice, London: Taylor & Francis Ltd., 1993.

[18] "Glidcop data sheet," [Online]. Available: https://www.hoganas.com/en/powder-technologies/glidcop/. [Accessed 28 November 2018].

[19] L. Savoldi, A. Bertinetti, F. G. Nallo, A. Zappatore, R. Zanino, F. Cau, F. Cismondi and Y. Rozier, "CFD Analysis of Different Cooling Options for a Gyrotron Cavity," *IEEE Transactions on Plasma Science,* vol. 44, no. 12, pp. 3432-3438, 2016.

[20] Software Siemens PLM, STAR-CCM+® Documentation, version 13.02, 2018.

[21] K. A. Avramides, C. Pagonakis, C. T. Iatrou and J. L. Vomvoridis, "EURIDICE: A code-package for gyrotron interaction simulations and cavity design," *EPJ Web Conf,* vol. 32, 2012.

[22] K. Avramidis, A. Bertinetti, F. Albajar, F. Cau, F. Cismondi, G. Gantenbein, S. Illy, Z. Ioannidis, J. Jelonnek, F. Legrand, I. Pagonakis, Y. Rozier, T. Rzesnicki, L. Savoldi, M. Thumm and R. Zanino, "Numerical Studies on the Influence of Cavity Thermal Expansion on the Performance of a High-Power Gyrotron," *IEEE Transactions on Electron Devices,* vol. 65, no. 6, pp. 2308-2315, 2018.

[23] R. F. Menter, "Two-equation eddy-viscosity turbulence models for engineering applications," *AIAA,* vol. 32, no. 8, pp. 1598-1605, 1994.

[24] W. M. Rohsenow, "A method of correlating heat transfer data for surface boiling of liquids," 1951.

[25] J. G. Collier, Convective Boling and Condensation, 3rd ed., Oxford Science Publications, Clarendon Press, 1994.

[26] F. P. Incropera, D. P. Dewitt, T. L. Bergmann and A. S. Lavine, Introduction to heat transfer, 6th ed., John Wiley & Sons, 2011.

[27] D. L. Youchison, M. A. Ulrickson and J. H. Bullock, "Prediction of Critical Heat Flux in Water-Cooled Plasma Facing Components Using Computational Fluid Dynamics," *Fusion Science and Technology,* vol. 60, no. 1, pp. 177-184, 2011.

[28] "The International Association for the Properties of Water and Steam," [Online]. Available: http://www.iapws.org. [Accessed 5 April 2017].

[29] P. J. Karditsas and B. M., "Thermal and Structural Properties," [Online]. Available: http://www-ferp.ucsd.edu/LIB/PROPS/PANOS/cu.html. [Accessed 8 August 2018].

[30] J. W. Davis and P. D. Smith, ITER material properties handbook, J. Nucl. Mater., 1996.

[31] A. Leggieri, "F4E-OPE-447: Report on thermal cavity mock-up experiments," 2017.

[32] L. Savoldi, "F4E-2015-EXP-223: Experimental and Simulation Results on Mock-Ups equipped with Raschig Rings and Mini-Channels," 2017.

[33] A. Bertinetti, F. Albajar, F. Cau, A. Leggieri, F. Legrand, E. Perial, G. Ritz, S. L, R. Zanino and A. Zappatore, "Design, Test and Analysis of a Gyrotron Cavity Mock-Up Cooled Using Mini Channels," *IEEE Transactions on Plasma Science,* vol. 46, no. 6, pp. 2207-2215, 2018.

[34] T. -. H. Shih, W. W. Liou, A. Shabbir, Z. Yang and J. Zhu, "A new k-ϵ eddy viscosity model for high reynolds number turbulent flows," *Computers & Fluids,* vol. 24, no. 3, pp. 227-238, 1995.

[35] A. Bertinetti, K. A. Avramidis, F. Albajar, F. Cau, F. Cismondi, Y. Rozier, L. Savoldi and R. Zanino, "Multi-physics analysis of a 1 MW gyrotron cavity cooled by mini-channels," *Fus. Eng. Des,* vol. 123, pp. 313-316, 2017.

[36] K. A. Avramidis, private communications, 2016-2019.

[37] Tecnalia, "F4E-OFC-167: ITER relevant raw materials. Raching Rings Characterization.," 2016.

[38] L. Savoldi, F. Albajar, S. Alberti, K. A. Avramidis, A. Bertinetti, F. Cau, F. Cismondi, G. Gantenbein, H. J.-P., Z. C. Ioannidis, P. Kalaria, A. Leggieri, F. Legrand, I. G. Pagonakis, S. Ruess, T. Rzesnicki and R. Zanino, "Assessment and Optimization of the Cavity Thermal Performance for the European Continuous Wave Gyrotrons," *27th IAEA Fusion Energy Conference, Ahmedabad, India,* 2018.

[39] J.-P. Hogge, *Private communication,* 2018.

[40] T. Rzesnicki and e. al, "Experimental verification of the European 1MW, 170GHz industrial CW prototype gyrotron for ITER," *Fusion Engineering and Design,* vol. 123, pp. 490 - 494, 2017.

[41] K. A. Avramidis, A. Bertinetti, Z. C. Ioannidis, G. Gantenbein, S. Illy, P. C. Kalaria, I. G. Pagonakis, T. Rzesnicki, L. Savoldi, M. Thumm, R. Zanino and J. Jelonnek, "Validation of Multi-Physics Gyrotron Modeling against Experimental Results," *US-EU-Japan RF Heating Technology Workshop, Shizuoka, Japan,* 2018.

[42] S. M. Ross, Introduction to Probability and Statistics for Engineers and Scientist, Elsevier Academic Press, 2004.

[43] S. Ruess, K. A. Avramidis, M. Fuchs, G. Gantenbein, Z. Ioannidis, S. Illy, J. Jin, P. C. Kalaria, T. Kobarg, I. Pagonakis, T. Ruess, T. Rzesnicki, M. Schmid, M. Thumm, J. Weggen, A. Zein and J. Jelonnek, "KIT coaxial gyrotron development: from ITER toward DEMO," in *Proceedings of the 47th European Microwave Conference*, Nürnberg, 2017.

[44] L. Savoldi, "PMI-3-T005 - D002: Evaluation of the behaviour of a 2MW coaxial gyrotron cavity with the MUCCA tool," 2018.

[45] A. Bertinetti, F. Albajar, K. A. Avramidis, F. Cau, F. Cismondi, G. Gantenbein, J. Jelonnek, P. Kalaria, R. S., T. Rzesnicki, L. Savoldi and R. Zanino, "Analysis of an actively-cooled coaxial cavity in a 170 GHz 2 MW gyrotron using the multi-physics computational tool MUCCA," *Fusion Engineering and Design,* in press.

[46] S. Ruess, *Private communication,* 2017.

[47] F. M. White, Fluid mechanics, 7th ed., New York, USA: McGraw-Hill, 2009.

[48] O. C. Jones, "An improvement in the calculation of turbulent friction in rectangular ducts," *J. Fluid. Eng.,* vol. 98, no. 2, pp. 173-181, 1976.

[49] S. Kakac and W. Aung, Handbook of Single-Phase Convective Heat Transfer, USA: John Wiley & Sons, 1987, USA: John Wiley & Sons, 1987.

[50] "https://www.tecnalia.com," [Online]. [Accessed 5 December 2018].

[51] "Software java," [Online]. Available: https://www.oracle.com/it/java/. [Accessed February 2019].

[52] L. Savoldi, "F4E-2015-EXP-223: Multiphysics Analysis of the Working Point for a Gyrotron Cavity Equipped with Raschig Rings or Mini-Channels," 2015.

[53] J. R. Lamarsh, Introduction to nuclear reactor theory, New York: American Nuclear Society, 2002.